République Algerienne Démocratique et Populaire

Ministère de l'enseignement supérieur et de la Recherche scientifique

Université Djillali Liabès de Sidi Bel Abbès

Faculté de Technologie

Département de Génie Mécanique

Thèse

Présentée pour l'Obtention du Diplôme de Doctorat 3ème Cycle par:

DAHMANI ABDERRAOUF

Filiere: Génie Mécanique
Spécialité: Energéique et environnement

Intitulé de la thèse

INTENSÉFICATION DES TRANSFERTS THERMIQUES PAR ÉLECTROMAGNETISM

Soutenue le 21/06/2022

Jury :

BOUCHAM BELHADJ	Professeur	Président	UDL-SBA
LAOUEDJ SAMIR	Professeur	Directeur de thèse	UDL-SBA
SOLANO JUAN PEDRO	Professeur	Co-directeur de thèse	UPCT-Espagne
AISSA ABDERRAHMANE	MCA	Examinateur	UMS-Mascara
BOUZIANE ALI	MCA	Examinateur	UDL-SBA

Année Universitaire : 2021/2022

People's Democratic Republic of Algeria
Ministry of Higher Education and Scientific Research
Djillali Liabes University of Sidi Bel Abbès
Faculty of Technology
Mechanical Engineering Department

Thesis

Presented to Obtain the 3rd Cycle Doctorate Diploma by:

DAHMANI ABDERRAOUF

Field: Mechanical Engineering
Speciality: Energetic and environment

Title of the thesis

INTENSIFICATION OF HEAT TRANSFER BY ELECTROMAGNETISM

Defended on 21/06/2022

Jury :

BOUCHAM BELHADJ	Professor	President	UDL-SBA
LAOUEDJ SAMIR	Professor	Thesis director	UDL-SBA
SOLANO JUAN PEDRO	Professor	Thesis co-director	UPCT-Spain
AISSA ABDERRAHMANE	MCA	Examiner	UMS-Mascara
BOUZIANE ALI	MCA	Examiner	UDL-SBA

Academic Year : 2021/2022

Cuando todo está demasiado oscuro
puedes ver las estrellas.
— Ralph Waldo Emerson

To my parents, my family, my friends and to every single person that has
supported me on this journey . . .

Acknowledgements

Praise is to Allah by whose grace good deeds are completed

Abstract

The energy future is based on two main aspects; the renewable energies and the efficiency of energy systems. In this regard, this numerical work is aimed to study a compound method convective heat transfer intensification using a magnetic fluid (Ferrofluids) and a non-uniform magnetic field generated by current-carrying wire. The lion share of this work is dedicated for the study of the possibility of using this technique in the parabolic trough solar collectors absorber. The study included both flow regimes, laminar and turbulent. The effect of the magnetic field on the flow pattern, velocity distribution, streamlines, Nusselt number, as well as the friction factor are analyzed. On the other hand, this work has analyzed the effect of the magnetic field strength represented by the magnetic number, as well as the effect of the Reynolds number increment.

The results showed that the presence of a periodically distributed non-uniform magnetic field disturbs the velocity distribution and the ferrofluid motion, which leads to an improvement in the convective heat exchange, but this is accompanied by an increase in the friction factor. As another result, the increase in the strength of the magnetic field increases the value of the Nusselt number and the friction factor, but when the the Reynolds number increases it is noticed that the effect of the magnetic decreases in front of the inertial forces of the fluid.

Key words: Magnetic fluid, Ferrohydrodynamics, Laminar, Turbulent, Magnetic field, Current-carrying wire, Parabolic trough solar collector, Computational Fluid Dynamics.

الملخص

يتمركز المستقبل الطاقوي على نقطتين أساسيتين؛ الطاقات المتجددة و الكفاءة الطاقوية للأنظمة الطاقوية. في هذا الصدد، يهدف هذا العمل الرقمي الى دراسة أسلوب مركب لتكثيف التبادلات الحرارية باستعمال محلول مغناطيسي وحقل مغناطيسي غير منتظم متولد عن طريق أسلاك حاملة للتيار الكهربائي. تم تخصيص نصيب الأسد من هذا العمل لدراسة إمكانية استخدام هذه التقنية في أنبوب المركزات الشمسية من نوع طبق القطع المكافيء. الدراسة شملت كلا نظامي التدفق، الرقائقي و المضطرب، أين تمت معاينة تأثير الحقل المغناطيسي على شكل التدفق ،توزع السرعة، خطوط التيار عدد نوسلت وكذا معامل الاحتكاك. من جهة أخرى تطرقت الأطروحة إلى تحليل مدى تأثير قوة الحقل المغناطيسي الممثل في العدد المغناطيسي وكذا تأثير زيادة عدد رينولدس.

أظهرت النتائج أن تواجد حقل مغناطيسي غير منتظم موزع بشكل متناوب يولد اضطرابات على مستوى توزع السرعة و حركة المائع المغناطيسي مما يؤدي لتحسين التبادل الحراري، لكن يترافق هذا مع زيادة في معامل الإحتكاك. كنتيجة أخرى، الزيادة في قوة الحقل المغناطيسي تزيد من قيمة عدد نوسلت و معامل الاحتكاك ، غير انه عند الزيادة في عدد رينولدز يلاحظ تلاشي تأثير الحق المغناطيسي أمام قوة المائع العطالية

الكلمات المفتاحية : مائع مغناطيسي، فيروهيدروديناميكا، رقائقي، مضطرب، حقل مغناطيسي، سلك ناقل للتيار، مركز شمسي من نوع طبق القطع المكافيء، ديناميكا الموائع الحسابية .

Résumé

L'avenir énergétique repose sur deux aspects principaux ; les énergies renouvelables et l'effi-cacité des systèmes énergétiques. À cet égard, ce travail numérique a pour but d'étudier une méthode composée d'intensification convective du transfert de chaleur à l'aide d'un fluide magnétique (Ferrofluides) et d'un champ magnétique non uniforme généré par un fil conduc-teur de courant. La part du lion de ce travail est consacrée à l'étude de la possibilité d'utiliser cette technique dans l'absorbeur des collecteurs solaires cylindro-paraboliques. L'étude a inclus les deux régimes d'écoulement, laminaire et turbulent. L'effet du champ magnétique sur le modèle d'écoulement, la distribution de vitesse, les lignes de courant, le nombre de Nusselt, ainsi que le facteur de frottement sont analysés. D'autre part, ce travail a analysé l'effet de l'intensité du champ magnétique représenté par le nombre magnétique, ainsi que l'effet de l'incrément du nombre de Reynolds.

Les résultats ont montré que la présence d'un champ magnétique non uniforme distribué périodiquement perturbe la distribution de vitesse et le mouvement du ferrofluide, ce qui conduit à une amélioration de l'échange thermique convectif, mais cela s'accompagne d'une augmentation du facteur de frottement. Comme autre résultat, l'augmentation de l'intensité du champ magnétique augmente la valeur du nombre de Nusselt et du facteur de frottement, mais lorsque le nombre de Reynolds augmente, on remarque que l'effet du champ magnétique diminue devant les forces inertielles du fluide.

Mots clefs :Fluide magnétique, Ferrohydrodynamique, Laminaire, Turbulent, Champ magné-tique, Fil conducteur de courant, Collecteur solaire cylindro-parabolique, Dynamique des fluides computationnelles.

Contents

List of Figures

List of Tables

List of symbols

c_p	specific heat (J/(kg·K))
C_R	collector concentration ratio
D	absorber tube inner diameter (m)
D_e	absorber tube outer diameter (m)
d_p	particle diameter (m)
T	temperature (K)
H	magnetic field intensity vector modulus (A/m)
H_x	magnetic field intensity component in x direction (A/m)
H_y	magnetic field intensity component in y direction (A/m)
H_r	characteristic magnetic field intensity (A/m)
h	heat transfer coefficient (W/(m^2·K))
I	electric current (A)
I_g	global radiation (W/m^2)
I_b	beam radiation (W/m^2)
k	thermal conductivity (W/(m·K))
K_B	Boltzmann constant ($=1.3806503 \times 10^{-23} J/K$)
L	tube length (m)
l	wire pitch length (m)
M	magnetization (A/m)
m_p	particle magnetic moment(A.m^2)
P	pressure (Pa)
q''	heat flux (W/m^2)
V_{avg}	mean axial velocity (m/s)
x,y,z	directions

Dimensionless groups

f	Darcy friction factor, $f = \frac{2\Delta P}{\rho_f V^2}(\frac{D}{L})$
Nu	Nusselt number, $Nu = \frac{hD}{k}$
Mn	Magnetic number, $Mn = \frac{\mu_0 \chi H_r^2 h^2}{\rho_f v_f^2}$
Pr	Prandtl number, $Pr = \frac{\mu c_p}{k}$
Re	Reynolds number, $Re = \frac{\rho V D}{\mu}$

Greek symbols

α_f	thermal diffusivity (m^2/s)
φ	particle volume fraction
ξ	Langevin parameter
μ	dynamic viscosity ($kg/(m \cdot s)$)
μ_0	vacuum permeability (=$4\pi \times 10^{-7}\ T \cdot m/A$)
μ_B	Bohr's magneton (=$9.27 \times 10^{-24} A \cdot m^2$)
ν	kinematic viscosity (m^2/s)
ρ	density (kg/m^3)
χ	magnetic susceptibility

Subscripts

b	base fluid
f	ferrofluid
in	inlet
p	nanoparticle
w	wall

Abbreviations

PTSC	parabolic trough solar collector
MF	magnetic field
HTF	heat transfer fluid

Introduction

Undoubtedly, the convective heat transfer has noteworthy importance in many energetic processes, industrial applications and sectors, such as the chemical processes, power generation or tr systems...etc. Due to this importance, the quest for optimum convective heat transfer systems was and still the main challenge for many researchers and engineers, driven by their energetic, environmental and economic concerns.

The enhancement techniques could be arranged into two major methods passive and active techniques, in other words, if the technique needs energy from an external source, here, it is considered as active technique, in contrast, it is a passive technique if no external energy is needed. However, a combination between both techniques is defined as a compound method.

The researches in the aerospace field, have always been a reason for new innovations and products that serves the life in our planet in itself. Among this innovations, a magnetic fluid was developed in NASA's laboratories by Steve Papell in the 60's of the previous century, within the frame of developing a new magnetically controllable rocket fuel in the weightless conditions. This magnetic fluids which are commonly called ferrofluids, are composed of nano-sized particles with magnetic properties and a base fluid. Nowadays, the applications capabilities of ferrofluids in presence of a magnetic field, attract the attention of many researchers in heat transfer field, as a heat transfer enhancement technique. In this regard, the present work comes as an attempt to benefit from the effect of the magnetic field on ferrofluids flow in convective heat transfers intensification.

Accordingly, the present thesis focuses on the numerical study of the magnetic field effect on the ferrofluids using a new current-carrying wire configuration to generate the magnetic field. The proposed configuration is based on a periodic change of the wire position, introducing a periodic flow disturbance due to the variation of the magnetic field intensity along the tube. Taking into account present-day challenges in the renewable energies technologies optimization, the lion share of this work analyzes the integration of this technique in the parabolic trough solar collectors (PTSCs), exactly in the PTSC absorber tube.

This work is organized in four chapters, resumed in the following points:

1. The first chapter gives generalities about the heat transfer enhancement techniques with illustrations, as well as the ferrohydrodynamics theories, notions and some of examples of its application domains, since the study of the interactions between the magnetic field and the ferrofluids fall under this discipline. Besides that, this chapter

includes a comprehensive literature review for the relevant works as a background for our research.

2. The second chapter is dedicated for the mathematical formulation that describes mathematically what occurs during the interaction of the magnetic field and the ferrofluids flows which paves the way for the construction of the numerical model. The chapter also explains the simulation methodology.

3. The third and the fourth chapter show and discuss the obtained results for both flow regimes, the laminar and the turbulent regime. The results are presented and visualized in form of contours, streamlines and graphs in term of dimensionless numbers.

Finally, this doctoral dissertation finishes with a conclusion points out the main outcomes from this research, the recommendations and the the future works.

1 Generalities and literature review

1.1 Introduction

The content of this chapter is divided into three major sections, the first section discusses the heat transfer enhancement techniques and their classification, passive, active and compound methods. Since the present work belongs to ferrohydrodynamics as a discipline, the second section touched upon its inception and the important notions about the ferrofluids, their structure and properties, as well as the magnetism and magnetization of materials, the section shows also some of the promising application using ferrofluids. The final section act as a literature review of the applications of ferrofluids and electromagnet forces as a heat transfer enhancement solution.

1.2 Heat transfer enhancement techniques

The intensification of the convective heat transfer in the heat exchange systems is important key to increase the efficiency, to downsize the heat exchange equipment, to reduce the power consumption and the costs, depending on the objectives of the targeted system.

A closer look at Newton's law (Eq 1.1) shows that the enhancement of the convective heat transfer would be performed by increasing the value of the heat transfer coefficient h or the area A_s [1].

$$\dot{Q} = h A_s (T_s - T_\infty) \tag{1.1}$$

Mainly, the enhancement methods can be classified according to the traditional distinction between passive techniques do not employ any external power and active methods employ an external source of energy, Figure 1.1 resumes some examples for both methods. However, a detailed examples from the open literature for the methods are represented in the next two subsections.
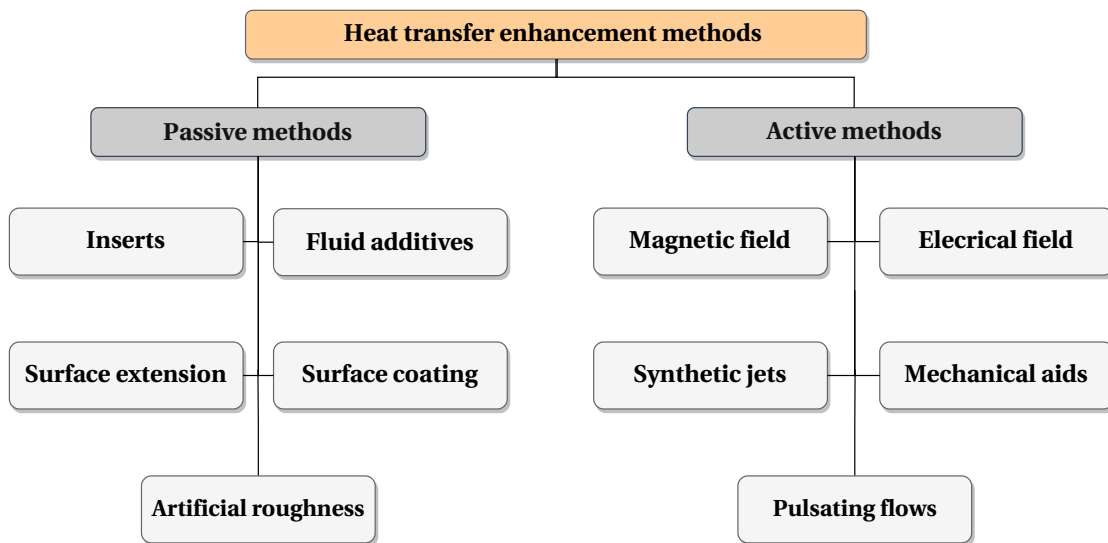
Figure 1.1: Heat transfer enhancement methods classification of some techniques.

1.2.1 Passive methods

1.2.1.1 Geometrical modifications

The geometrical manipulations of the surfaces in the heat exchange equipment are widely used as enhancement methods [2] and the most common in the commercial equipment. According to Webb et al. [3], an enhanced heat transfer surface is capable to increase the hA value (Eq. 1.1), i.e. extending the surface increases the area A_s, moreover, shaping the surface with a special structures increases the heat transfer coefficient h, which leads consequently to improve the convective heat transfer. However, many techniques belong to this category, including but not limited to:

a) *Fins:* The fins are defined as extended surfaces forming protrusions, characterized by their shape or profile, Figure 1.2 represents the common types of the fins, Figure 1.3 shows a real example of annular finned tube.
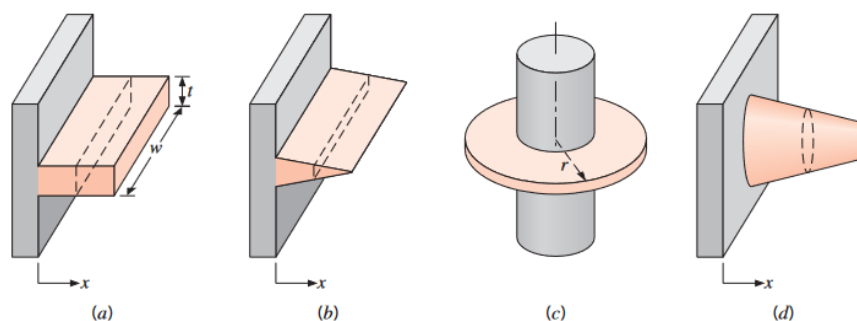
Figure 1.2: Fin types. (a) Straight fin of uniform cross section. (b) Straight fin of nonuniform cross section. (c) Annular fin. (d) Pin fin [4].

Figure 1.3: Latent thermal energy storage accumulator equipped by annular-finned tubes (ACCUSOL project).

b) *Inserts:* This elements are inserted into the heat exchange equipment to enhance the flow mixing and the heat transfer, they are existing in various forms as displaced inserts (e.g. Coils Figure 1.4b) or swirl flow devices (e.g. twisted tape Figure 1.4a).

(a)　　　　　　(b)
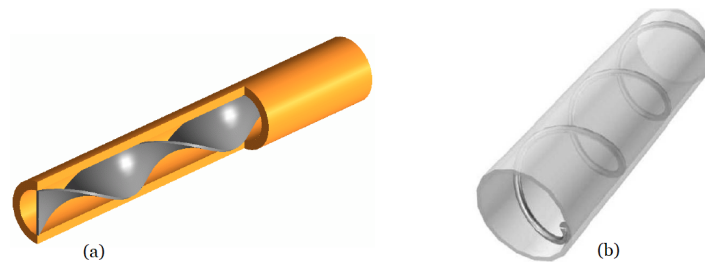
Figure 1.4: (a) Twisted tape, (b) Wire-coil insert [5].

c) *Metallic foam:* The metallic foam is an innovative class of cellular low-weight and high thermal conductive material with a porous structure made of metals such as the aluminium (Figure 1.5a) [6], the metallic foam knows many applications as enhancement technique due to its structure and properties which improve the mixing and the heat transfer performance [7], Figure 1.5b shows a latent thermal storage system (LTES) equipped with aluminium foam for enhancement purposes.

(a)　　　　　　(b)

Figure 1.5: (a) Open cell aluminium foam blocks, (b) thermal storage system equipped with aluminium foam (ACCUSOL project).

d) *corrugated tubes:* The modification of the main shape of the tube is commonly used as a technique to enhance the convective heat transfer, giving the tubes certain shape like corrugation (see Figure 1.6) affects the flow pattern which leads to create a secondary flows that improve the convection [8].

Figure 1.6: Helical corrugated tube (SACOME company).

e) *Coiled tubes:* The coiled tubes passively enhance the convection by producing secondary flows, in addition the coiled form reduces heat exchangers size [3].
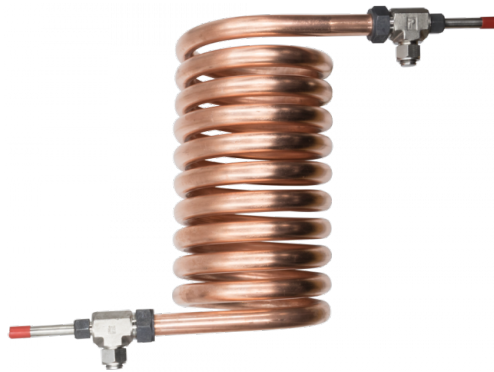
Figure 1.7: Helically coiled tube.

1.2.1.2 Surface coating

This technique applies metallic and nonmetallic materials to coat the heat exchange surfaces to enhance the convection. Figure 1.8 shows a real example from the literature.
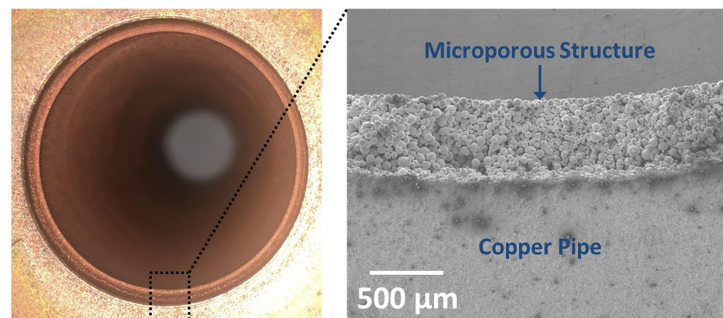
Figure 1.8: Microporous coating [9].

1.2.1.3 Fluid additives

This enhancement technique exploit solid particles, gas bubbles or liquid droplets, depending on the nature of the fluid (liquid or gas) [5], Figure 1.9 shows Al_2O_3 nanoparticles and Al_2O_3/DI-water nanofluid with different volume fractions.

| (a) | (b) |
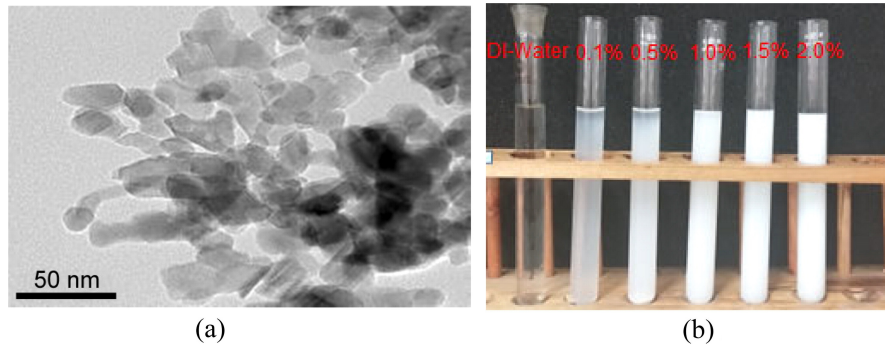
Figure 1.9: (a) Al_2O_3 nanoparticles, (b) nanofluid with different concentrations [10].

1.2.2 Active methods

1.2.2.1 Mechanical aids

To improve the convective heat transfer, the mechanical aids help to perturb the thermal boundary layers near to the heat exchange surfaces by mechanical mechanisms like stirring or the rotation of the walls, Figure 1.10 showes a parabolic trough solar collector equipped by rotating absorber (the rotation mechanism is framed with yellow).

Figure 1.10: Rotary coaxial double-twisted tape employed inside a tube [11].

1.2.2.2 Synthetic jet

The synthetic jet is a fluidic device that jets a generated air through an orifice of a synthetic jet actuator, the actuator consists of a cavity and moving wall called a diaphragm or a membrane (see Figure 1.11) that ensures the oscillating movement [12] the created vortices by the device improve the heat transfer.
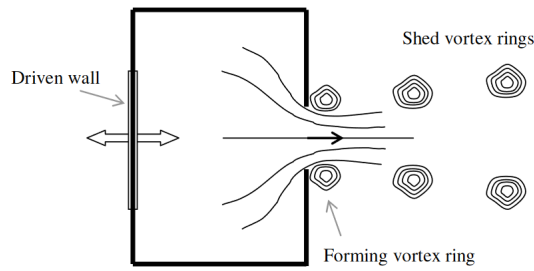
Figure 1.11: Schematic of synthetic jet actuator [12].

1.2.2.3   Pulsating flow

This method gives the heat transfer fluid a mechanical pulsation or oscillatory motion to perturb the thermal boundary layer which leads to improve the heat transfer enhancement [13]. Figure 1.12 shows Particle Image Velocimetry (PIV) vizualization of pulsating flow in Oscillatory Baffled Reactor (OBR) for different piston positions
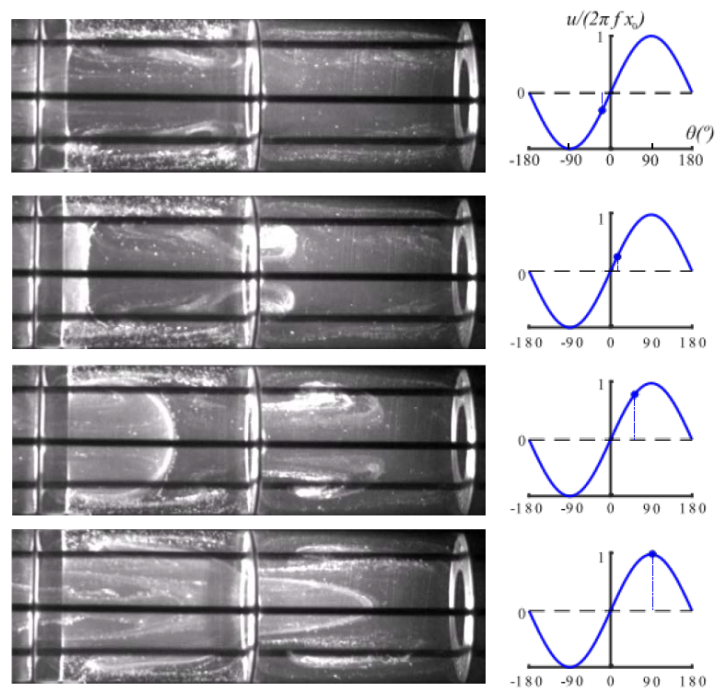
Figure 1.12: PIV visualization of oscillating flow [14].

1.2.2.4   Electrical field

The use of electrical fields knows increasing attraction in the recent decades as enhancement technique due to the effect of this field on the heat transfer fluid flow pattern and behaviour. This technique is mainly based on the fact that the presence of an electrical field generated with high voltage and low electrical current, disturbs the fluid boundary layer. As an example, Figure 1.13 shows how the electrical field with different voltages voltage affects on air streamlines.
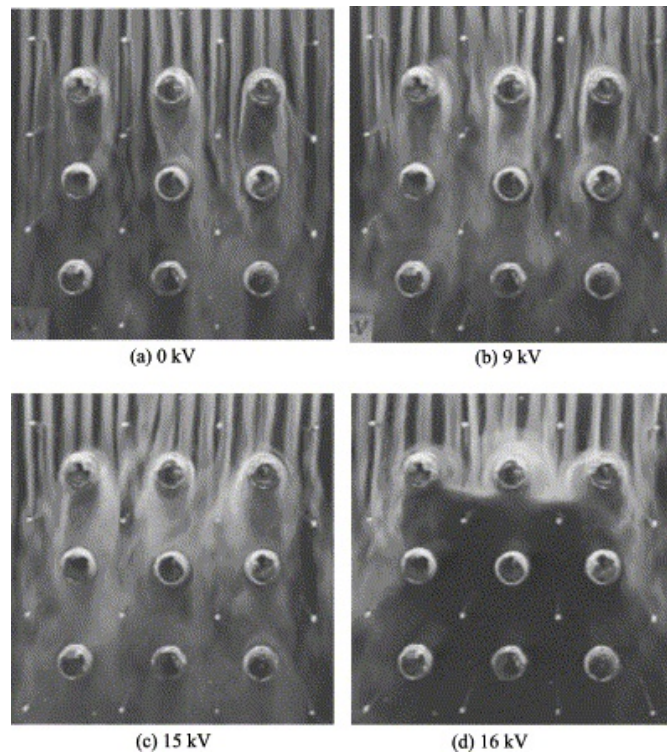
Figure 1.13: Electric field influence on air stream for various voltage values [15].

1.2.2.5 Magnetic field

Similarly to the previous technique, the use of the magnetic field to enhance the convective heat transfer became interesting only in the recent decades. The application of a magnetic field on fluids with magnetic properties generates a body force (kelvin body force) which affects on the thermal-hydraulic characteristics. Since this technique is the subject of the present work, more details will be in the next sections.

1.2.3 Compounding methods

The employment of the enhancement techniques is not limited in one technique, for that reason the researchers and the designers in the industrial sectors could use various methods simultaneously to rich an optimum improvement, combining multiple passive or active methods or by using both, active and passive methods [3]. As an example Figure 1.14 shows a rotary coaxial double-twisted tape (passive method) inside a heat exchanger tube where the rotation of the mechanism is achieved by the means of electrical motor (active method).
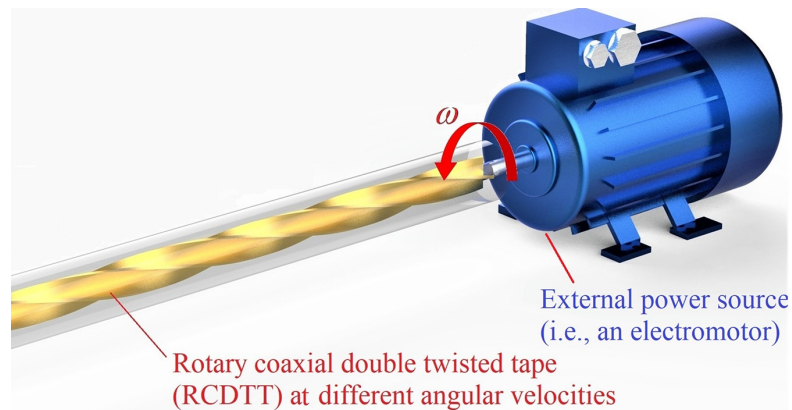
Figure 1.14: Rotary coaxial double-twisted tape employed inside a tube [16].

1.3 Ferrohydrodynamics

The ferrohydrodynamics which is called FHD for short, represents the discipline that studies the mechanical behaviour of the fluids with magnetic properties under the effect of the magnetic forces. Following to R. Rosensweig [17], the research in the FHD began in the 60s of the previous century, about 30 years after the first ferrofluid manufactured by F. Biiter. In this area, the most common used fluids are the ferrofluids and the magnetorheological fluids, where they differ in the size of the dispersed particles, nanoparticles or microparticles, respectively [18].

1.3.1 Ferrofluids

A ferrofluid is defined as a synthetic and stable colloidal made of nano-sized magnetic particles (see Figure 1.15) and an organic or polar base fluid (carrier liquid), such as oil or water, respectively. The used nanoparticles for the elaboration of ferrofluids are made of elements with high magnetic properties like iron, nickel, cobalt, their alloys or their oxides such as the nickel oxide (NiO), the magnetite (Fe_3O_4)...etc [17]. The small size of this nanoparticles prevent from the sedimentation in presence of gravitational forces or average magnetic field. In addition, the nanoparticles is coated by surfactant made of chain-like organic molecules (e.g., oleic acid) to avoid the agglomeration of the nanoparticles and to ensure the ferrofluid stability benefiting from the generated repulsive forces, a schematic view of coated magnetic nanoparticles in a colloidal ferrofluid is shown in Figure 1.16). [19].
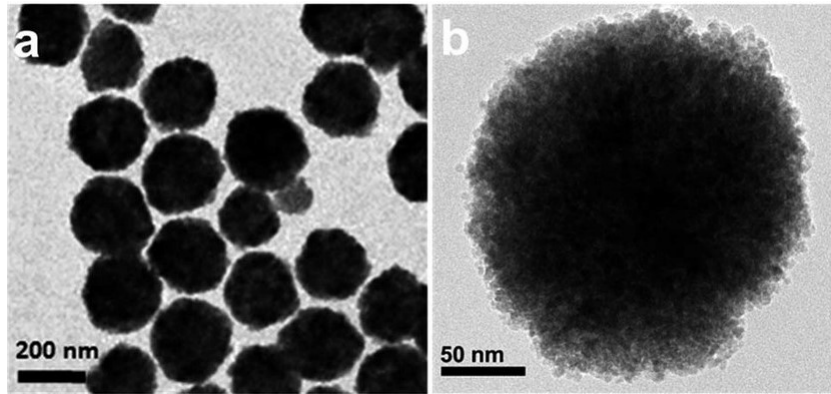
Figure 1.15: Transmission Electron Microscopy (TEM) images of magnetite particles (Fe$_3$O$_4$) [20].
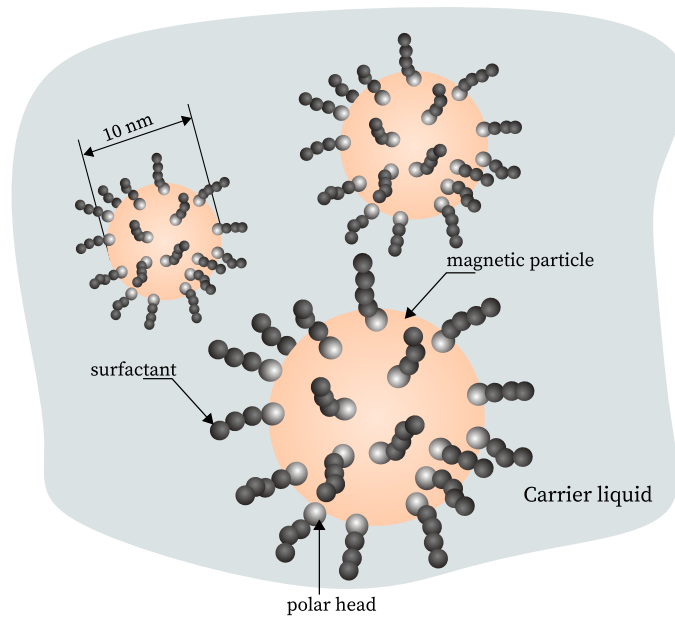
Figure 1.16: Schematic view of ferrofluid structure.

1.3.2 Magnetic field effect on ferrofluids

Similar to the iron filings, when a ferrofluid is exposed to a magnetic field , the ferrofluid clings to the source of this field forming spike-shape as it is illustrated in Figure 1.17 [17]. Contrary to the magnetohydrodynamics (MHD), the resulting force that arises during the interaction of a ferrofluid and an external magnetic field ($\overrightarrow{H}$) is called Kelvin force density which is mathematically represented by equation (1.2) [21], more details about the mathematical formulation that describes the FHD problems are presented in the second chapter. On top of that, the Kelvin body force gives the ability to control the ferrofluid's motion and allows the manipulation of its behavior.

$$\overrightarrow{F_k} = \mu_0 (\overrightarrow{M} \cdot \nabla) \overrightarrow{H} \tag{1.2}$$

In equation (1.2), μ_0 denotes the vacuum permeability and the vector $\overrightarrow{H}$ stands for the magnetic field which is by definition; the acting force on magnetic pole. However, a magnetic field could be generated by a magnet, or through the electromagnetism phenomena i.e., current-carrying wires, solenoids or electromagnets. Figure 1.18 illustrates some examples of the magnetic field lines, where Figure1.18(a) shows a uniform magnetic field between two unlike magnetic poles (North and south pole), case (d) represents a magnetic dipole, on the other hand, Figures 1.18 (b), (c) and (e) show the generated magnetic field through the flow of a steady electrical current in current-carrying wire, a solenoid and a small current-carrying wire loop, respectively.
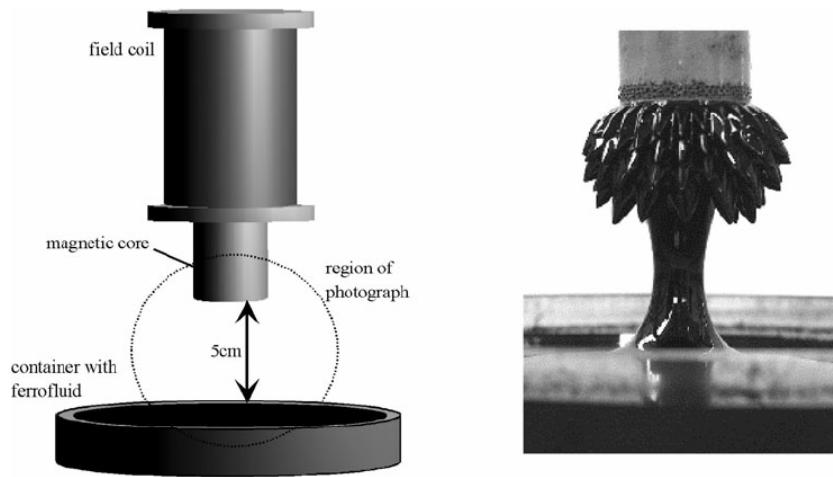
Figure 1.17: Ferrofluid under the effect of the magnetic forces generated by electromagnet [19]
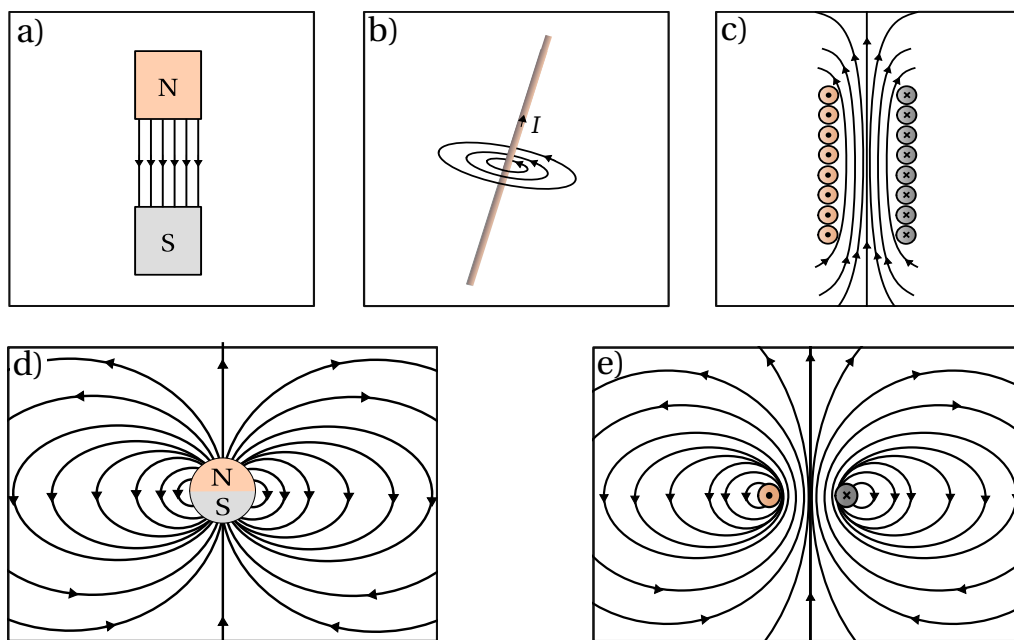
Figure 1.18: Schematic view of magnetic fields lines for different configurations.

The magnetization which is denoted by the vector $\vec{M}$ in equation (1.2), represents the state of polarization of a magnetic material in general [22] or the dipole moment per unite volume [21] . Therefore, there are six main types of magnetic behaviour based on the magnetic dipole moments alignment (magnetic ordering) of the magnetic material in presence and absence of a magnetic field $\vec{H}$ i.e. [17], [23], [24]:

a) Ferromagnetic; when the magnetic dipole moments of the particles align in parallel in absence of the magnetic field (see Figure 1.19a) and bellow Curie temperature because above the Curie temperature the alignment will be destroyed and the ferromagnetic materials lose their permanent magnetic properties, consequently, their behaviour becomes similar to the paramagnetic materials [25].
b) Antiferromagnetic; This materials exhibit an anti-parallel distribution of the adjacent dipoles (Figure 1.19b)), this kind of material have a weak magnetism .
c) Ferrimagnetic; Similar to the antiferromagnetic materials in the behaviour, but the magnetic dipoles do not have the same size as it dimenstrated in Figure 1.19c).
d) Diamgnetic; In absence of a magnetic field, this kind of materials do not show any magnetic dipole, but in the opposite case where $H \neq 0$ the magnetization of this materials is opposite to the magnetic field direction (Figure 1.19d).
e) Paramagnetic; this type of materials have an aleatory arrangement of the magnetic dipole when $H = 0$. However, if $H \neq 0$ the alignment of the magnetic dipole moments take partially the same direction of the applied magnetic field (Figure 1.19e).
f) Superparamagnetic; The superparamagneic materials magnetically behave similar to the paramagnetic ones (the magnetic moment dipoles are parallel to the applied magnetic field), but they have higher magnetization (Figure 1.19f).

In Figure 1.20, it can be seen clearly the typical curves that evaluate the behaviour of the magnetisation in function of the applied magnetic field, which depends on the material type. The magnetization in diamagnetic materials develops linearly by the increase of the magnetic field with a negative slope (1.20 a), where the slop represents the magnetic susceptibility (χ). The magnetization of paramagnetic materials have the same linear behaviour but with a positive slope. On the other hand, for the ferromagnetic and the superpamagnetic materials cases (Figures 1.20 c and d), the curves M versus H, exhibit a sigmoid behaviour. It is noteworthy to mention that unlike the paramagnetic materials, the ferromagnetic materials magnetization curve shows a hysteresis loop due to the ability of this last to remain magnetized even in absence of the magnetic field. However, it is worth noting that the colloidal ferrofluids belongs to the superparamgnetic category [17].
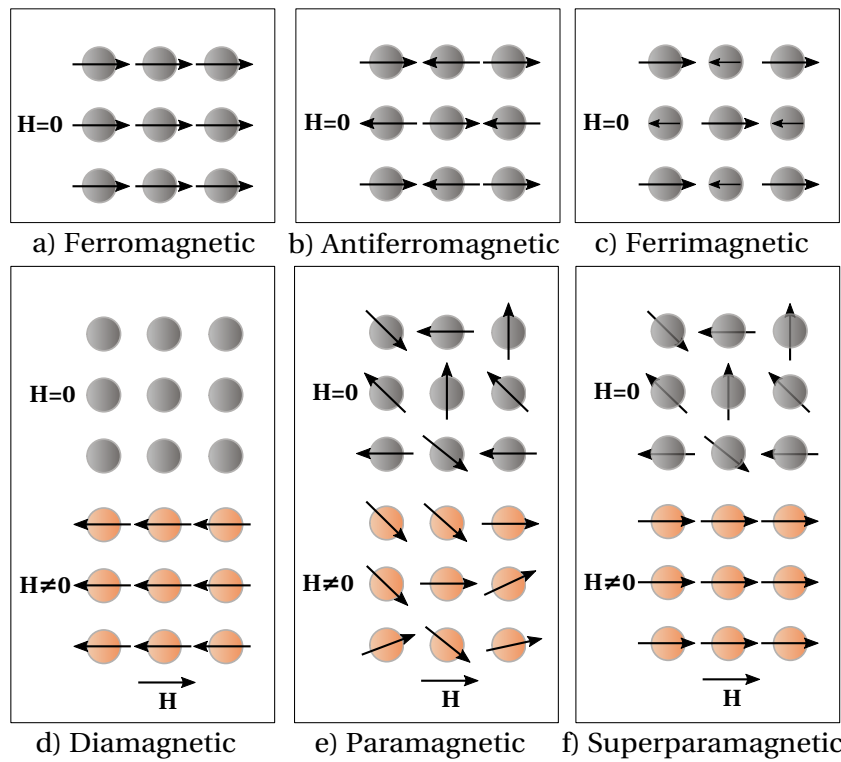
Figure 1.19: The magnetic materials behaviour in presence and absence of a magnetic field [23] [24].
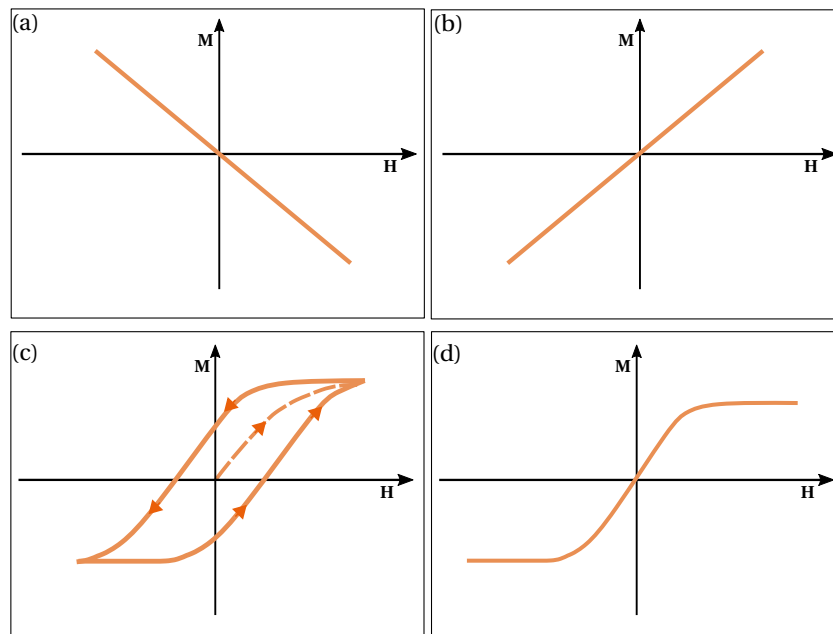
Figure 1.20: Different types of the theoretical magnetization curves versus the magnetic field intensity; a) Diamagnetic material b)Paramagnetic material c)Ferromagnetic material d)Superparamagnetic material [23].

1.3.3 Ferrofluids applications

Due to the possibility of controlling ferrofluids by the means of magnetic field, the use of ferrofluids in different applications attract the researchers from many fields, similar to:

1.3.3.1 Medical uses

The ferrofluids are used as contrast agent to enhance the quality of the obtained images from magnetic resonance imaging (MRI). The magnetic hyperthermia, another application uses the ferrofluids as a cancer treatment, either by driving the the magnetic suspensions to a target cell in order to damage it increasing its temperature locally or by magnetic field guided drug delivery as it is shown in Figure 1.21 [26], [27].
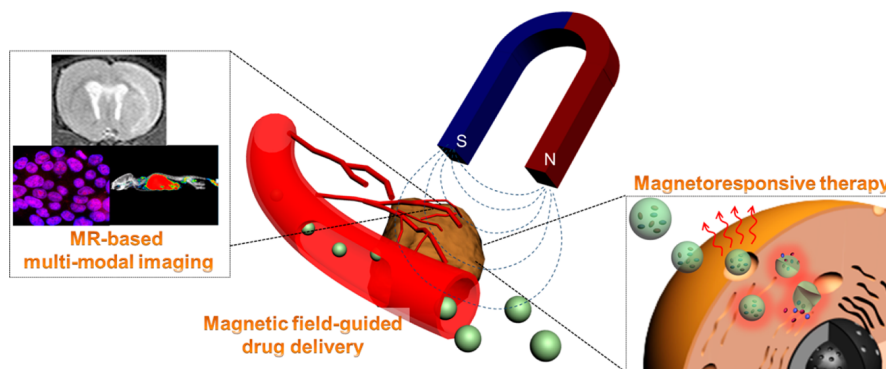
Figure 1.21: The medical uses of ferrofluids, Magnetic resonance imaging, drug delivery, magnetic hyperthermia [27].

1.3.3.2 Electronics field

Several electronics companies use the ferrofluids to enhance the performance of the speakers and car HiFi audio systems, by reducing the sonic distortion unlike the conventional ones which create the distortion due to dumper vibrations (See Figure 1.22). Moreover, the use of ferrofluids as a coolant in presence of strong magnetic field in the speakers, reduce energy consumption of these last [28].

Figure 1.22: A loudspeaker with ferrofluids [29].

1.3.3.3 Mechanical sealing

Because of its negligible friction in presence of a strong magnetic field which is due to its ability to keep its liquid properties at this condition, the ferrofluid provides a good solution for rotating shaft sealing where the low friction is needed, like in hard disk drives [28]. Figure 1.23 shows a 3D model for the sealing mechanism using ferrofluids and permanent magnets.
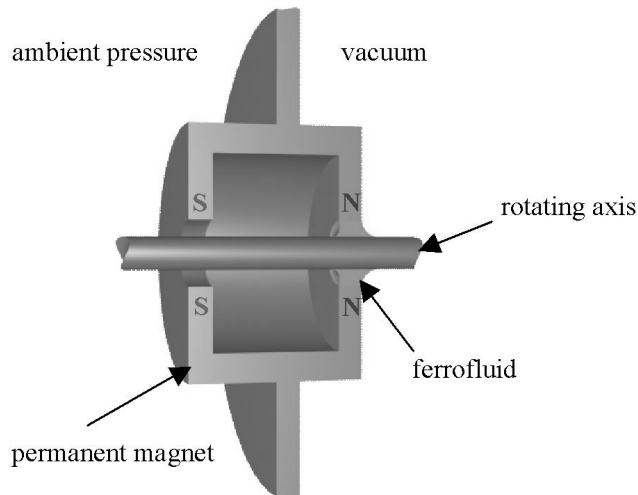
Figure 1.23: Three dimensional illustration for the sealing of a rotating axis using the ferrofluid [28].

1.3.3.4 Adaptive optics systems

The adaptive optics systems are used in many optic fields like astronomy. In this regard, the liquid deformable mirrors (MLDMs) could be one of innovative solutions, this technique uses the ferrofluids and reflective coating made of silver nanoparticles or a thin film of Poly-dimethylsiloxa [30], while the magnetic field represents the mechanism behind the surface deformation and manipulation (Figure 1.24).
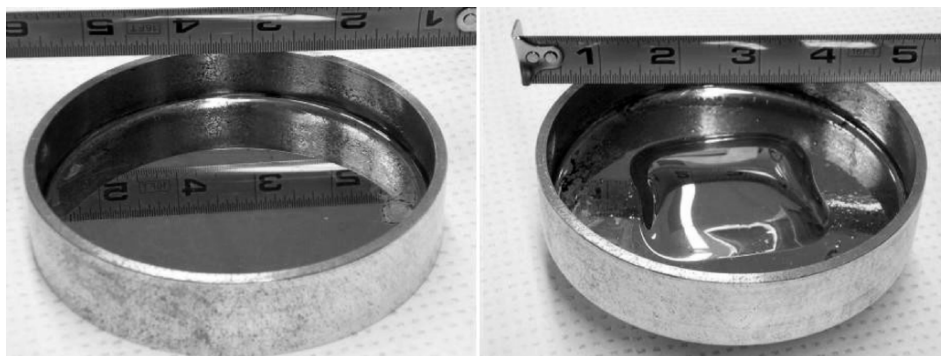
Figure 1.24: Photo of liquid deformable mirror made ferrofluid and silver nanoparticles, in presence and absence of a magnetic field. [31].

1.4 Ferrofluids for heat transfer enhancement (a review)

In the last decades, ferrofluids are attracting the interest of researchers as promising heat transfer fluids (HTF), due to the enhancement of the base fluid thermal properties (thermal conductivity) and the flow controllability by applying external magnetic forces [32], [33], so, it can be considered as a compound technique that combines a passive method (adding nanoparticles to a base fluid) and active method ,using electromagnetic field or it can be considered as a passive technique if the magnetic field is generated by a permanent magnet.

Considering the fluid layer in Figure 1.25, in presence of an external magnetic field and a temperature gradient, the volume element M of the magnetized fluid (ferrofluid) moves from position M_1 in the direction of temperature and the magnetic gradients toward the magnetic source to position M_2 driven by the kelvin body force, due to higher magnetization of this volume element comparing to the fluid around it, the volume element will experience a force anti-parallel to field gradients (∇T and ∇H), consequently this volume element will displace from position M_2 to M_1 [18], [28]. This convection phenomena is termed thermomagnetic convection.
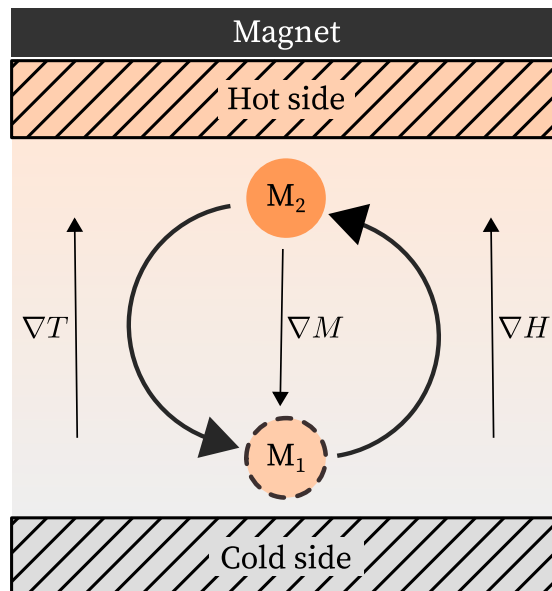
Figure 1.25: A sketch for the thermomagentic convection principle.

Früh [34] studied experimentally and numerically, the thermomagnetic convection under the effect of magnetic field. The results showed that a weak magnetic fields can enhance slightly the heat transfer. **Szabo et al.** [35] investigated experimentally and numerically the effect of non uniform magnetic field on the thermomagnetic convection, they concluded that the augmentation in temperature difference increases the buoyancy and the kelvin body forces. They reported also that the Kelvin body force is grater than the buoyancy, by comparing both forces calculating the convection ratio, magnetic Rayleigh number over convectional Rayleigh number.

The magneto-caloric cooling devices, are one of the interesting practical applications of the thermomagnetic convection. In this regard, **Pattanaik et al.**[36] conduced experimental

and numerical studies, where they analyzed a passive cooling device in which they involved the thermomagnetic phenomena using the commercial ferrofluid (Fe_3O_4/*Organic ester oil*) as heat transfer fluid and a permanent magnet (the experimental setup is illustrated in Figure 1.26), the obtained results showed that the local Nusselt number achieved a maximum values near to the magnet position.The average Nusselt number increased correspondingly to the increase of the heat load and the maximum value. Furthermore, the researchers were able to cool the heat load by 41°C for heat flux equals to 8.85 kW/m². it is noteworthy to mention that the developed device is self-pumping and self-regulating.
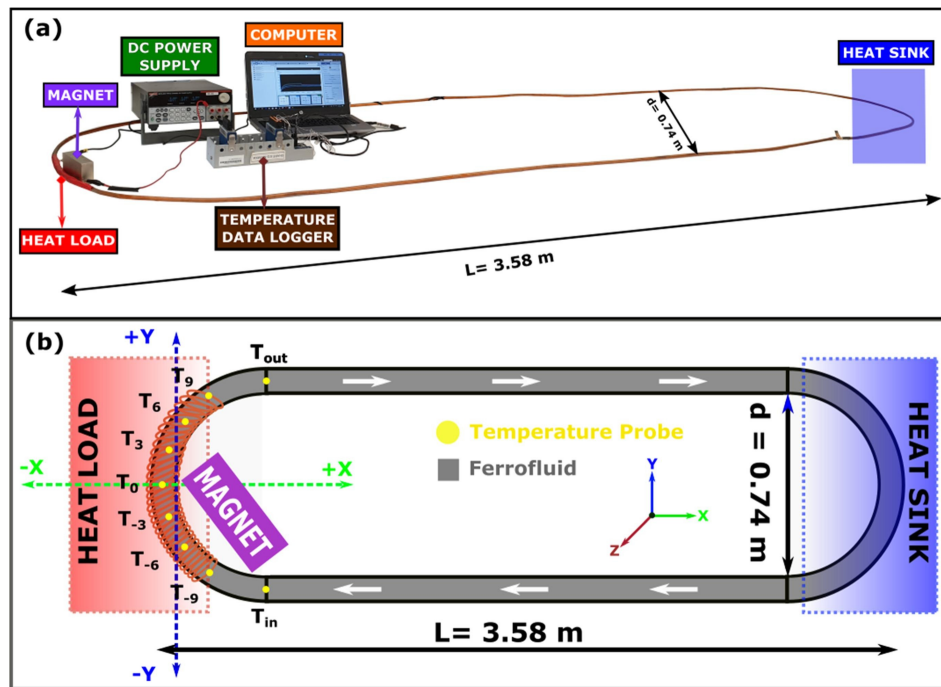
Figure 1.26: a) The experimental setup of the passive cooling device, b) schema of the studied system [36].

Kumar et al.[37] investigated experimentally and numerically the effect of using ferrofluids in presence of induced magnetic field of a micro current-carrying wire, on its cooling process, where the wire was submerged in ferrofluid as it is demonstrated in Figure 1.27a, they found that the convective heat transfer enhanced using the ferrofluids as a coolant instead of using the deionized water, Figure 1.27b gives a clear view about the Nusselt number enhancement. They pointed out, that the generated induced magnetic field around the wire has contributed in the cooling enhancement, as a clear indication for the thermomagnetic convection phenomena. Moreover, the authors reported that the type of the wire material plays a critical role in the strength of the generated magnetic field, accordingly, the thermomagnetic convection efficiency.

As a promising application **Zanella et al.**[38] invested in this phenomena by using 1 Vol % ferrofluid (Fe_3O_4/*Transformer oil*) as a cooling fluid in a 40 kVA electrical transformer, they were able to decrease the temperature of the transformer by additional 2.2°C in comparison with the transformer oil case.
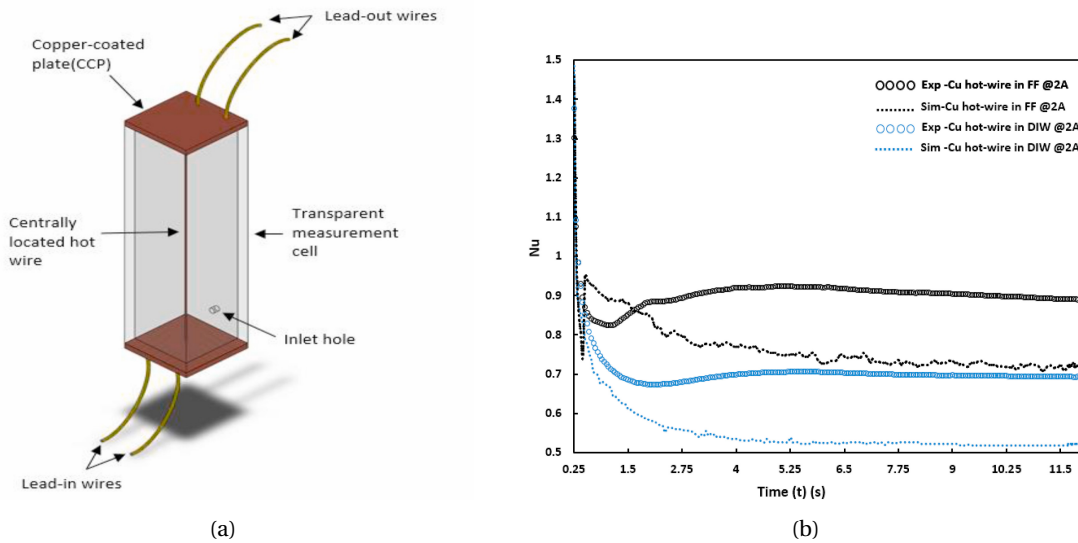
Figure 1.27: (a) The studied configuration, (b) A comparison of Nusselt number as a function of time for ferrofluid and deionized water cases (I=2A) [37].

On the other hand, several studies have been carried out by different research groups to characterize the ferrofluid forced flows in ducts with heat transfer and under the magnetic forces effect.

Buschmann. [39] summarized in his review the mechanisms behind the heat transfer enhancement in straight ducts, using ferrofluids under the effect of external magnetic field, in which he analyzed 18 experimental works ranged between laminar and turbulent regime. He organized this mechanisms as interactions between, viscous, inertial and magnetic forces as it is illustrated in Figure 1.28. Therefor, the strength of the magnetic field plays the important role i.e., if the ferrofluid flow is under the effect of weak magnetic field, the nanoparticles will form chain-like agglomeration, an increase in the magnetic field intensity generates secondary flows and if the magnetic field became very strong, the magnetic nanoparticles will pin near to the magnetic field source forming an obstacle. However, the lion's share of the studied cases of heat transfer enhancement in forced flows using ferrofluid, was for magnetic field generated by current-carrying wire, where **Shakiba et al.** [40] tested numerically the effect of a non-uniform magnetic field (MF) generated by a straight current-carrying wire on the flow of ferrofluid in the inner tube of a double pipe heat exchanger. They reported that the force (Kelvin body force) produced by the interaction between the MF and the ferrofluid generated secondary flows that boosted the convective heat transfer in the heat exchanger.

Another study by **Larimi et al.** [41] investigated numerically the influence of the MF generated via multiple wires parallels to each other and perpendicular to the ferrofluid flow in a ribbed channel for laminar flow conditions and various wire configurations. It was found that the presence of the MF increases the Nusselt number (especially for low Reynolds numbers), but also the pressure drop. The maximum increase was observed for the arrangement of all wires under the channel.
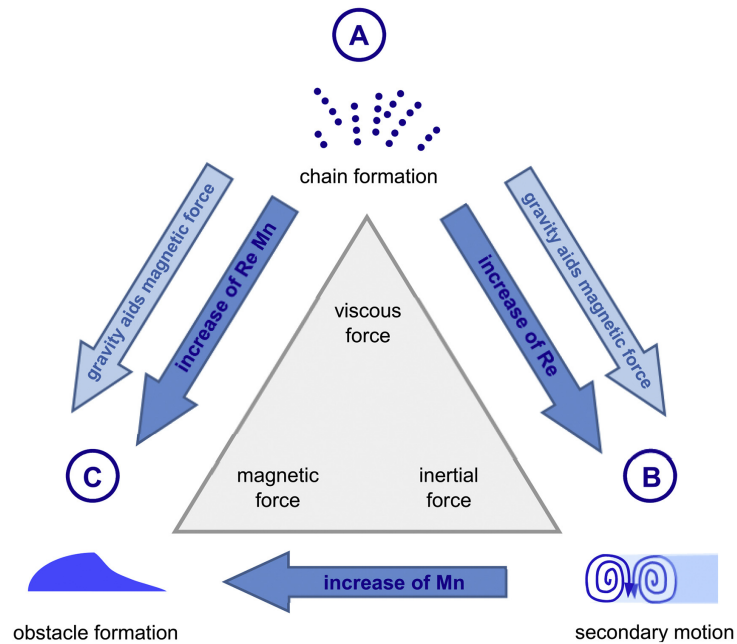
Figure 1.28: The interactions between the viscous inertial and magnetic forces (Mn denotes the magnetic number) [39].

Soltanipour et al. [42] developed a numerical model to study the effect of an external magnetic field over a curved tube. This work was the first one to cover the influence of the current-carrying wire angular position on the flow characteristics. The results showed that the flow patterns (number of vortices and position) were strongly influenced by the wire position. The authors found that the optimal wire position corresponds to $\varphi = 180°$ (measured as the counter-clockwise angle with the horizontal axis), where the Kelvin force promotes the secondary flow recirculations produced by the tube curvature. The maximum heat transfer enhancement measured was about 29%.

Yousefi et al. [43] analysed numerically the effect of the location and the number of straight current-carrying wires on flow pattern and the thermal-hydraulic characteristics of ferrofluid laminar flow in a flattened tube. The study concluded that the secondary flows generated by the MF improved the heat transfer coefficient and increased the pressure drop. In addition, the position of the wires plays a major role in the number and the size of the vortices generated. Moreover, the configuration with two parallel wires placed at the top and bottom parts of the tube (flat sides of the tube) provided the highest heat transfer coefficient and pressure drop. Figure 1.29 shows the cross-sectional views of the velocity contours, the streamlines and the distribution of temperature and the kelvin body force, for the studied configurations.

In the thermal solar field, one of the first studies to conceive the application of ferrofluids and an external magnetic field in parabolic trough solar collectors was performed by **Khosravi et al.** [44]. Their numerical study was focused on the turbulent region ($15 \cdot 10^3 < Re < 250 \cdot 10^3$). The different operating conditions were specified to those expected in the studied application: Therminol 66 was selected as HTF and the collector tube received a non-uniform heat flux. The

results showed a significant increase on the Nusselt number and the friction factor when the magnetic field was applied. The authors concluded that the best performance was obtained when a 4 vol% Fe_3O_4-Therminol 66 mixture was used under the maximum magnetic field tested (500 G).

Malekan et al. [45] extended the previous study to include different nanoparticles (CuO), nanoparticle size and the use of internal fins. The authors found that the Fe_3O_4 particles of the smallest size (10 nm) provided a higher heat transfer enhancement. Under external magnetic field, the introduction of the internal fins provided a modest increase on the performance evaluation criterion and a similar levelized cost of energy when compared to a smooth tube.
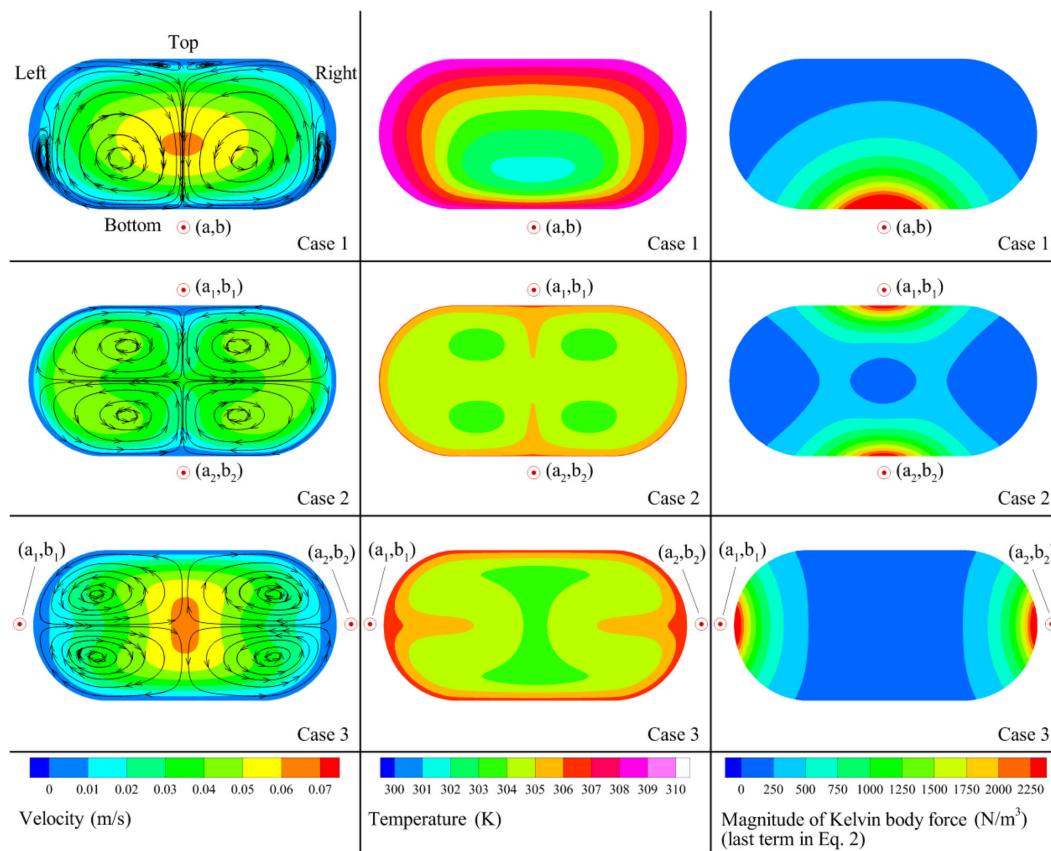
Figure 1.29: Velocity contours, the streamlines, the temperature and kelvin body force contours of ferrofluid laminar flow in flattened tube (φ = 4.3 %, Re = 300, I=5A) [43].

In 2018 **Alsaady et al.** [46] as well, invested in the electromagnetism phenomena, where they analyzed experimentally the effect of using ferrofluids in an experimental prototype of parabolic trough solar collector with electromagnets, as it can be noticed in Figure 1.30 the proposed configuration was different from **Malekan et al.** works. Although, the results approved that using Fe_3O_4 water based ferrofluids enhances the thermal efficiency in absence of the magnetic forces by 16% compared to its base fluid. Likewise, in presence of the magnetic field, the efficiency increases more.
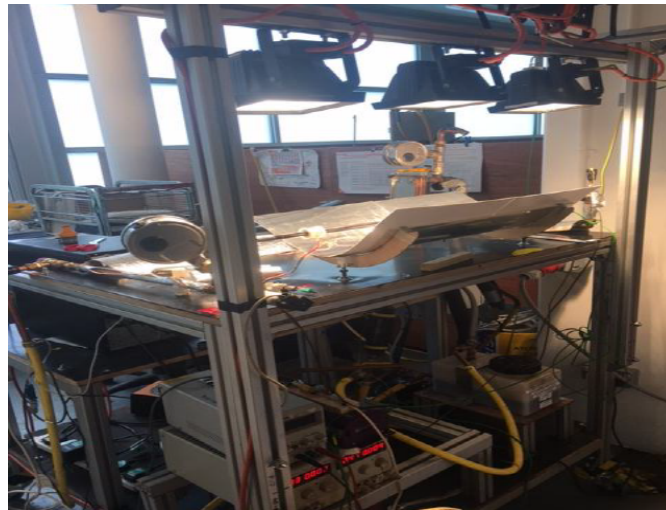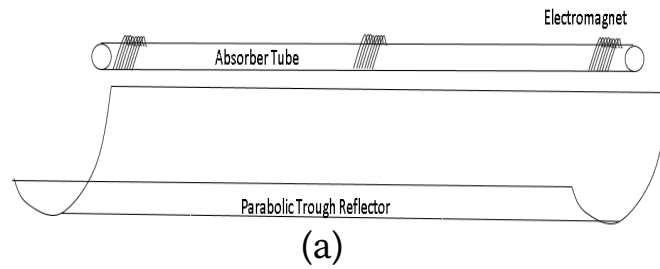
Figure 1.30: a) a sketch for the proposed parabolic trough solar collector. b) The experimental facilities [46].

1.5 Conclusions

The race toward the design of reliable heat transfer enhancement techniques created a variety of methods and solutions. These methods are classified into two main categories passive or active, based on their need to an external energy. The combination between passive and active methods is defined as a compound method.

The ferrofluids are synthetic colloidal liquids made of carrier liquids and nanoparticles, where the used nanoparticles characterized by their magnetic properties. In presence of a magnetic field, the magnetic nanoparticles align in the direction of this field, based on this behaviour the magnetic nanoparticles are classified as superparamagnetic materials.

The magnetic characteristics of the ferrofluids made the motion control of this last possible via the magnetic fields, which are generated either by magnets or electromagnets. The interaction between the a magnetic field and the ferrofluids creates the so-called kelvin body force, this feature opened doors for many application in various fields, among them the heat transfer enhancement.

Based on the literature review (section 1.4), it is clear that ferrofluids under magnetic field effects as a heat transfer enhancement technique provide promising results, even for the parabolic trough solar collectors which is one of the interests of the present thesis. However, as it can be observed that the most studies in forced flows involved the electromagnetism

through using current-carrying wires as magnetic field sources. In addition, it is noticed that all the works in this regard, considered only an axially uniform magnetic field along the flow ducts generated by a straight current-carrying wire, while other wire configurations have not been considered. This option appears as a reasonable solution for a higher heat transfer enhancement without a significant cost increase.

2 Mathematical formulation and methodology

2.1 Introduction

This chapter presents the governing equations that describe mathematically the ferrofluid flow under the effect of a magnetic field, the equations of electromagnetism and magnetization, as well as the used ferrofluid's thermo-physical proprieties correlations for this study. On the other hand, the chapter goes into the different used simulation steps to resolve such problem numerically via the commercial Computational Fluid Dynamics code ANSYS Fluent. Finally, the chapter discusses the non-dimensional numbers related to this study.

2.2 The governing equations

The governing equations which represents the interaction between the magnetic field and ferrofluid flows are derived from the coupling between the Navier-Stokes equations and the electromagnetism forces.

2.2.1 Navier-Stokes and energy equations

Before introducing the continuity, Navier-Stokes and energy equations, it is important to consider the following assumptions for the ferrofluid [47]:

1. The thermo-physical proprieties are constant thermo-physical properties.

2. The magnetic nanoparticles are in thermal equilibrium with the base fluid.

3. No velocity slip between the magnetic nanoparticles and the base fluid.

4. The ferrofluid is homogeneous.

5. The ferrofluid is incompressible fluid.

6. Single phase.

7. Considered as Newtonian fluid.

8. Gravity effect is neglected.

9. Considered as electrically non-conductive.

2.2.1.1 The continuity equation

Taking into account the previous assumptions and assuming that the ferrofluid is steady, therefore:

$$\nabla \cdot (\rho_f \vec{V}) = 0 \tag{2.1}$$

where: ρ_f denotes the ferrofluid density and $\vec{V}$ refers for the ferrofluid flow velocity vector.

2.2.1.2 The ferrohydrodynamic momentum equation

The interaction between the ferrofluid and a magnetic field rises the so-called Kelvin body force, which is expressed mathematically by adding the Kelvin body force term $\vec{F}_k$ to the right hand side (RHS) of the momentum equation, therefore:

$$\rho_f(\vec{V} \cdot \nabla \vec{V}) = -\nabla p + \mu_f \nabla^2 \vec{V} + \vec{F}_k \tag{2.2}$$

where p stands for the pressure and μ_f the dynamic viscosity of the ferrofluid.

2.2.1.3 Energy equation

By neglecting the magneto-caloric, Joule heating and radiation effects, the energy equation for the studied cases is expressed by:

$$\vec{V} \nabla T = \frac{k_f}{\rho_f C_{p,f}} \Delta T \tag{2.3}$$

It is noteworthy to mention that T refers for the temperature, k_f and $C_{p,f}$ are the thermal conductivity and the specific heat of the ferrofluid, respectively.

2.2.2 The electromagnetic forces

2.2.2.1 Kelvin body force

Below, the kelvin body force expression as it is defined in the electromagnetic theory[21]:

$$\vec{F}_k = \mu_0(\vec{M} \cdot \nabla)\vec{H} \tag{2.4}$$

where:

μ_0: free space or vacuum permeability.
$\vec{M}$: the magnetization vector.
$\vec{H}$: the magnetic field.
Assuming that the magnetization $\vec{M}$ and the magnetic field $\vec{H}$ are collinear which allows to write the equivalence of magnetization vector $\vec{M}$ in term of the magnetic field unit vector $\hat{e}_H$:

$$\vec{M} \equiv M\hat{e}_H \equiv M\frac{\vec{H}}{H} \qquad (\text{ because } \hat{e}_H = \frac{\vec{H}}{H}) \tag{2.5}$$

here M and H are the magnitudes of $\overrightarrow{M}$ and $\overrightarrow{H}$ successively.

Replacing the magnetization in equation (2.4) by its equivalence (equation 2.5), yields:

$$\overrightarrow{F_k} = \mu_0 \frac{M}{H}(\overrightarrow{H} \cdot \nabla)\overrightarrow{H} \tag{2.6}$$

Substituting the vector identity $(\overrightarrow{H} \cdot \nabla)\overrightarrow{H} = \frac{1}{2}\nabla(\overrightarrow{H} \cdot \overrightarrow{H}) - \overrightarrow{H} \times (\nabla \times \overrightarrow{H})$ in equation (2.6), gives:

$$\overrightarrow{F_k} = \mu_0 \frac{M}{H}\left(\frac{1}{2}\nabla(\overrightarrow{H} \cdot \overrightarrow{H}) - \overrightarrow{H} \times (\nabla \times \overrightarrow{H})\right) \tag{2.7}$$

Taking into account Maxwell's equation $\nabla \times \overrightarrow{H} = \overrightarrow{J}$ (where $\overrightarrow{J}$ denotes the total electric current density) and by neglecting the electrical conductivity of the ferrofluid, then J=0, therefore:

$$\overrightarrow{F_k} = \mu_0 \frac{M}{H}\left(\frac{1}{2}\nabla(\overrightarrow{H} \cdot \overrightarrow{H}) - \overrightarrow{H} \times \overset{0}{\cancel{(\nabla \times \overrightarrow{H})}}\right) \tag{2.8}$$

Knowing that the dot product $(\overrightarrow{H} \cdot \overrightarrow{H}) = H^2$, then:

$$\overrightarrow{F_k} = \mu_0 \frac{M}{H}\frac{1}{2}\nabla(\overrightarrow{H} \cdot \overrightarrow{H}) = \mu_0 \frac{M}{H}\frac{1}{2}\nabla H^2 \tag{2.9}$$

Finally, the Kelvin body force can be reduced to:

$$\overrightarrow{F_k} = \mu_0 M \nabla H \tag{2.10}$$

In cartesian coordinates, the components of the Kelvin body force in the x, y and z directions, are respectively:

$$F_k(x) = \mu_0 M \frac{\partial H}{\partial x} \tag{2.11}$$

$$F_k(y) = \mu_0 M \frac{\partial H}{\partial y} \tag{2.12}$$

$$F_k(z) = \mu_0 M \frac{\partial H}{\partial z} \tag{2.13}$$

2.2.2.2 The magnetization force

As discussed earlier in the previous chapter, the ferrofluids are classified as a superparamagnetic materials in term of ferromagnetism behaviour. In spite of that, for the calculation of magnetization magnitude there exist various calculation formulas, including the following [48]:

$$M = K(T_c - T) \tag{2.14}$$

where K represents the pyromagnetic coefficient and T_c denotes the Curie temperature in which the magnetic materials start to experience a notable changes in their magnetic properties. For magnetite nanoparticles (Fe_3O_4), T_c=858°C.

Another expression for the magnetization uses the temperature as a variable and the constants, β (The critical exponent of the saturation magnetization), T_c, T_1 and M_1:

$$M = M_1 \left(\frac{T_c - T}{T_1} \right)^{\beta} \tag{2.15}$$

The third model calculate the magnetization in function of the constant K', the magnetic field intensity H, the Curie temperature T_c and the temperature T:

$$M = K'H(T_c - T) \tag{2.16}$$

However, the following model is used for the present study [32]:

$$M = M_s L(\xi) \tag{2.17}$$

Note that $L(\xi)$ refers for Langevin equation where $L(\xi) = coth(\xi) - \frac{1}{\xi}$, and M_s denotes the saturation magnetization which is represented in the curve of the magnetization in function of magnetic field intensity (Figure 2.1), and it can be calculated through the following relation:

$$M_s = Nm_p \tag{2.18}$$

The number of the particles per unit volume N, is calculated via the following formula:

$$N = \frac{\varphi}{V} \tag{2.19}$$

where φ is the fraction volume and V the nanoparticle volume (for the spherical nanoparticles $V = \frac{\pi d_p^3}{6}$ where d_p is the magnetic nanoparticle diameter).
Finally, by replacing each parameter with its expression, equation (2.17) becomes:

$$M = \frac{6\varphi m_p}{\pi d_p^3} (coth(\xi) - \frac{1}{\xi}) \tag{2.20}$$

The magnetic nanoparticle moment m_p and the Langevin parameter ξ are calculated by equations (2.21 and 2.22) successively:

$$m_p = \frac{4\mu_B \pi d_p^3}{6 \times 91.25 \times 10^{-30}} \tag{2.21}$$

$$\xi = \frac{\mu_0 m_p H}{k_B T} \tag{2.22}$$

where Bohr's magneton μ_B=9.27 × $10^{-24} A \cdot m^2$ and Boltzmann constant K_B=1.3806503 × $10^{-23} J/K$.
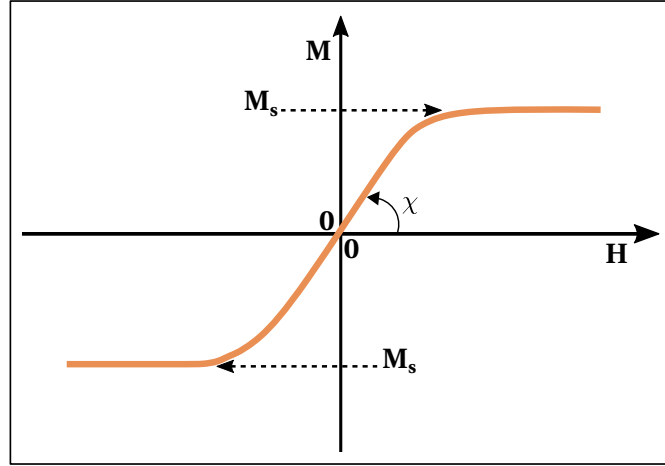
Figure 2.1: Superparamagnetic material theoretical curve of magnetization versus magnetic field intensity; [49]

2.2.2.3 The magnetic field

Among the different magnetic field generation methods, the current-carrying wire is chosen for all the studied cases in the present work. The mathematical expression that calculate the distribution of the arose magnetic field induction (B) when an electrical current flows through a thin current-carrying wire is given by the Biot-Savart law (equation 2.23).

$$B = \frac{\mu_0 I}{2\pi r} \tag{2.23}$$

Here, I denotes the electrical current and r is the distance from the wire.

The schema in Figure 2.2, illustrates a cross sectional view of the main studied configuration in the present work, which is composed of a tube filled with a ferrofluid and a thin current-carrying wire located at the bottom of the tube, where its position is defined in the Cartesian coordinate system (x,y), by the pair of coordinates (a,b).

The direction of the magnetic field induction $\overrightarrow{B}$ is circumferential around the wire, the magnitude of this field is constant at r distance from the wire forming the so-called Amperian loop as it is demonstrated in Figure 2.3.

As a step forward to derivate the mathematical expression that calculates the magnitude of the magnetic field H at any point from the space, lets consider the Cartesian coordinates system (x', y') centered on the wire center as it is illustrated in Figure 2.3, in such a way this coordinates system is related to the main coordinates system (x,y) Figure 2.2 through the relations bellow.

$$\begin{cases} x &= x' + a \\ y &= y' + b \end{cases} \tag{2.24}$$
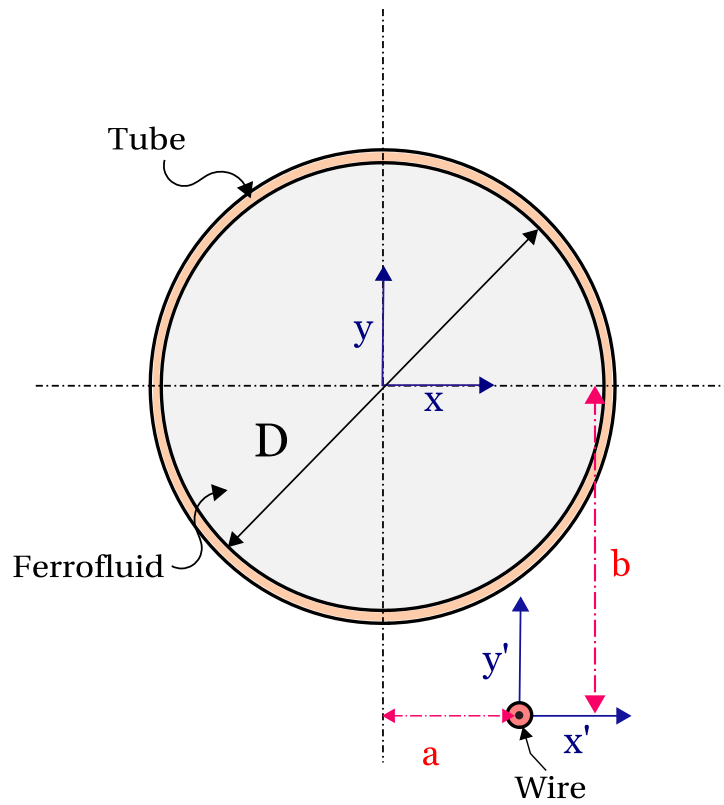
Figure 2.2: Schematic model for the principle behind the studied configurations.
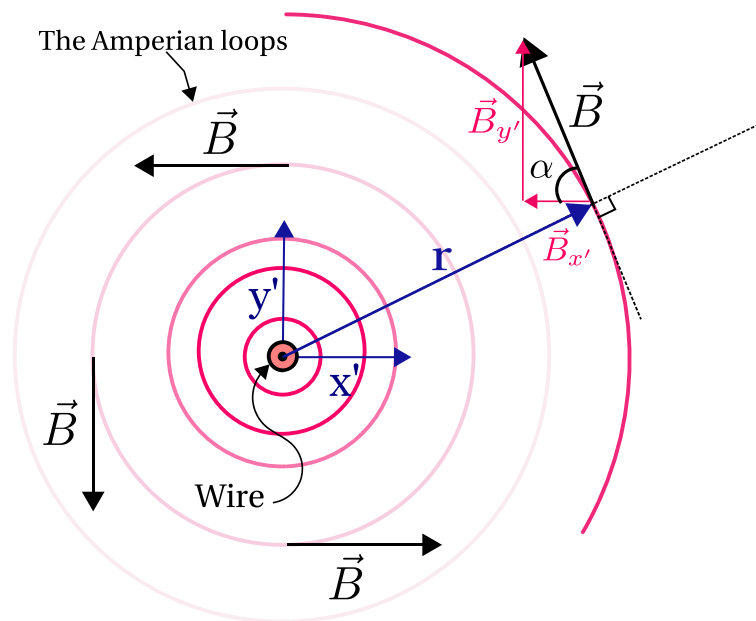
Figure 2.3: The magnetic field around the current-carrying wire.

The normal projection of the magnetic induction vector $\vec{B}$ on the axis x' and y', results the directional components of the magnetic induction vector, $\vec{B_{x'}}$ $\vec{B_{y'}}$ respectively. However, the following equations calculate the the magnitude of each component:

$$
\begin{aligned}
B_{x'}(x', y') &= -B\cos(\alpha) \\
&= -B\frac{y'}{r} \\
&= -\frac{\mu_0 I}{2\pi r}\frac{y'}{r} \\
&= -\frac{\mu_0 I}{2\pi}\frac{y'}{r^2}
\end{aligned}
\tag{2.25}
$$

$$
\begin{aligned}
B_{y'}(x', y') &= B\sin(\alpha) \\
&= B\frac{x'}{r} \\
&= \frac{\mu_0 I}{2\pi r}\frac{x'}{r} \\
&= \frac{\mu_0 I}{2\pi}\frac{x'}{r^2}
\end{aligned}
\tag{2.26}
$$

Through using the formula of radius in term of coordinates $r^2 = x'^2 + y'^2$, the equations 2.25 and 2.26 become:

$$
B_{x'}(x', y') = -\frac{\mu_0 I}{2\pi}\frac{y'}{x'^2 + y'^2}
\tag{2.27}
$$

$$
B_{y'}(x', y') = \frac{\mu_0 I}{2\pi}\frac{x'}{x'^2 + y'^2}
\tag{2.28}
$$

Via a frame reference transformation, form the wire coordinates system (x', y') to the tube coordinates system (main coordinates system) (x, y), using the relations below:

$$
\begin{cases} x &= x' + a \\ y &= y' + b \end{cases} \Longleftrightarrow \begin{cases} x' &= x - a \\ y' &= y - b \end{cases}
\tag{2.29}
$$

the equations 2.27 and 2.28 become successively:

$$
B_x(x, y) = \frac{\mu_0 I}{2\pi}\frac{(b - y)}{(x - a)^2 + (y - b)^2}
\tag{2.30}
$$

$$
B_y(x, y) = \frac{\mu_0 I}{2\pi}\frac{(x - a)}{(x - a)^2 + (y - b)^2}
\tag{2.31}
$$

The relation that relates the magnetic field magnitude with its magnetic induction is written

as[18]:

$$B = \mu_0 H + B_r \tag{2.32}$$

where B_r refers for the residual magnetization (the remanence) and it is negligible for magnetic nanoparticles (Superparamagnetic material)[50].

Hence

$$H = \frac{B}{\mu_0} \tag{2.33}$$

Therefore the value of the magnetic field directional components in Cartesian coordinates are written as:

$$H_x(x, y) = \frac{I}{2\pi} \frac{(b - y)}{(x - a)^2 + (y - b)^2} \tag{2.34}$$

$$H_y(x, y) = \frac{I}{2\pi} \frac{(x - a)}{(x - a)^2 + (y - b)^2} \tag{2.35}$$

The magnitude of the magnetic field (modulus of magnetic field vector) is given by:

$$|\vec{H}| = H(x, y) = \sqrt{H_x^2 + H_y^2} \tag{2.36}$$

The expression that calculates the magnitude of the magnetic field in function of the Cartesian coordinates (x, y) is therefore:

$$H(x, y) = \frac{I}{2\pi} \frac{1}{\sqrt{(x - a)^2 + (y - b)^2}} \tag{2.37}$$

2.3   Thermo-physical properties calculation

The dispersion of nanoparticles in a base fluid changes the thermo-physical properties of of this last. The properties of the ferrofluid are calculated using the thermo-physical properties of magnetic nanoparticles and the base fluid [51]:

2.3.1   Density

The density of the ferrofluid is calculated through the flowing correlation:

$$\rho_f = \varphi \rho_p + (1 - \varphi) \rho_b \tag{2.38}$$

where, ρ_f, ρ_p and ρ_b are the density of the ferrofluid, the magnetic nanoparticles and the base fluid, successively.

In addition, the volume fraction of the magnetic nanoparticles φ is the ratio between the

magnetic nanoparticles and the ferrofluid volumes and it is given by:

$$\varphi = \frac{V_p}{V_f} \tag{2.39}$$

2.3.2 The specific heat capacity

The specific heat capacity or the mass heat capacity of the ferrofluid is estimated by the following correlation [52]:

$$c_{p,f} = \varphi c_{p,p} + (1 - \varphi) c_{p,b} \tag{2.40}$$

2.3.3 Viscosity

The dynamic viscosity of the ferrofluid can be obtained through the fallowing formula:

$$\mu_f = (1 + 2.5\varphi)\mu_b \tag{2.41}$$

2.3.4 Thermal conductivity

The thermal conductivity which measures the ability of the material to transfer the heat via the conduction, is calculated using this equation [53]:

$$k_f = \left[\frac{k_p + (n-1)k_b - (n-1)\varphi(k_b - k_p)}{k_p + (n-1)k_b - \varphi(k_b - k_p)} \right] k_b \tag{2.42}$$

The empirical shape factor of the nanoparticles (n) is given by:

$$n = \frac{3}{\psi} \tag{2.43}$$

where the sphericity coefficient ψ depends on the shape of nanoparticle (See the table below).

Table 2.1: The sphericity coefficient and empirical shape factor of some typical nanoparticle shapes [54].

Nanoparticle shape	Aspect ratio	Sphericity ψ	Shape factor n
Sphere	-	1	3
Platelet	1:1/8	0.52	5.7
Cylinder	1:8	0.62	4.9
Brick	1:1:1	0.81	3.7

2.4 Numerical solution procedures

The present work combines between fluid mechanics, heat transfer and the electromagnetism. However, to resolve numerically the governing equations behind this multiphysics problem which are detailed in the previous section, the commercial computational fluid dynamics code ANSYS Fluent [55] is used.

ANSYS Fluent is based on the finite volume method (FVM). This method solves the governing partial differential equations (PDEs) at small finite control volumes [56]. The finite

volume method is mainly based on three fundamental steps, that can be resumed as follows [57]:

1. **Mesh generation**: By dividing the studied domain into finite volumes or sub-domains called cells (See Figure 2.4).

2. **Discretization**: By integrating the partial differential governing equations over each small control volume.

3. **Resolution of the equations**: By solving the system of equations, using an appropriate algorithm.
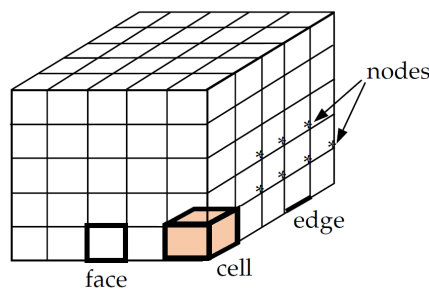
Figure 2.4: Simple 3D mesh [55]

2.4.1   Kelvin body force implementation

The Kelvin body force term (Equation 2.10) is added to the governing equation through implementing a user defined function (UDF) in ANSYS Fluent solver.

A user defined function is a C language program which is able to be dynamically loaded with the ANSYS Fluent solvers. The UDF as a tool, contributes in ANSYS Fluents' features enhancement. Like, defining a boundary conditions (e.g. a time depending boundary, a variable velocity, heat flux profile, moving wall...etc), material properties, source terms or even in the post-processing stage.

Figure 2.5, illustrates the main implementation possibilities of a UDF code in ANSYS Fluent solvers, as well as the UDF position on the solution process, in other words, the stage when the UDF code is called based on the solver i.e. pressure-based segregated solver, pressure-based coupled solver or density based coupled solver.

Similarly to a C language program, a UDF code includes a header file like "udf.h" or "math.h" (called by the command #include) and macros, where the definitions of the macros are included in the header files. In general, a user-defined function macro has the following form: DEFINE_MACRONAME(udf_name, passed-in variables) [58].

However, some of the macros are listed bellow [55]:

1. DEFINE_INIT; to initialize variables.

2. DEFINE_ADJUST; allows to manipulate variables.

3. DEFINE_PROPERTY; to specify a material property.

4. DEFINE_PROFILE; to implement a specific boundary condition.

5. DEFINE_SOURCE; to add a source terms to the governing equations.
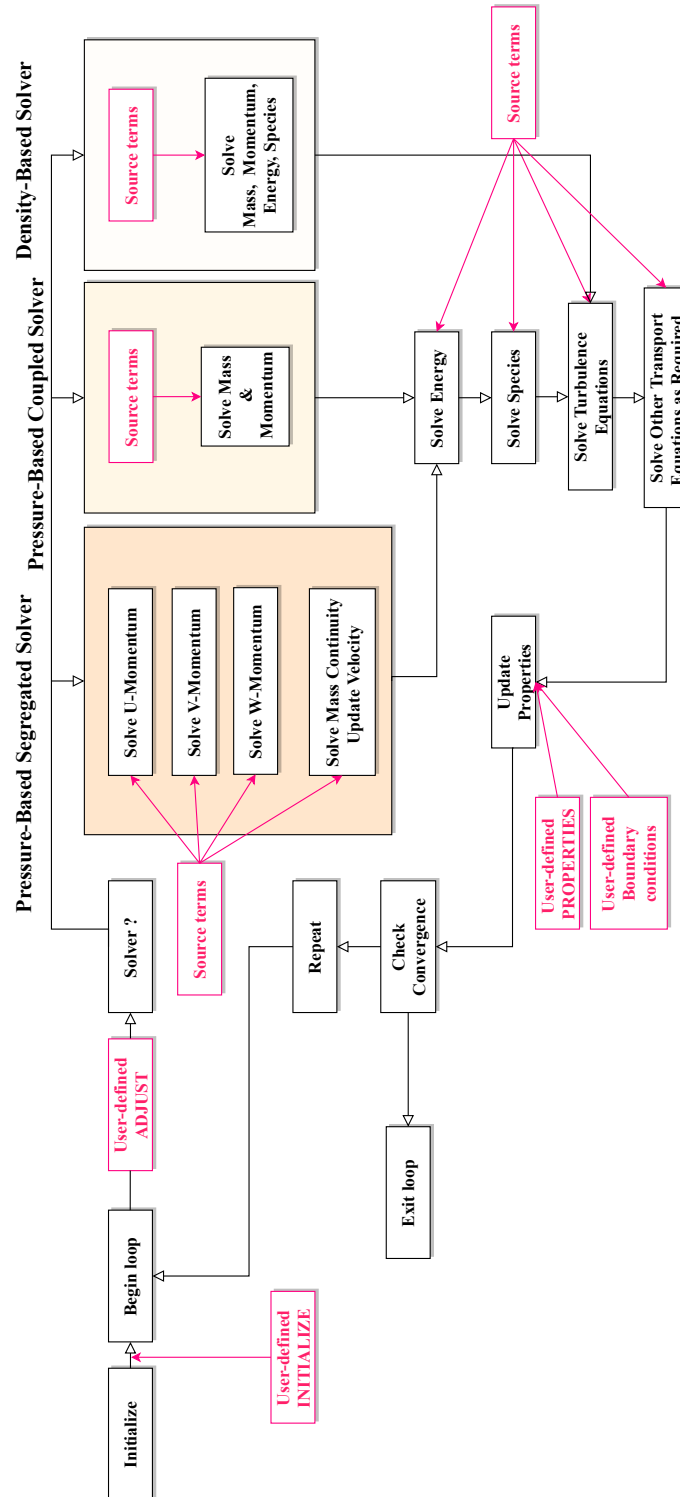
Figure 2.5: The main access points to ANSYS Fluent solver through a UDF[58] .

Since the only considered term from the interaction of magnetic field with ferrofluid flow in this study is the Kelvin body force, this last is added to the momentum equation as a source term, using the macro `DEFINE_SOURCE`, following the next steps:

1. Compiling the source code files that contains the UDFs.

2. Loading the compiled source file.

3. Enabling the Source Terms option in the dialog box activated in the cell zone condition (Fluid zone) (see Figure 2.6).

4. Hooking each UDF in its specific placement i.e. Kelvin body force x direction component in "X Momentum" and y direction component in "Y Momentum" dialog boxes (see Figure 2.6).
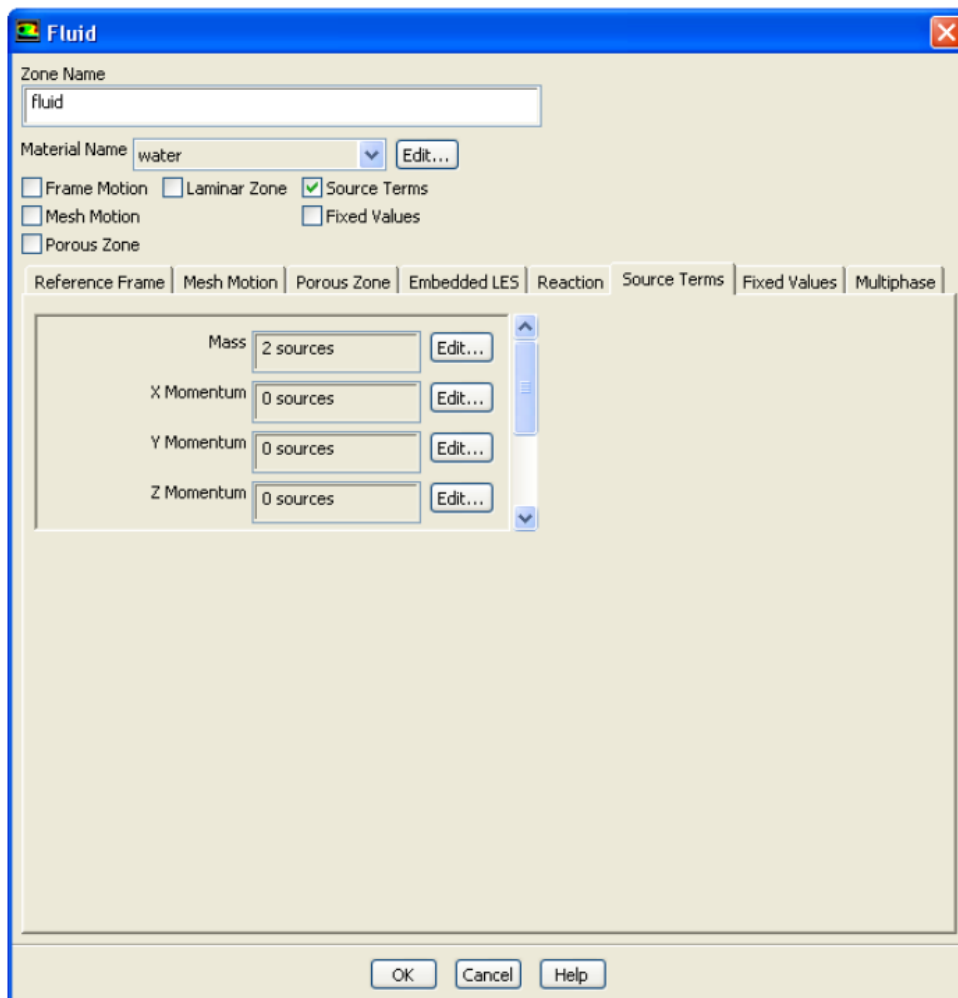
Figure 2.6: ANSYS Fluent cell zone dialog box [55]

2.4.2 The electromagnetic force model test

Before implementing the UDF file into Fluent software and as additional step, the numerical model of Kelvin body force was tested on 2D model of tube cross section using MATLAB software in order to see the agreement with the theory.

Figure 2.7 shows 2D plot of the magnetic field $\vec{H}$ generated by a current-carrying wire where the current is out of the paper. As it can be seen clearly, the vectors are tangent to the field lines (Amperian loops) and encircle the wire with a anticlockwise direction which follows the right hand thumb rule.

Figure 2.8 illustrates the magnetic field intensity contours, obviously the magnetic field intensity decreases when further away from the current-carrying wire center.

The plotted vectors of the magnetic field gradient ∇H and Kelvin body force $\vec{F_k}$ presented in Figures 2.9 and 2.10 respectively. By definition a gradient of a function is a vector quantity that points toward the maximum increase of this function [25]. Similarly, the gradient of the magnetic field modulus ∇H behaves in the same way, pointing in the direction of the maximum magnitude of the magnetic field (the current-carrying wire). As well as the Kelvin body force which is a function of magnetic field gradient (see equation 2.10).
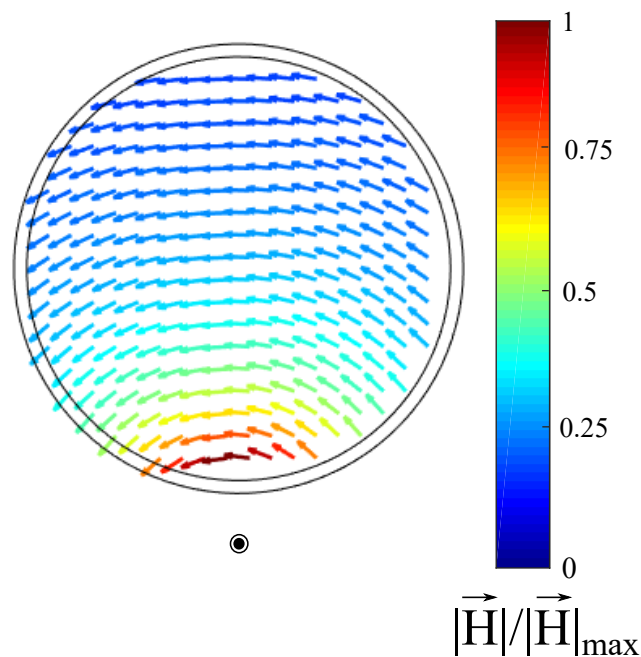
Figure 2.7: Vector field of the magnetic field intensity.
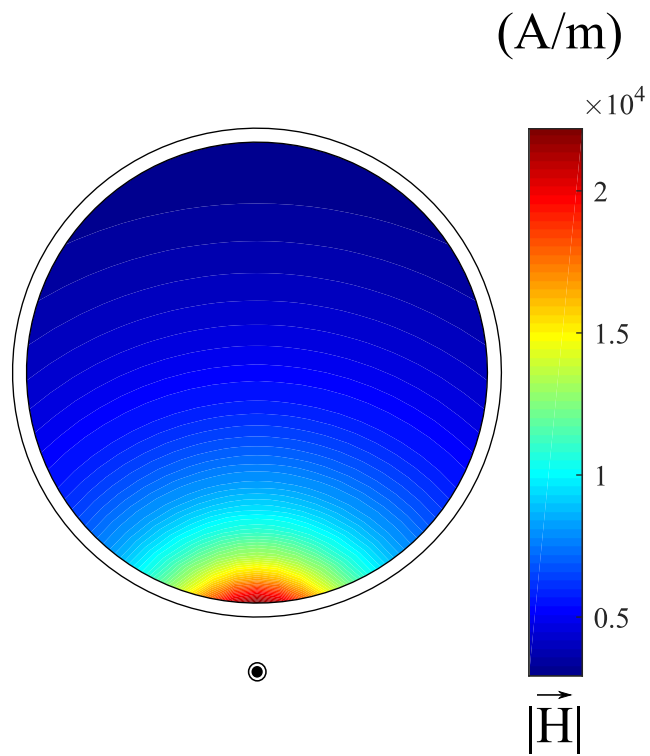
Figure 2.8: Modulus of the magnetic field intensity.
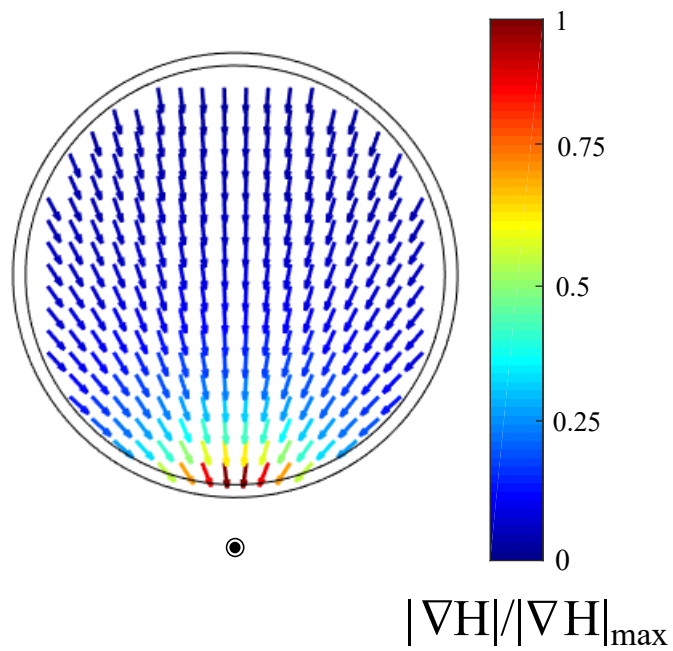
Figure 2.9: Gradient of the magnetic field.
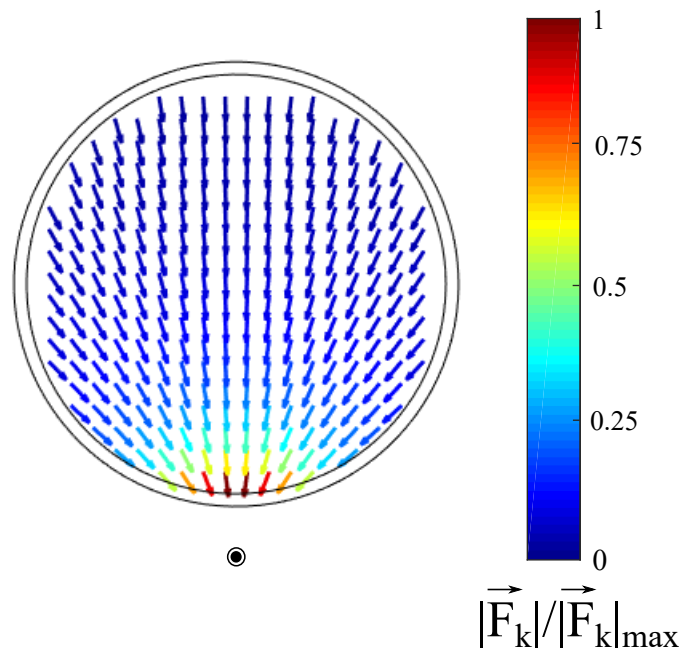
Figure 2.10: Kelvin body force.

2.4.3   Solver setup

In ANSYS Fluent there are two types of solvers, pressure based solver and density-based coupled solver. For the present study, the pressure-based solver is selected.

For the pressure-velocity coupling, ANSYS Fluent offers four different numerical algorithms:

1. Semi-Implicit Method for Pressure Linked Equations (SIMPLE).

2. Semi-Implicit Method for Pressure Linked Equations-Consistent (SIMPLEC).

3. The Pressure-Implicit with Splitting of Operators (PISO).

4. Coupled Algorithm.

However, due to its convergence rapidity, the Semi-Implicit Method for Pressure Linked Equations-Consistent algorithm is selected for all the studied cases in the present work. Figure 2.11 demonstrates the flowchart of this coupling algorithm.
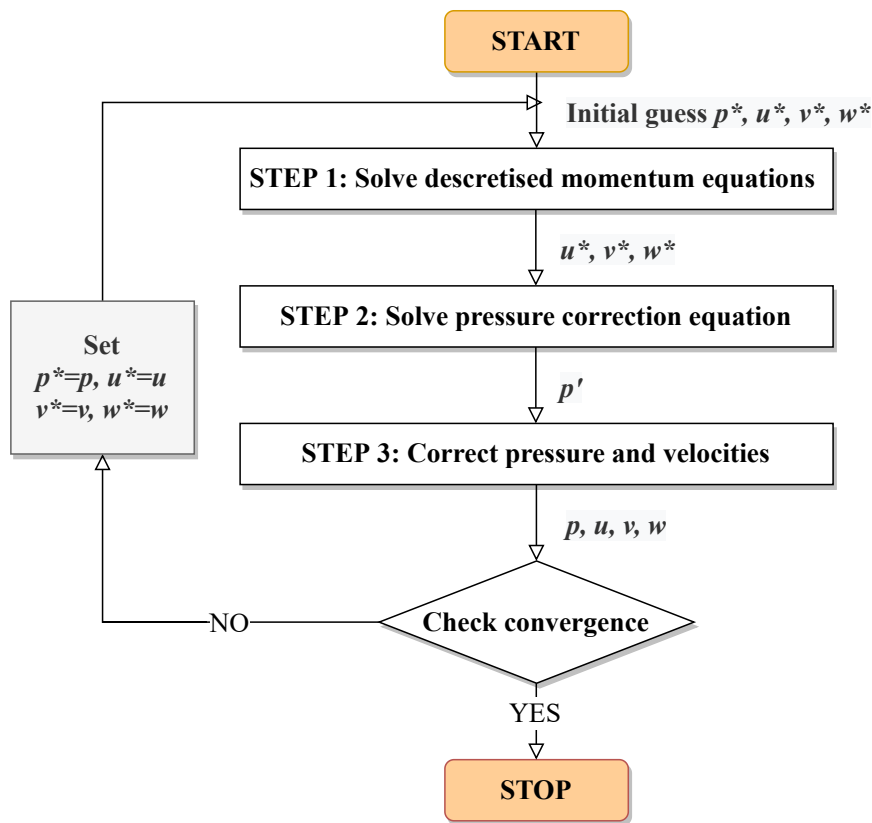
Figure 2.11: Semi-Implicit Method for Pressure Linked Equations-Consistent algorithm flowchart [59].

2.5 Data reduction

To evaluate the results and to compare fairly between them and against the data from the literature, it is important to transform the obtained data (temperatures, velocities, pressure...etc) into dimensionless numbers. The following subsections present the used dimensionless numbers.

2.5.1 Reynolds number

The Reynolds number quantifies the ratio between the inertial forces and the viscous ones [60].

$$Re = \frac{\text{inertial forces}}{\text{viscous forces}}$$

It was introduced for the first time by Reynolds in 1883. However, the utility of Reynolds number revolves around the fluid flow regime estimation or determination, if it is laminar or turbulent flow.

It is calculated as:

$$Re = \frac{\rho V D}{\mu} \tag{2.44}$$

2.5.2   Prandtl number

The Prandtl number which is named after the engineer Ludwig Prandtl, as an intrinsic number, the Prandtl number evaluates the importance of the momentum diffusivity to thermal diffusivity of a fluid [60].

$$Pr = \frac{\text{momentum diffusivity}}{\text{thermal diffusivity}}$$

Based on the fluid properties, the Prandtl number (Pr) is calculates as follow:

$$Pr = \frac{\nu}{\alpha} \tag{2.45}$$

where ν refers for the kinematic viscosity and α for the thermal diffusivity and $\alpha = \frac{k}{\rho c_p}$. Hence,

$$Pr = \frac{\mu c_p}{k} \tag{2.46}$$

2.5.3   friction factor

The friction factor is an important key to characterize the flow hydrodynamically, it gives an insight on how much the frictional losses in the flow channel (the pipe in our case). However, Darcy's friction factor formula is used for this study, which is defined by:

$$f = \frac{2\Delta P}{\rho_f V^2}\left(\frac{D}{L}\right) \tag{2.47}$$

where ΔP is the static pressure difference between the tube inlet and outlet, and L is the total length of the tube.

2.5.4   Nusselt number

Another important parameter for the heat transfer analysis is the Nusselt number which assesses the heat transfer by convection to heat transfer by conduction. is an important parameter that can contribute to a better rate of heat exchange. For the present work, the average Nusselt number (Nu)is calculated using equation 3.1 taking into consideration the axial variation of the heat transfer coefficient in the studied control volume.

$$Nu = \frac{h_{avg} \cdot D}{k} \tag{2.48}$$

The peripherally averaged heat convection coefficient, for each axial position, is calculated by:

$$\bar{h}(x) = \frac{q''}{\bar{T}_w(x) - T_b(x)} \tag{2.49}$$

where $\bar{T}_w(x)$ is the peripheral average of wall temperature at x, the axial position:

$$\bar{T}_w(x) = \frac{\sum_{i=1}^{n_{nodes}} T_i(x)}{n_{nodes}}; \forall i : r_i = D/2 \tag{2.50}$$

and $T_b(x)$ refers for the bulk temperature defined in [61], at the axial position x:

$$T_b(x) = \frac{\sum_{i=1}^{n_{cells}} \rho_i c_{pi} T_i(x) u_i(x) A_i}{\dot{m} c_p} \tag{2.51}$$

2.5.5 The Performance Evaluation Criterion

The chosen Performance Evaluation Criterion (PEC) model for this study to evaluate the heat exchange system, is computed as [62]:

$$PEC = \frac{(Nu/Nu_s)}{(f/f_s)^{1/3}} \tag{2.52}$$

Where Nu_s and f_s represent average Nusselt number and the friction factor for the reference case, respectively.

2.5.6 Magnetic number

The magnetic number (Mn), another important dimensionless number should be introduced for this study to quantify the effect of the magnetic field strength on the flow behaviour. The definition for the Magnetic number proposed by Soltanipour et al. [47] is used:

$$Mn = \frac{\mu_0 \chi H_r^2 D^2}{\rho_f v_f^2} \tag{2.53}$$

where, χ is the magnetic susceptibility (for this study χ=0.34859) and H_r is the characteristic magnetic field (the magnetic field calculated at the tube wall point), and d is the distance between the current-carrying wire and the tube wall, as it defined in Figure 2.12:

$$H_r = \frac{I}{2\pi d} \tag{2.54}$$

Although the position variation of the wire, H_r is constant along the axial direction, because the distance d is kept constant.
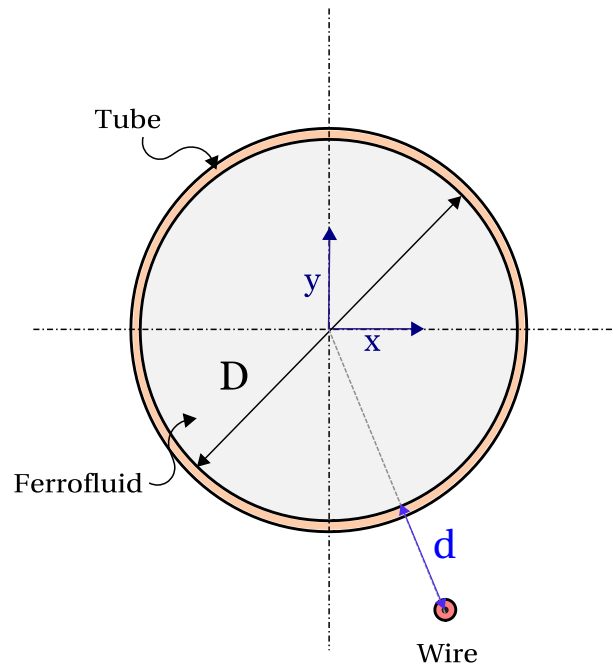
Figure 2.12: The definition of the distance d in the studied configuration.

2.6 Conclusions

The simplifying hypotheses for the present thesis, as well as the governing equations have been described in this chapter.

Considering the ferrofluids as electrically non-conductive (dielectric) and that the magnetization $\vec{M}$ is parallel to the magnetic field $\vec{H}$ led to reduced Kelvin body force term.

From the available magnetic field generation techniques, the current-carrying wire has been selected for all the studied cases in this study. Furthermore, the mathematical model of the generated magnetic field has been demonstrated in details from the Biot-Savart equation to the components of the magnetic field in function of the Cartesian coordinates.

ANSYS Fluent offers many access points to its solver via the user defined functions (UDFs), this feature allowed for the implementation of mathematical model of Kelvin body force in the momentum equation. This model has been tested and compared against the theory notions using MATLAB software.

However, the next two chapters will discuss the studied applications and the proposed configurations, as well as, the selected mesh type for the studied models and the numerical results for both flow regimes, the laminar and the turbulent.

3 Magnetic field effect on laminar flow

3.1 Introduction

Most of the analyzed studies which studied the influence of the non-uniform magnetic field generated by the current-carrying wires on the ferrofluid flows, have focused only on the straight configuration of the wire. Meanwhile, the majority of this studies agreed on the capacity of this technique to improve significantly the heat transfer by convection as an enhancement method.

On the other hand, the studies about the effect of the magnetic field created by wires with an arrangement differ from the straight wire configuration is virtually non-existent.

In this regard, the present numerical investigation is dedicated for the study of the effect of the magnetic field generated by a new current-carrying wire configuration, on the thermal and the hydraulic characteristics of Fe_3O4/ Water ferrofluid laminar flow in a smooth tube, where the tube is subjected to a uniform heat flux. The novel configuration is based on the periodic arrangement of the wire pitches (more details about the configuration will be explained in the next section).

3.2 Problem description

The ferrofluid which is composed of spherical nanoparticles of the magnetite (Fe_3O_4) with volume fraction $\varphi = 4\%$ and the water as a carrier fluid (Base fluid), enters the tube from the inlet as it is indicated in Figure 3.1, the ferrofluid flows in the direction of z axis. The inlet temperature of the ferrofluid is considered as uniform temperature where $T = T_{in}$ as well as the inlet velocity is considered uniform, with $V = V_{avg}$. The outer wall of the tube is subjected to a uniform heat flux (q''). The tube characteristics are shown in the table below.

Table 3.1: The tube parameters.

The length (L)	0.066 m
The diameter (D)	3 m
The thickness	Not considered

In order to generate a non-uniform magnetic field the tube is fitted with a current-carrying wire, this last is considered to have a periodic form. The periodic configuration is determined by l, the pitch length and θ the angle formed between the y axis and line that passes through

the wire cross-section and the tube centerline, like it is illustrated in Figure.3.1). And as it was mentioned earlier, when the electrical current I passes through the current-carrying wire, it generates a non-uniform magnetic field along the wire. However, it is worth mentioning that the only magnetic field generated by the wires parallel to the tube (the wire pitches represented with red lines in Figure 3.1) are taken into consideration for the present work, neglecting the generated magnetic field at the current-carrying wire pitches connections (See Figure 3.2).
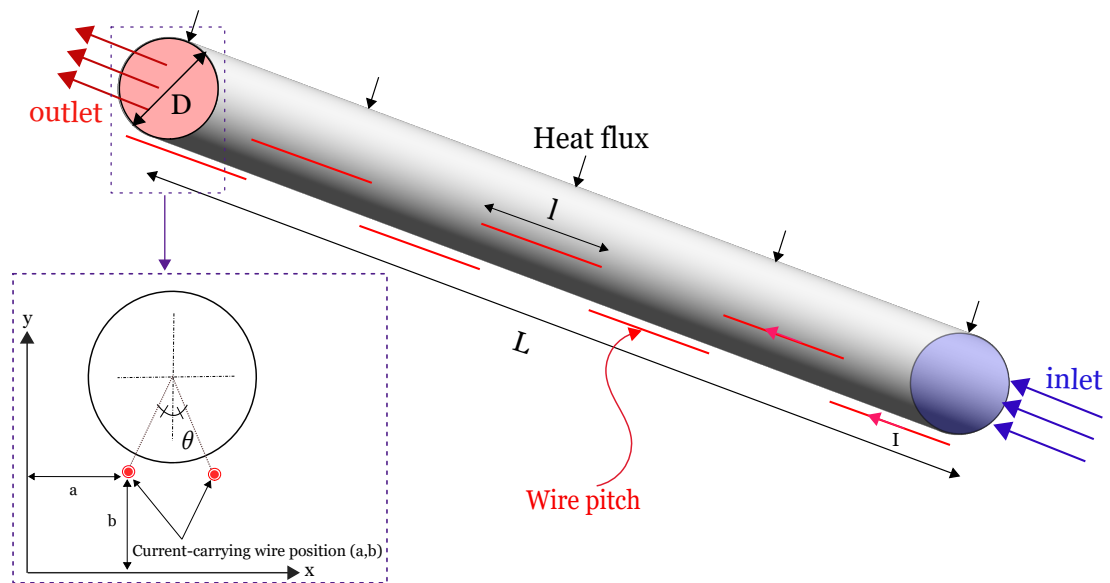
Figure 3.1: Schematic of the studied geometry.
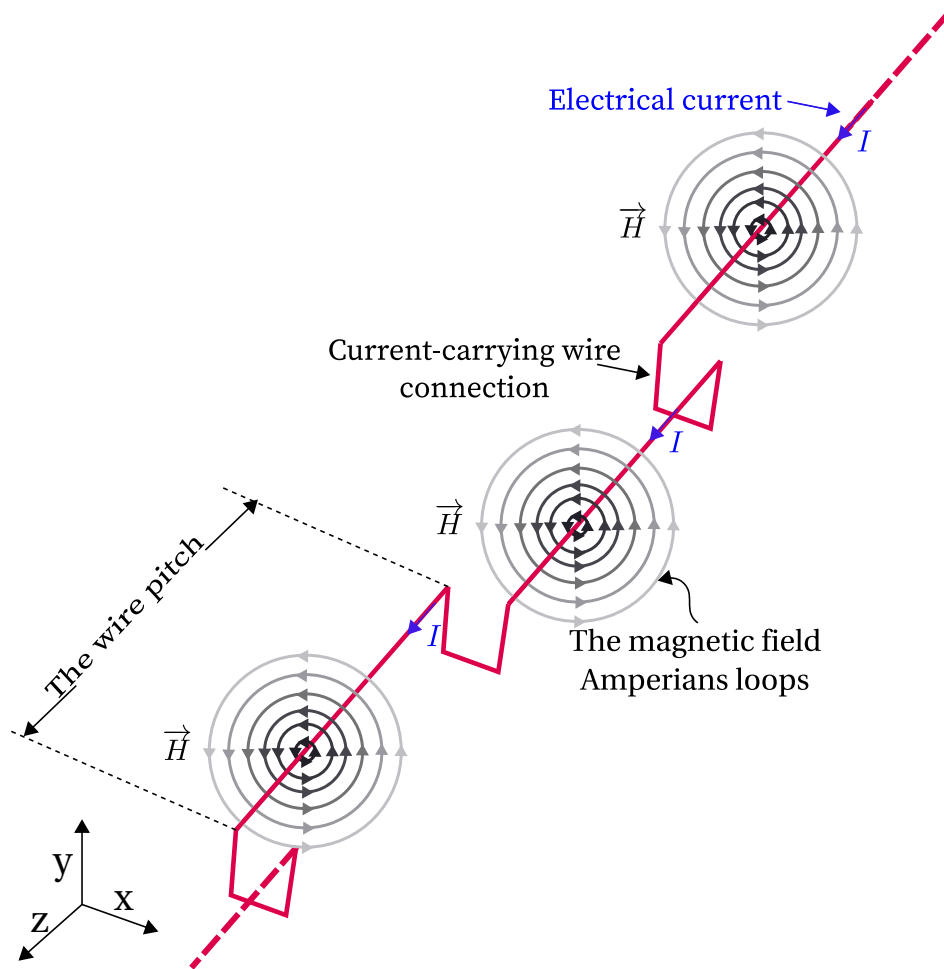
Figure 3.2: Schematic of the current carrying wire periodic configuration.

3.3   Thermo-physical proprieties

The used thermo-physical properties of the used nanoparticles and the base fluid, which are the magnetite and the water respectively, are presented in Table 3.2. On the other hand, the density, the specific heat, the dynamic viscosity and the thermal conductivity of the ferrofluid are calculated using the thermo-physical properties of the magnetite and the water from the Table 3.2, using the the correlations 2.38,2.40,2.41 and 2.42, represented in the second chapter, successively.

Table 3.2: Thermo-physical properties of water and the magnetite ([63]).

Property	The nanoparticle (Fe_3O_4)	The base fluid (water)
ρ (kg/m^3)	5200	1024
c_p (J/kg·K)	670	4001
k (W/m·K)	6	0.596
μ (kg/m·s)	-	0.00108

3.4   Numerical solution procedure

The commercial CFD code ANSYS Fluent [55] is used to solve the governing equations, where the simulations are done in parallel way using high performance computing hardware. Considering the following solver settings:

1. SIMPLEC algorithm is adopted for Pressure-Velocity coupling.

2. Least Squares Cell Based is selected for gradient interpolation.

3. PRESTO! scheme is selected for pressure.

4. Second order interpolation scheme is selected for Momentum and Energy.

Furthermore, the Kelvin body force mathematical model is hooked into the ANSYS Fluent momentum equations as source terms, where the x direction components are implemented in "X Momentum" section and the y direction components in "Y Momentum" section, via the user defined functions (UDFs).

To guarantee the high quality of obtained results and as a convergence criterion, the residuals for the continuity as well as the momentum equations are set 10^{-6}, but for the energy equation, the residuals are maintained 10^{-9}.

3.5   Boundary conditions

The applied boundary conditions in this study are resumed in the Table 3.3.

Table 3.3: The boundary conditions.

Inlet velocity	$V_{in} = V_{avg}$ where ($10^2 \leq Re \leq 10^3$)
Inlet temperature	$T_{in} = 300$ K
Heat flux at the tube wall	$q'' = 2000$ W/m^2
Outlet pressure	$P_{out} = 0$ Pa

3.6   Grid independency test

The structured mesh (O-grid) is selected for current study and in order to assure the mesh independency, three different meshes were proposed to perform the sensitivity study (see Table 3.4). To compare between the meshes, the dimensionless axial velocity was used as a comparison parameter. The three meshes were tested for ferrofluid laminar flow for $Re = 100$, in absence of the magnetic field.

Figure 3.3 shows the obtained results, a closer look at this figure shows that the results are identical for for the fine and the very fine meshes, but there is a difference of 0.1 % between these last and the coarse mesh. Therefore, the fine mesh (Mesh #2) was selected due to its accuracy and to save the computational time. The selected mesh is represented in Figure 3.4.

Table 3.4: The tested meshes parameters.

	Coarse mesh (Mesh #1)	**Fine mesh (Mesh #2)**	**Very fine mesh (Mesh #3)**
Number of elements	1080000	1948800	4377600
Near wall refinement	No	Yes	Yes
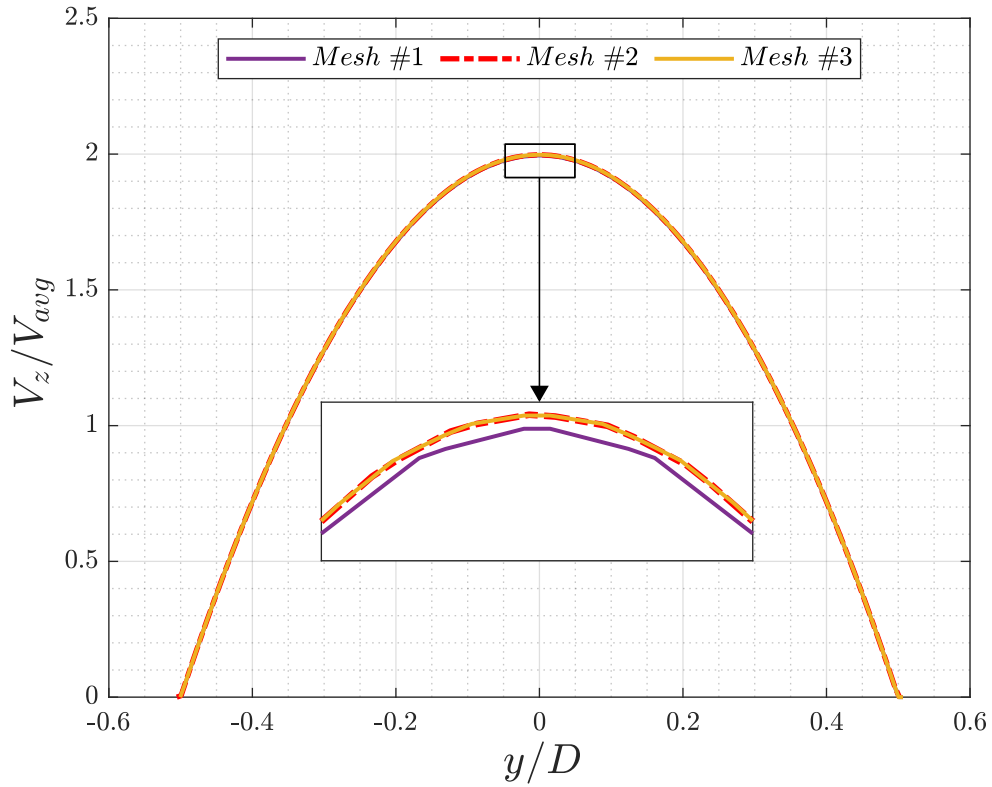
Figure 3.3: Dimensionless axial velocity for the three tested meshes at $z/D = 30.30$.
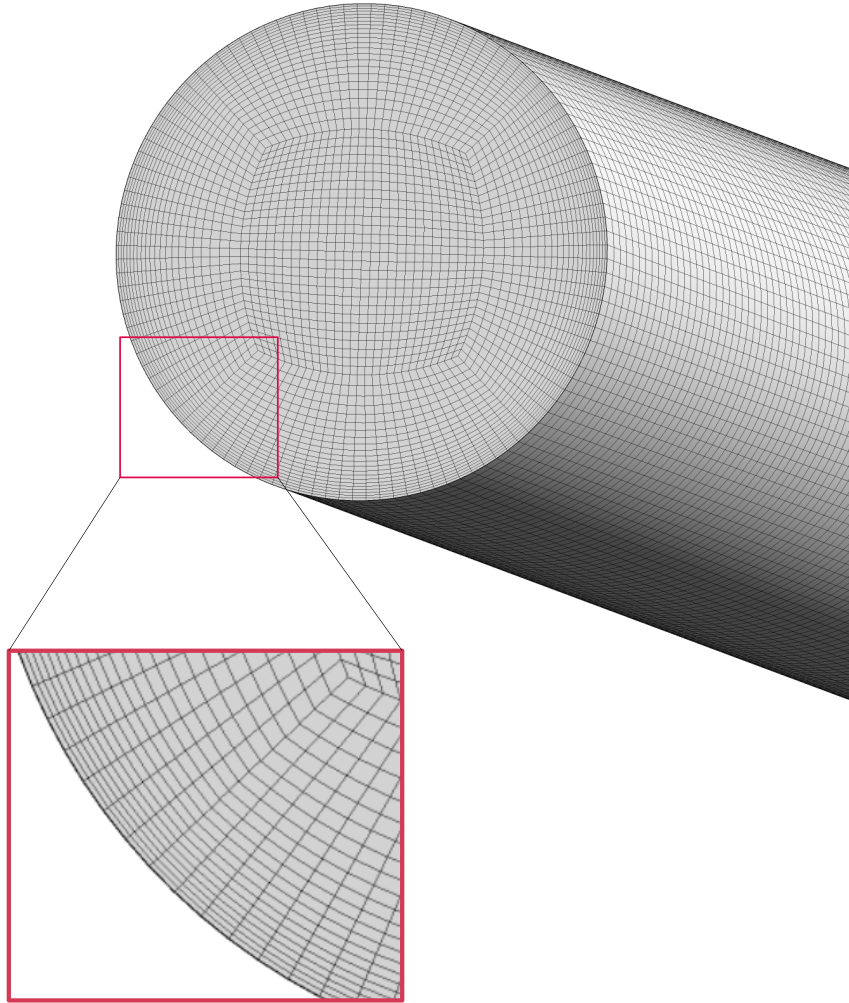
Figure 3.4: Three dimensional view of the selected mesh.

3.7 The validation

To ensure the accuracy of the obtained results it is important to validate the numerical results. Therefore, the studied smooth tube model has been used to simulate the water flow in laminar regime for two different cases, where in the first one lower Reynolds number $Re =100$ is used and in the second the high Reynolds number $Re=1000$. The simulations has been performed in absence of the magnetic field (the water properties are mentioned in Tables 3.2).

The obtained local Nusselt number for the water flow along the smooth tube is compared to Churchill-Ozoe correlation [64]:

$$\frac{Nu_D}{4.364\left[1+\left(\frac{Gz}{29.6}\right)^2\right]^{\frac{1}{6}}} = \left[1+\left(\frac{\left(\frac{Gz}{19.04}\right)}{\left[1+\left(\frac{Pr}{0.0207}\right)^{\frac{2}{3}}\right]^{\frac{1}{2}}\left[1+\left(\frac{Gz}{29.6}\right)^2\right]^{\frac{1}{3}}}\right)^{\frac{n}{2}}\right]^{\frac{1}{n}} \quad (3.1)$$

Where n=6 and Gz denotes the Graetz number which calculates the length of thermal entry and it is defined as:

$$Gz = RePr\left(\frac{D}{z}\right)$$ (3.2)

The plotted trends in Figure 3.5 shows a good agreement comparing the obtained numerical results with those calculated using Churchill-Ozoe correlation, where it can be seen clearly that the trends are in line for the low Reynolds number case ($Re = 100$), but for the high Reynolds number case ($Re=1000$), the deviation at the region located between the positions $z/D = 0$ and $z/D = 20$ is notably lower than 18.6 %.
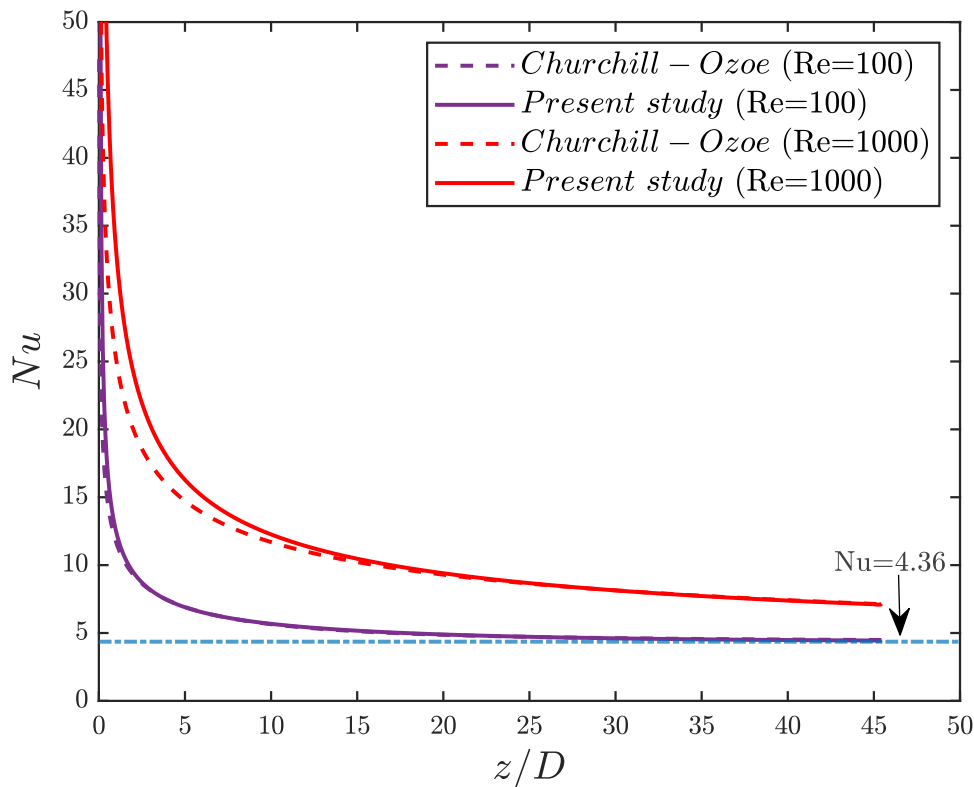
Figure 3.5: The local Nusselt number for present study compared to the results of [64] correlation.

3.8 Results and discussion

3.8.1 Flow pattern assessment

To evaluate the impact of the non-uniform magnetic field generated by the current carrying wire periodic configuration on the ferrofluid flow in smooth tube, the axial velocity along the tube centerline is measured, for four different cases characterized by the magnetic numbers, $Mn = 0, Mn = 2.83 \times 10^4$, $Mn = 6.37 \times 10^4$ and $Mn = 1.13 \times 10^5$, where all the simulations are done at Reynolds number $Re = 100$.

The results represented in Figure 3.6 shows that when no magnetic field is applied ($Mn = 0$), the flow develops from $V_z = V_{avg}$ (the applied inlet velocity) until it becomes the double i.e. $V_z = 2 \cdot V_{avg}$ which corresponds to the theoretical solution of a fully-developed laminar flow, following Hagen–Poiseuille law. The theoretical equivalence of the developing length for $Re = 100$ is about $5 \cdot D$, which is near to the value where the axial velocity becomes steady.

On the other hand, when an external non-uniform magnetic field is applied on the flow, the velocity shows a periodic behaviour over the reference curve of the case when no external magnetic field is applied. It is noteworthy mentioning that the periodicity of the velocity is in accordance with the current-currying wire pitch length, $l = 3 \cdot D$.

A closer look at one of the pitches in Figure 3.6 shows that the axial velocity in the tube centerline tends to reach a lower and steady value, but the position change of the current-carrying wire pitch leads to a noticeable sharp increase in the axial velocity. In addition, it is noticed that this pattern keeps repeating along the tube for every wire pitch.

What is remarkable also, is that the axial velocity profiles fluctuations are proportional with the magnetic field intensity, where the fluctuations are higher at higher magnetic field intensity.
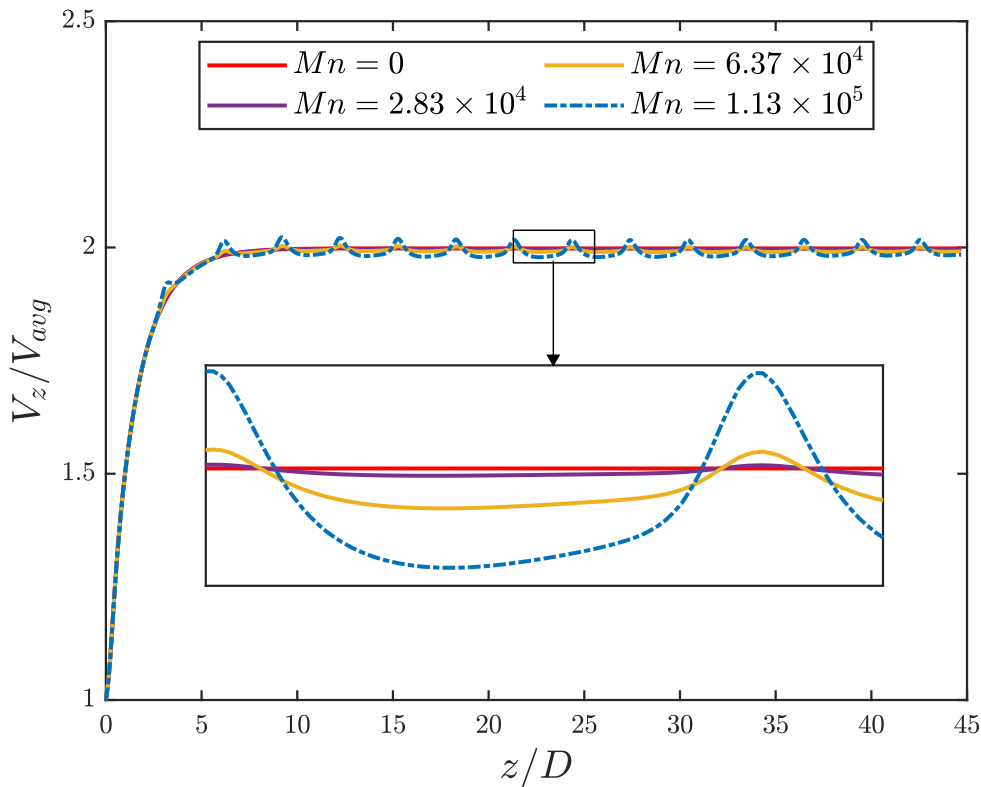
Figure 3.6: Dimensionless axial velocity profile at tube center-line for different Magnetic numbers at Re=100.

For a deep understanding of the local axial velocity comportment, the axial velocity contours at three different axial locations, $z = 37.1 \cdot D$, $41.1 \cdot D$ and $43.2 \cdot D$ are shown in Figure

3.7.

For the case when no magnetic field is applied, the axial velocity contours do not present any modifications and this is due to the fact that the flow is already hydrodynamically developed.

In contrast, for the case where a non-uniform magnetic field is applied by the periodic wire configuration, it can be seen that the fluid is directed towards the magnetic field source (the current-carrying wire position) attracted by the Kelvin body force $\overrightarrow{F_k}$. A considerable deformation is noticed for the high axial velocity region towards the current-carrying wire position, accompanied at the same time with a decrease of the axial velocity near to the tube centerline region.

What is worth noting is that when the current-carrying wire changes its location, from a pitch to other pitch, the flow has to redevelop over and over to be adapted to the new attracting magnetic force generated by the new wire pitch.
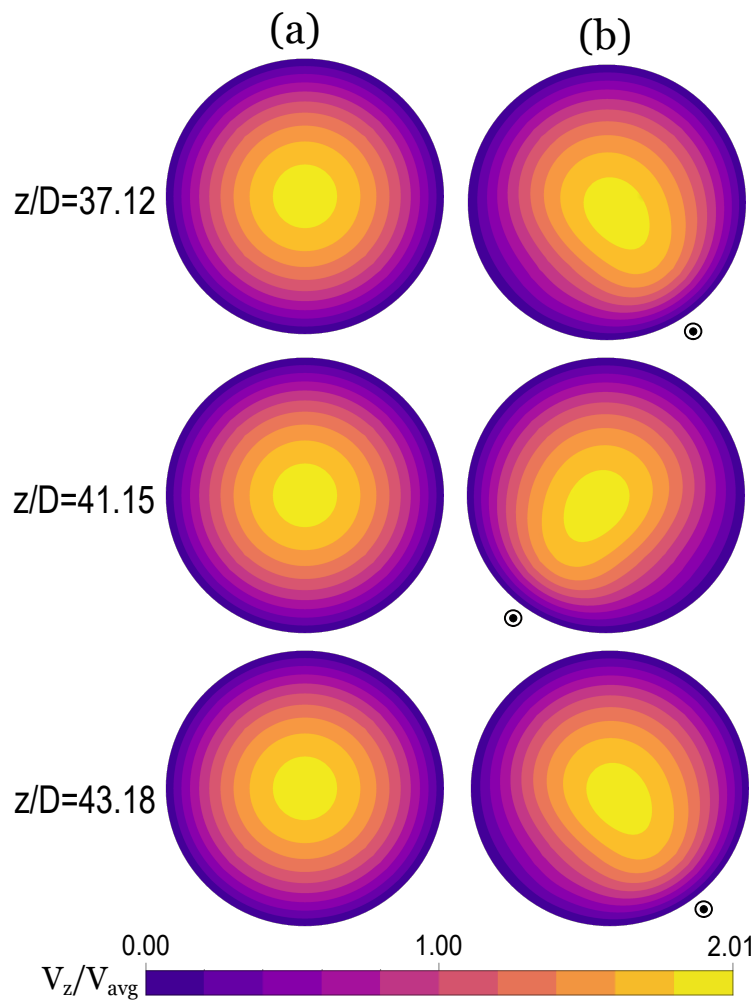
Figure 3.7: Velocity contours at Re=100, (a) $Mn = 0$ (b) $Mn = 1.13 \cdot 10^5$.

3.8.2 Thermo-hydraulic assessment

To quantify the effect of the applied non-uniform magnetic field on the convective heat transfer, a three different laminar flow simulations for a three different Reynolds numbers, Re =100, Re =500 and Re =1000 are simulated for four different magnetic numbers, varying from Mn=0 to Mn = $1.13 \cdot 10^5$. The obtained results from these simulations, are plotted in terms of average Nusselt number in function of the magnetic number and Reynolds number (see Figure 3.8a). Besides, the increment of the average Nusselt number in comparison to the reference case when no magnetic field is applied, is revealed in Figure 3.8b.

It is apparent from Figure 3.8a that the effect of the applied magnetic field is not considerable for the two highest Reynolds numbers $Re = 500$ and $Re = 1000$, while is observable that there is a significant enhancement of about 8 %, for the lowest Reynolds number, $Re = 100$. This can be explained physically with the the fact that the increase in Reynolds number, increases the inertial forces of the ferrofluid flow until it overcomes the magnetic forces, consequently the effect on the ferrofluid flow becomes negligible.

Another important parameter to evaluate the effect of the applied magnetic field on the needed pumping power for the ferrofluid flow, the friction factor is extracted from simulations and plotted in Figure 3.9. Obviously, there is a strong relation between the pressure drop and the heat transfer, in such way that any augmentation in the Nusselt number implies an augmentation in the friction factor of the flow.

However, it can be concluded from Figure 3.9 that the friction factor increment is much lower in comparison with the Nusselt number augmentation, which means that a slightly higher pumping power is needed to enhance significantly the convective heat transfer, using an external magnetic field.
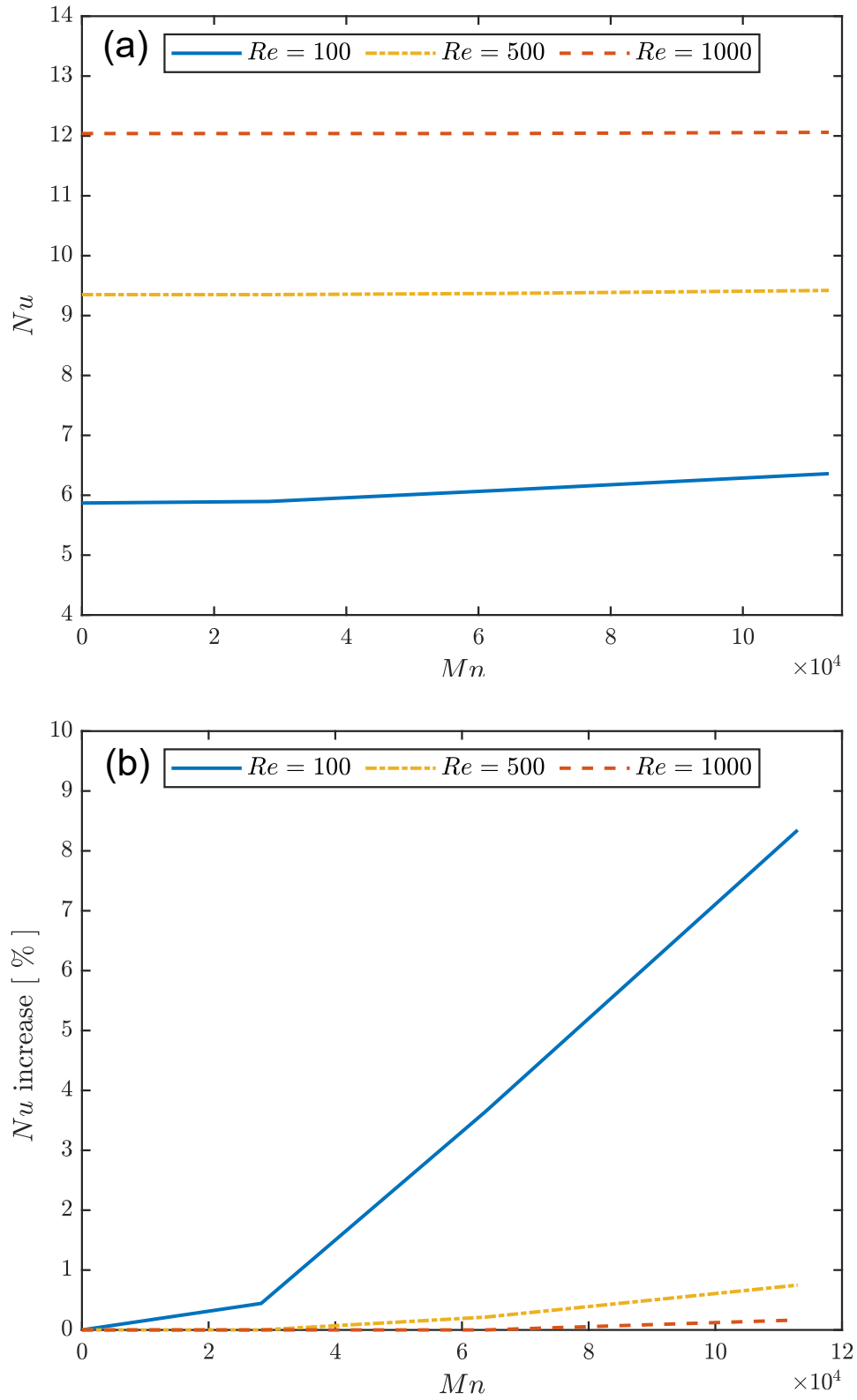
Figure 3.8: Effect of magnetic field increment on the average Nusselt number for different Reynolds numbers.
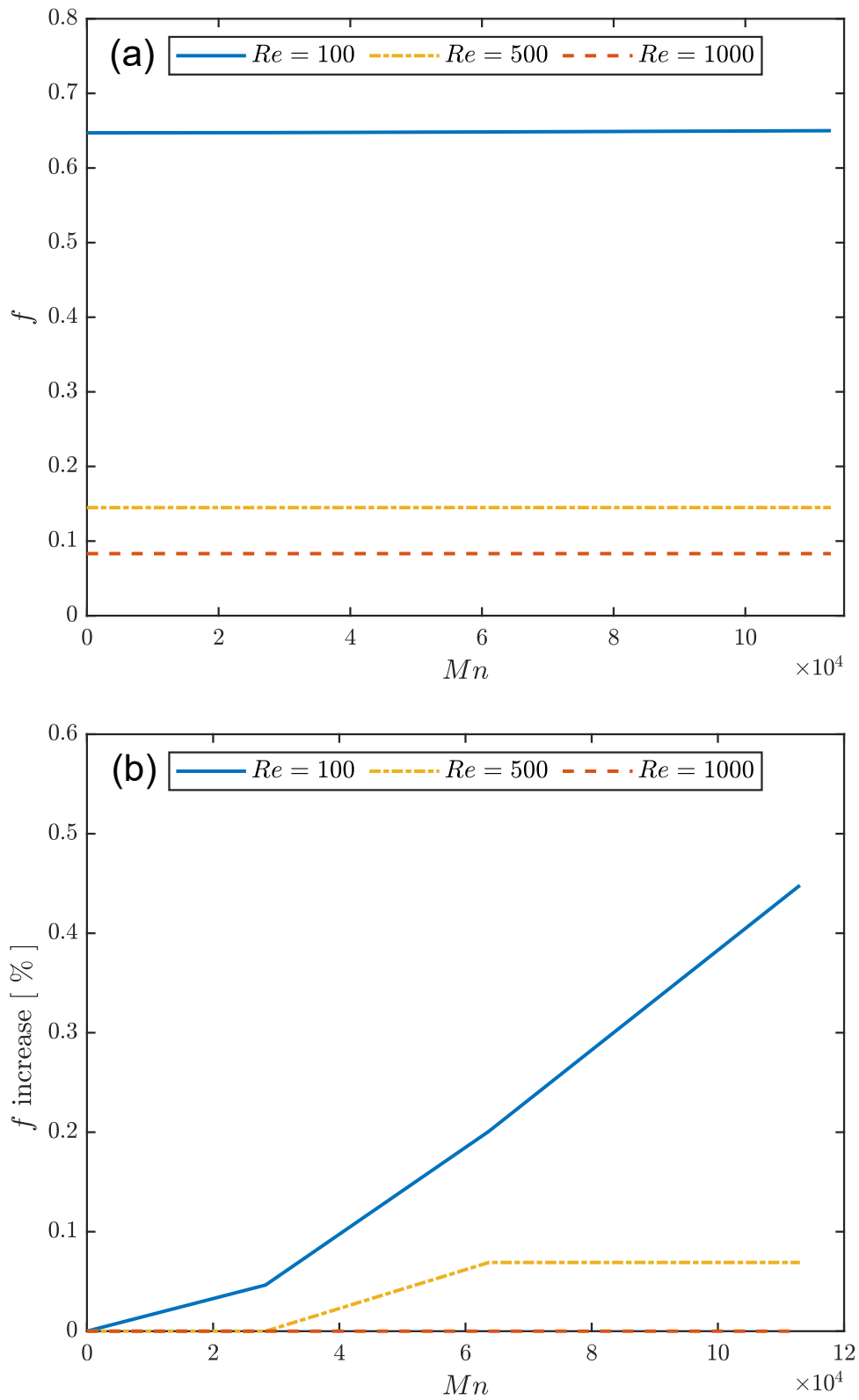
Figure 3.9: Effect of magnetic field increment on the average friction factor for different Reynolds numbers..

To estimate the performance of applying the non-uniform magnetic field with the proposed wire configuration on the ferrofluid flow, the well known Performance Evaluation Criterion (PEC) is calculated to measure the heat transfer enhancement taking into account the increase in the friction factor.

Figure 3.10 shows trends of PEC in function of the magnetic number and Reynolds number. A closer look to the curves gives the impression that the PEC behaves in like manner with the Nusselt number increment showed in Figure 3.8, because of the low increase in the friction factor for all the tested cases.

The periodic configuration of the current-carrying wire introduces an important enhancement, which is higher than a 8%, for the lowest Reynolds number tested case ($Re = 100$) and for Magnetic numbers grater than 10^5. It should be mentioned that the tested tube length, $L = 45 \cdot D$, implies that the flow is thermally developing along all the tube for relatively low Reynolds numbers, Re 130; while the periodic wire configuration improves the convective heat transfer in the developed region. Therefore, a higher enhancement would be expected for the tubes with long length.
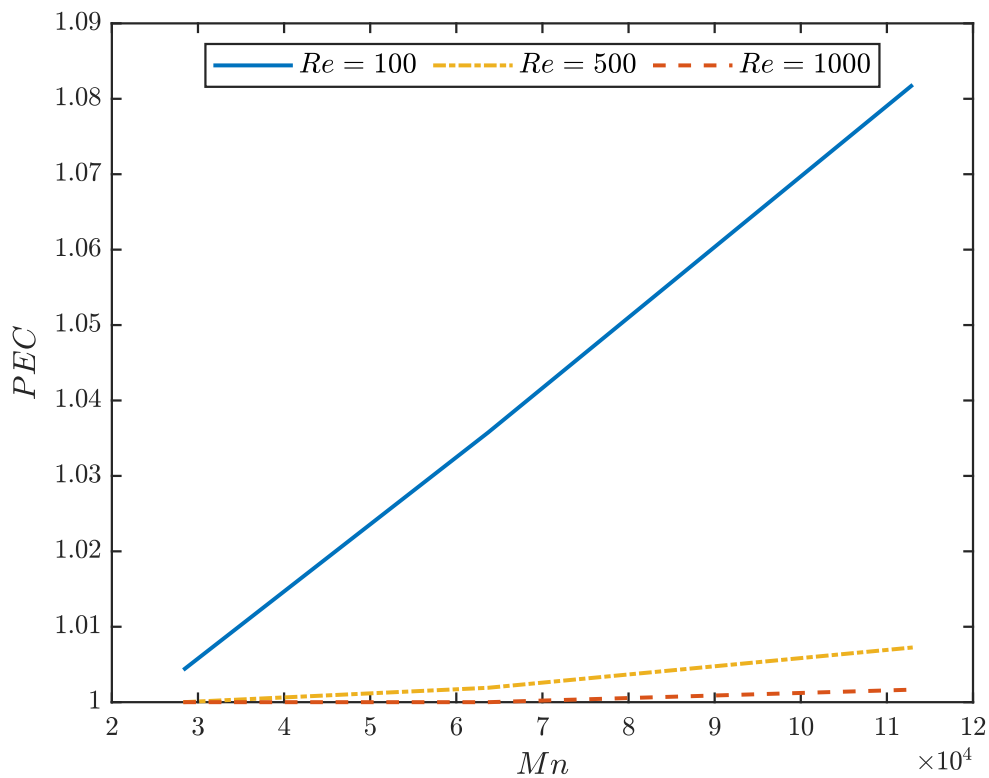
Figure 3.10: Performance Evaluation Criterion (PEC) in function of the magnetic number (Mn).

3.9   Conclusions

This chapter evaluated numerically the feasibility of applying a non-uniform magnetic field generated by a periodic current carrying wire, on a laminar flow of ferrofluid in smooth tube under a uniform heat flux. The main findings from this study are resumed in the following points:

1. The magnetic field generated by the periodic current-carrying wire has a negligible effect on the axial velocity comportment along the hydrodynamically developing zone, while it creates a significant periodic fluctuation on the flow pattern once the flow reaches the its fully developed region.

2. Imposing a non-uniform magnetic field on the ferrofluid laminar flow enhances the heat transfer which is noticeable in the increase of the Nusselt number.

3. The higher increase in the Nusselt number is observed for $Re = 100$ case which is about 8 % in comparison to the reference case (no magnetic field is applied).

4. There is no considerable increase in the friction factor, lower than 0.5 %, for all the tested cases.

5. The use of the magnetic field generated by a periodic wire configuration is recommended for the laminar flows in tubes where an important portion of the tube length is under fully developed flow conditions, in other words, for the low Reynolds numbers or the long tubes.

4 Magnetic field effect on turbulent flow (Application on PTSC absorber)

4.1 Introduction

Among the concentrated solar power (CSP) technologies, the parabolic trough solar collectors occupied a key place in the CSP's projects over the world [65], [66], exhibiting a promising rol as an alternative to the conventional power generation plants.

A parabolic trough solar collector (PTSC) mainly consists of a reflector with trough shape which receives the direct solar irradiance and reflects this last on a coated absorber tube, contained in an evacuated glass tube. The absorber tube contains the heat transfer fluid (HTF)[67], which depends on the application of the PTSC [68] (see Figure 4.1). Compared to other clean energy harvest systems, the PTSC technology encounters many engineering challenges to be competitive as a power generation tool, due to that, many studies have been carried out in order to improve the performance of this technology, for example, by modifying the optical performance of the PTSC [68], [69].

Many efforts are focused on enhancing the tube side heat transfer rate in the absorber tube. However, the used techniques can be classified following to the classical distinction between the passive methods, like manipulating the geometrical characteristics of the device, and active methods, which require an additional energy supply [13]. Both types of techniques have been used by different research groups to enhance the performance in PTSCs.

The present chapter set out to investigate numerically the effect of the periodic current-carrying wire configuration on the thermal-hydraulic performance of PTSC absorber that works in the turbulent flow regime. A wide range of Reynolds numbers that varies from $Re = 15 \cdot 10^3$ to $Re = 250 \cdot 10^3$, and Magnetic numbers, $1.52 \cdot 10^7 < Mn < 1.84 \cdot 10^9$, is analyzed to asses the effect of the proposed periodic configuration on the heat transfer rate and pressure drop in the PTSC absorber.

4.2 Problem description

In Figure 4.2 is shown a three dimensional model of the studied parabolic trough solar collector (PTSC) absorber tube with different view angles. The absorber tube equipped with a current-carrying wire, whose position varies periodically. Where, the lower parts of the current-carrying wire are supposed to be attached to the glass tube keeping the wire fixed, while the two ends of the wire are connected to electricity source to generate the magnetic field.
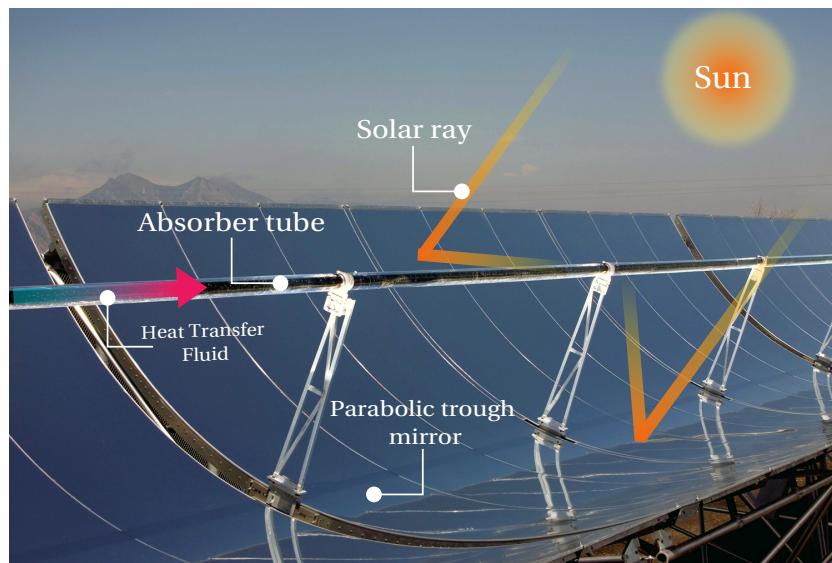
Figure 4.1: The consisting elements of the parabolic trough solar collector and its working principle [70].
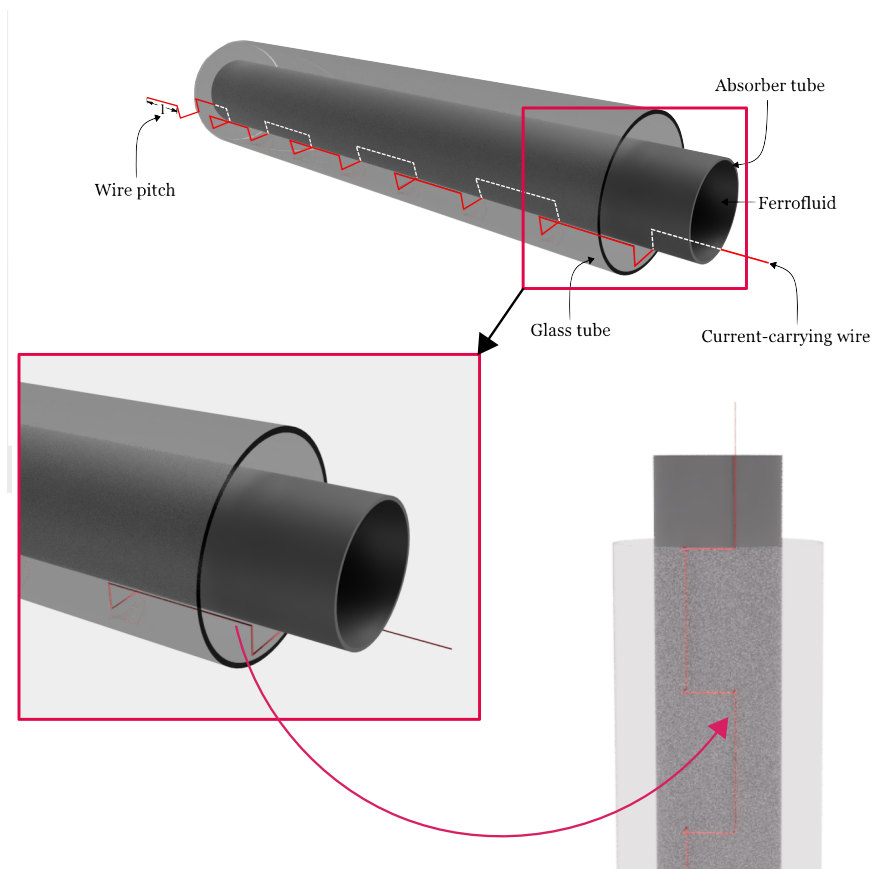
Figure 4.2: 3D model for PTSC absorber tube equipped with periodic current-carrying wire.

Figure 4.3 illustrates the simplified model of the parabolic trough solar collector absorber tube, in which the straight current-carrying wire model is shown in Figures 4.3 a-b and the periodic wire model is shown in Figures 4.3 c-d. The tube is determined by its inner and outer diameters, D and D_e, successively, and a total length L. The ratio between the two diameters is D_e/D=1.06.

The current-carrying wire periodic configuration is characterized by its pitch length (l), the distance between the wire and the tube inner wall (R), and the position angle θ, which measures the angle created by the y axis and the line passes through the wire and tube centers (Figures 4.3 c-d).
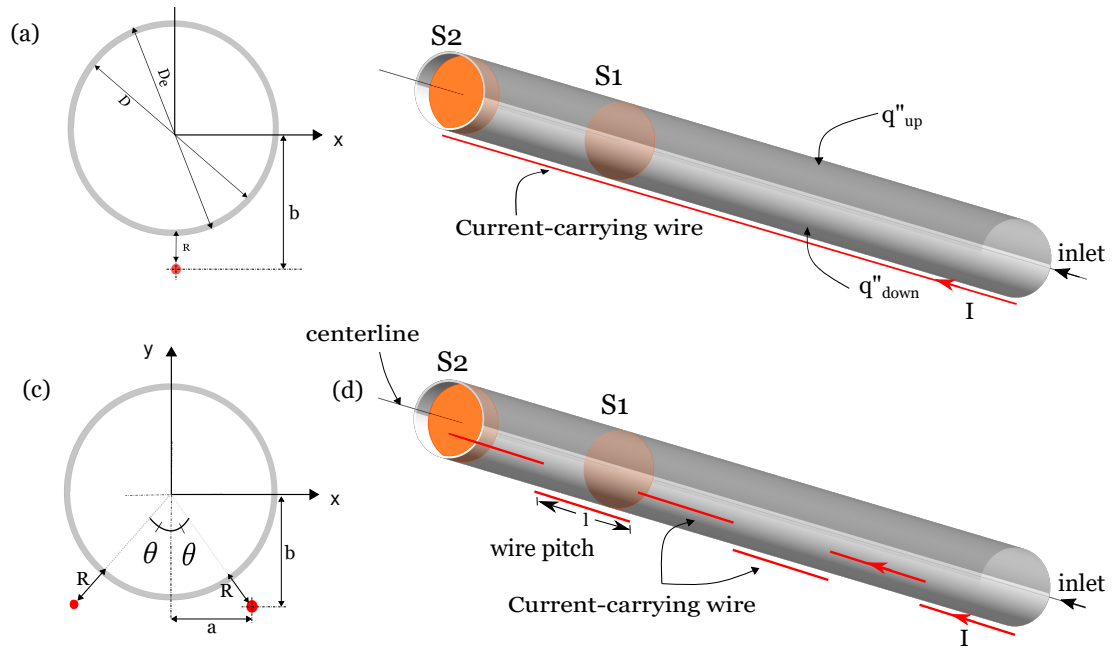
Figure 4.3: Schematic model for the studied cases, a) cross-sectional and b) 3D view of the straight wire case, c) cross-sectional and d) 3D view of the periodic wire case.

However, the used heat transfer fluid (HTF) for the present work, is the ferrofluid which is composed of a spherical magnetite nanoparticles (Fe_3O_4) with the particle diameter d_p=10 nm and a volume fraction φ=4% and Therminol 66 as a base fluid,. The ferrofluid enters from the tube inlet with uniform velocity equals to V_{avg}, and uniform temperature T_{in}.

In addition, the applied heat flux on the absorber tube is assumed to be non-uniform due to the parabolic trough solar collector shape. Hence, the heat flux is applied at the outer wall of tube, taking in consideration the simplified local concentration ratio (LCR) model [45], [71], where this model assumes that the tube receives a uniform heat flux on its upper half, equals to the global radiation I_g (Equation 4.1), while the lower half is exposed to a uniform heat flux $q"_{down}$, equals to the concentrated radiation beams reflected by the PTSC (Equation 4.2). For the current study: $I_g = 680\ W/m^2$, $I_b = 630\ W/m^2$, and the concentration ratio is considered $C_R = 15.46$.

$$q"_{up} = I_g \tag{4.1}$$

$$q"_{down} = I_b C_R \tag{4.2}$$

4.3 Thermo-physical properties

The density, specific heat, dynamic viscosity and thermal conductivity of the Therminol 66, the magnetite nanoparticles and the ferrofluid are shown in Table 4.1:

Table 4.1: The thermo-physical properties of base fluid, nanoparticles and the ferrofluid [45].

Property	The nanoparticle (Fe_3O_4)	The base fluid (Therminol 66)
ρ (kg/m^3)	5200	899.5
c_p (J/kg·K)	670	2122
k (W/m·K)	6	0.107
μ (kg/m·s)	-	0.00106

4.4 Numerical approach

The present problem is solved using Finite volume method by means of the commercial CFD code ANSYS$^{\circledR}$ Fluent release 17.1 [55] in parallel mode, taking into account the following settings:

1. The $k - \epsilon$ RNG model is selected for turbulence modeling (based on previous literature [44], [71]).

2. SIMPLEC algorithm is adopted for Pressure-Velocity coupling.

3. Least Squares Cell Based for gradient interpolation.

4. PRESTO! scheme for pressure.

5. Second order interpolation scheme is selected for Momentum and Energy.

On the other hand, the Kelvin body force components are added as source terms to the momentum equations in x and y directions by implementing a user defined function (UDF).

To ensure a good quality for the obtained results, a value for the residuals lower than 10^{-5} for the continuity and momentum equations and 10^{-9} for the energy equation is considered as convergence criterion.

4.5 The boundary conditions

The applied boundary conditions for this simulation are presented below in Table 4.2.

Table 4.2: The boundary conditions.

Inlet velocity	Vavg, $where\ 15000 \leqslant Re \leqslant 250000$
Inlet temperature	230°
Heat flux (tube upper wall)	q''_{up}
Heat flux (tube lower wall)	q''_{down}
Outlet pressure	0 Pa

4.6   Grid generation

O-grid structured mesh is generated along the absorber tube where the mesh is refined near to fluid-wall contact region in order to cover the high thermal, hydraulic and magnetic gradients. Furthermore, to ensure that the selected mesh provides accurate results and requires a reasonable computational time the friction factor was chosen as a relevant quantity to compare the accuracy of the different mesh sizes. Three different meshes, ranging from 1.87 to 5.69 million elements, were tested for Therminol 66 turbulent flow for two Reynolds numbers, $Re = 15000$ and $Re = 250000$, covering the range tested in the present work. The results are summarized in Table 4.3, where the deviation of the calculated friction factor is compared (in percentage) to that provided by the finest mesh.

Table 4.3: Friction factor comparison.

Number of elements	$Re = 15 \cdot 10^3$	$Re = 250 \cdot 10^3$
$1.87 \cdot 10^6$	0.2%	7.8%
$3.71 \cdot 10^6$	0.03%	0.10%
$5.69 \cdot 10^6$	($f = 0.0299$)	($f = 0.0147$)

As can be noticed, the coarsest mesh provides good results at the lowest Reynolds number, but the deviation becomes unacceptable at the highest Reynolds number, around 8%. On the other hand, the intermediate mesh shows a very low deviation even at the highest Reynolds number, 0.1%, value that has been considered as accurate enough. The selected mesh is shown in Fig. 4.4.
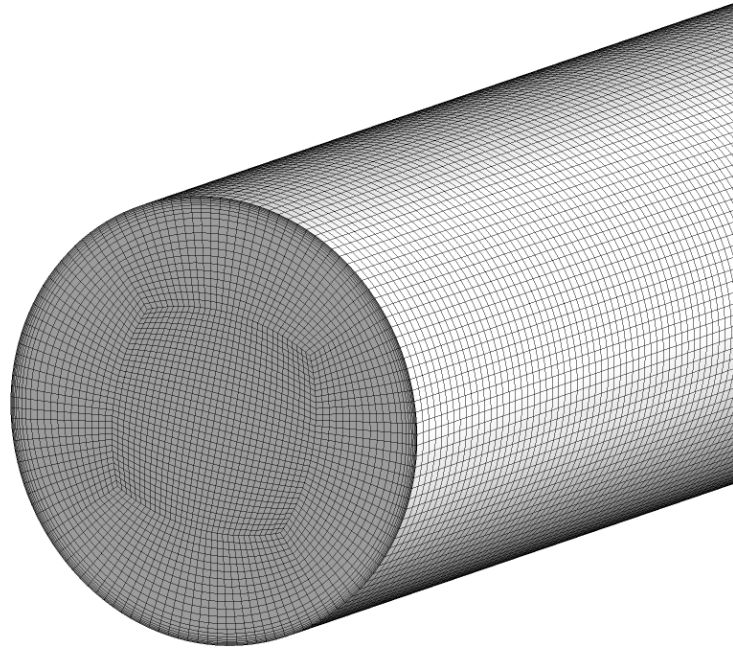
Figure 4.4: The selected mesh type.

4.7   Validation of the numerical model

The numerical methodology has been validated by comparison of the variables of interest against the well-known correlations in the tested range. Blasius's equation [72], Petukhov's correlation [73] and Gnielinski [74] have been considered for the friction factor and the Nusselt number, respectively.

$$f = 0.3164Re^{-0.25} \tag{4.3}$$

$$f = (0.79LnRe - 1.64)^{-2} \tag{4.4}$$

$$Nu = \frac{\left(\frac{f_{th}}{8}\right).Re.Pr}{1 + 12.8 \times \left(\frac{f_{th}}{8}\right)^{\frac{1}{2}} (Pr^{\frac{2}{3}} - 1)} \tag{4.5}$$

Darcy's friction factor is plotted in Figure 4.5 as a function of the Reynolds number, in the absence of magnetic field. As expected, the simulations with pure Therminol 66 and Therminol 66 with nanoparticles clearly overlap. The maximum deviation of the simulations is about 5%, which can be considered as accurate enough for validation purposes.

In Figure 4.6, the average Nusselt number is plotted as a function of the Reynolds number

and compared with the correlation for fully turbulent flow proposed by Gnielinski [74]. The results show a good agreement with the correlation, with a deviation lower than a 18% for the whole range.
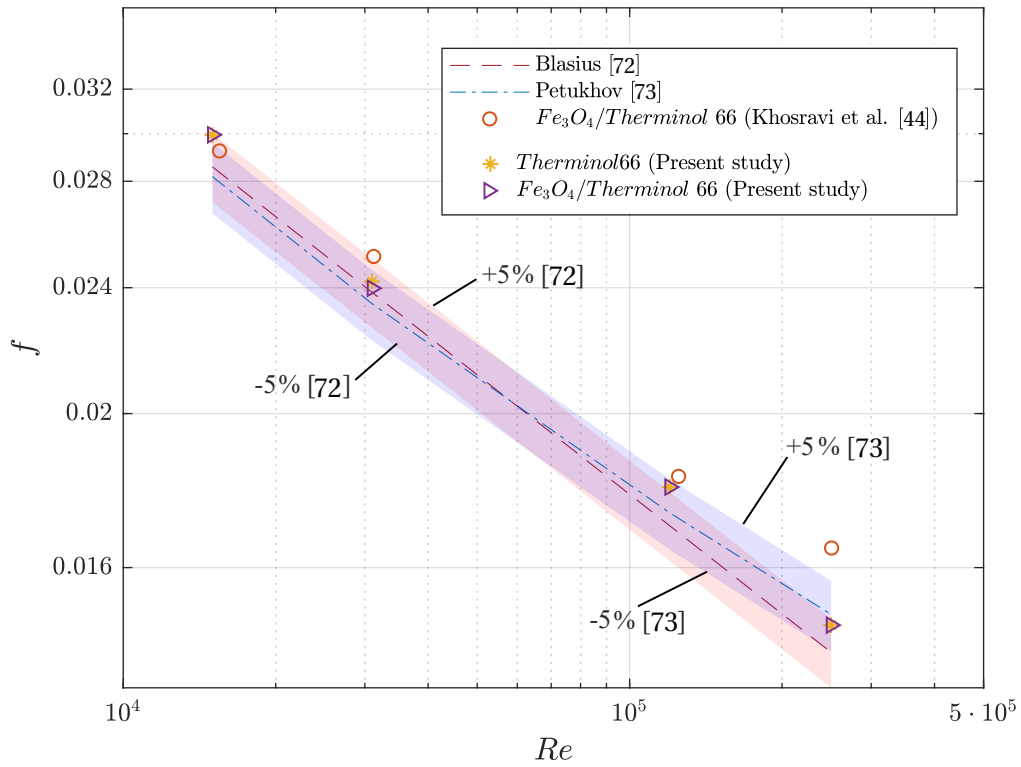
Figure 4.5: Friction factor comparison between the obtained results with previous studies.
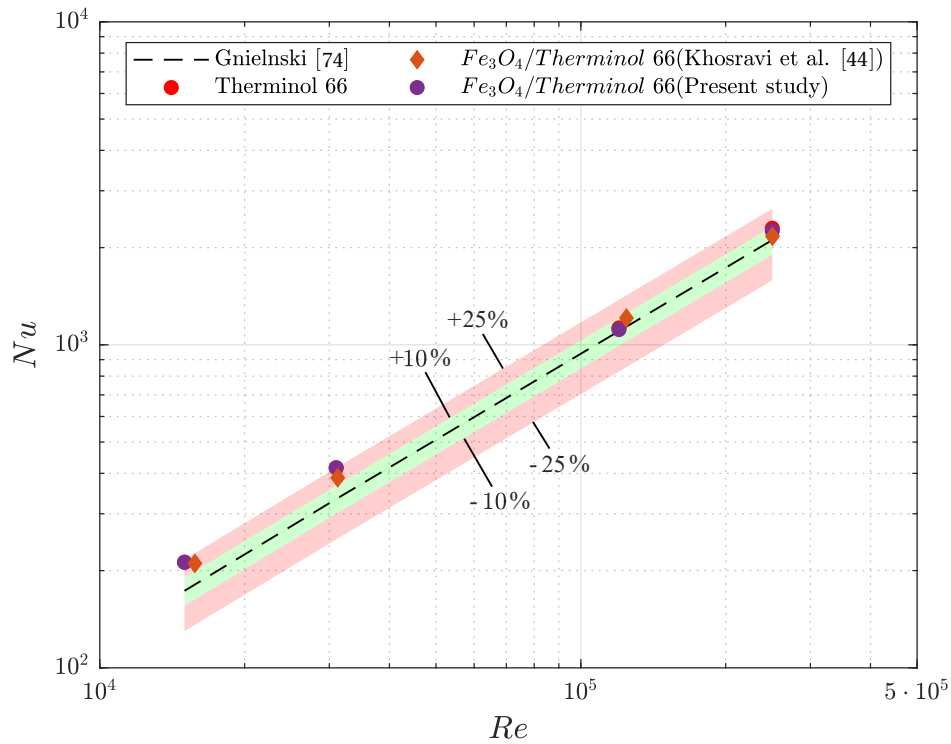
Figure 4.6: Comparison of the average Nusselt number values with Gnielinski's correlation [74].

4.8 Results and discussion

4.8.1 Effect of the magnetic number

The effect of the magnetic field intensity on the average Nusselt number is analyzed in Figure 4.7, at a Reynolds number $Re = 15000$, for the both wire configurations, the straight and the periodic. On the right axis, the increase in the Nusselt number in comparison with the reference case (without magnetic field applied, $Mn = 0$) is also indicated.

According to the results, increasing the Magnetic number value from $Mn=1.52 \times 10^7$ to $Mn=1.84 \times 10^9$ leads to an augmentation on the average Nusselt number for both configurations. However, the increment for the straight wire configuration is more subtle if it is compared with the periodic configuration, with an increase of about 5% and 25%, respectively.

The effect of the increase of the Magnetic number, from $Mn=1.52 \cdot 10^7$ to $Mn=1.84 \cdot 10^9$, on the friction factor is illustrated in Figure 4.8. The right axis represents the friction factor increase, as a percentage, comparing to the reference value when no magnetic field is applied ($Mn = 0$). For both wire configurations with $Mn=1.52 \times 10^7$, there is no significant increase in the friction factor, around a 2%, but an increase in the Magnetic number increases the friction factor around 7% for the straight wire case, in contrast to the periodic wire, which shows an increment of around 9%. Thus, it must be highlighted the close relation between the heat transfer and the pressure drop results, a Nusselt number increase implies an increase in the friction factor.
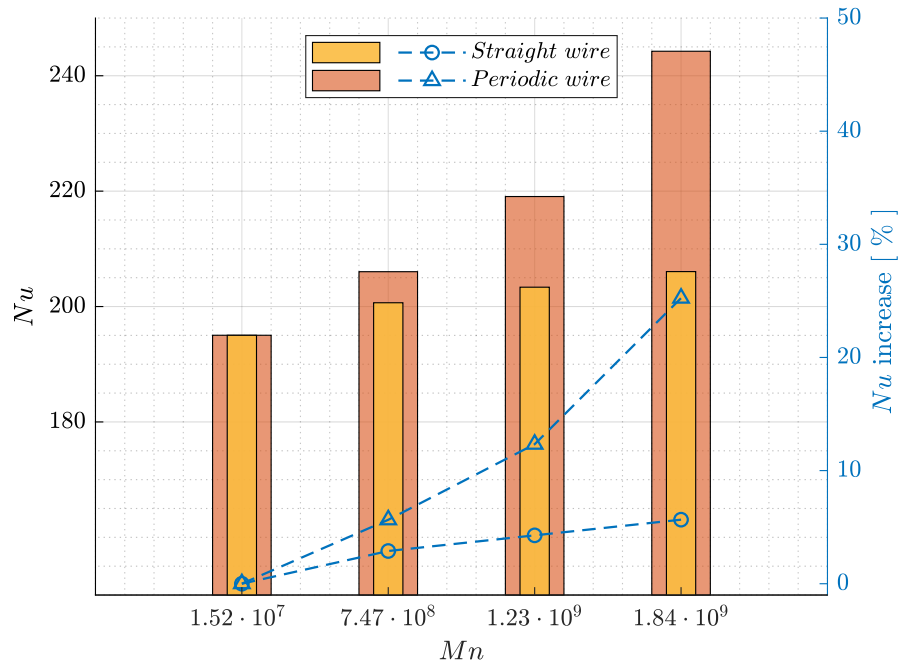
Figure 4.7: Effect of different wire configurations and the Magnetic number on the Nusselt number at *Re*=15000.
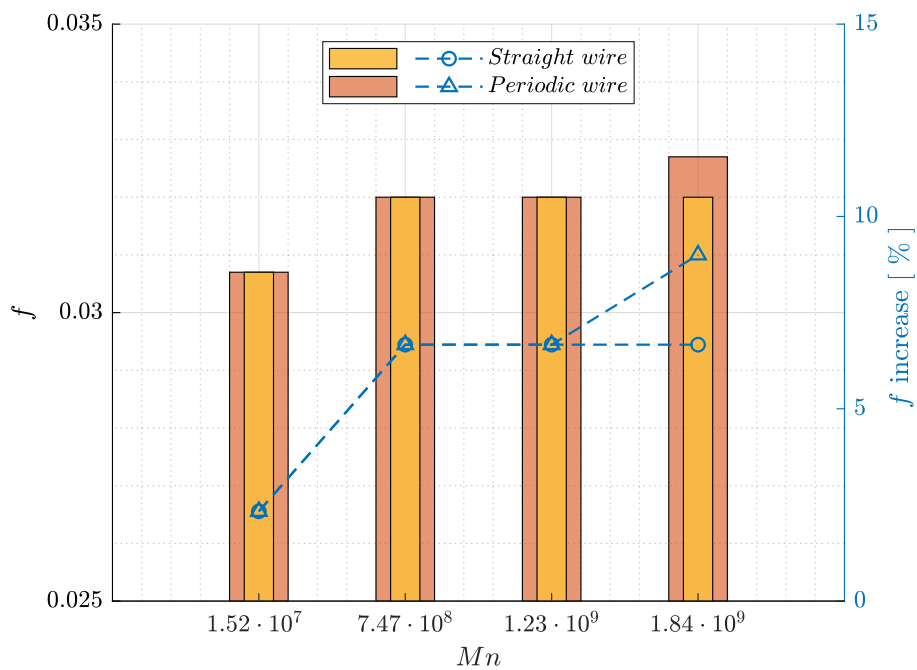
Figure 4.8: Effect of Magnetic number for different current-carrying wire configurations on friction factor at *Re*=15000.

4.8.2 Effect of current-carrying wire configuration

The three dimension dimensionless axial velocity profiles of Fe_3O_4/Therminol 66 ferrofluid flow are plotted and depicted in Figures 4.9(a-c) at the axial position $z = 22.7 \cdot D$ and Re=15000.

Figure 4.9a shows an axisymmetric profile for the case where no external magnetic forces are applied, meanwhile Figure 4.9(b,c) show the deformation of the axial velocity profiles in presence of the Kelvin body force due to the applied magnetic field, like it was noticed in previous works [75], [76]. In the case of the straight current-carrying wire depicted in Figure 4.9b, it is noticeable a high velocity region near the current-carrying wire. On the other hand, the periodic wire configuration case (Figure 4.9c) shows an asymmetric pattern with two velocity peaks. The current wire at the current wire position generates a peak (similarly to the straight wire), while the other weaker peak can be justified by the flow inertia, i.e., the flow is still evolving from the precedent wire pitch, where the wire was placed at the opposite position.
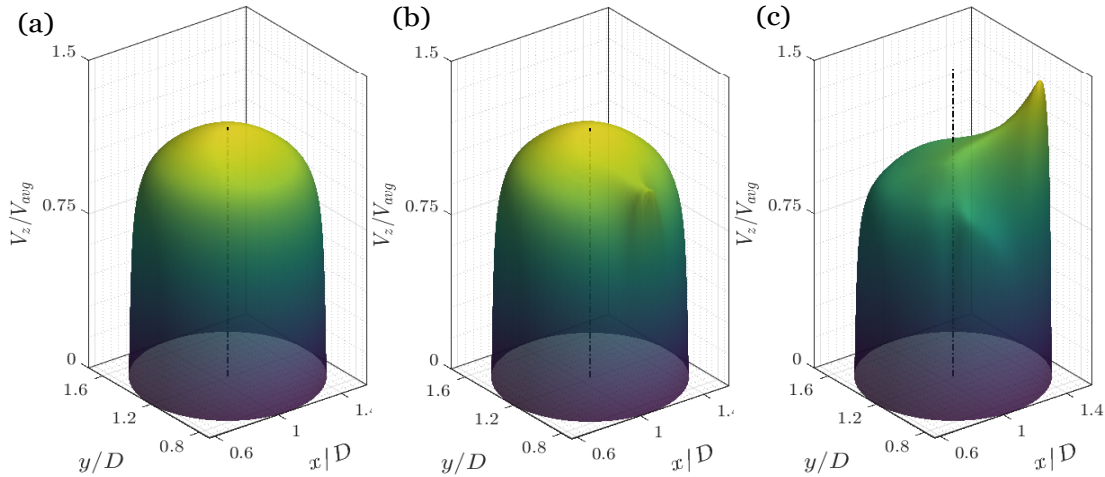
Figure 4.9: Dimensionless axial velocity 3D profiles of ferrofluid flow at the axial position z=22.7, for Re 15000 (a) Mn=0, (b) Straight current-carrying wire case, Mn=1.84·10^9 (c) periodic current-carrying wire case, Mn=1.84·10^9 , pitch length: $l/D = 3$ and $\theta = 30°$.

Furthermore, Figure 4.10 reveals the longitudinal comportment of the axial velocity at the tube centerline along the z direction for different wire configurations. Clearly, the axial velocity (which enters the tube with a uniform profile) develops until it reaches a maximum constant value at the fully developed region. The straight wire shows a similar behaviour to the case with $Mn = 0$, the flow develops and the tube center is far from the current-carrying wire, so little effect is found on the axial velocity. On the contrary, the periodic wire configuration case shows a spatially-periodic pattern, there is an initial developing region but after 4 to 5 pitches the flow reaches periodicity. This can be explained by the periodicity of the external magnetic field which is perceived by the flow. In addition, it is a noticeable that the length of the repeated pattern matches the simulated pitch length, $l = 6 \cdot D$.
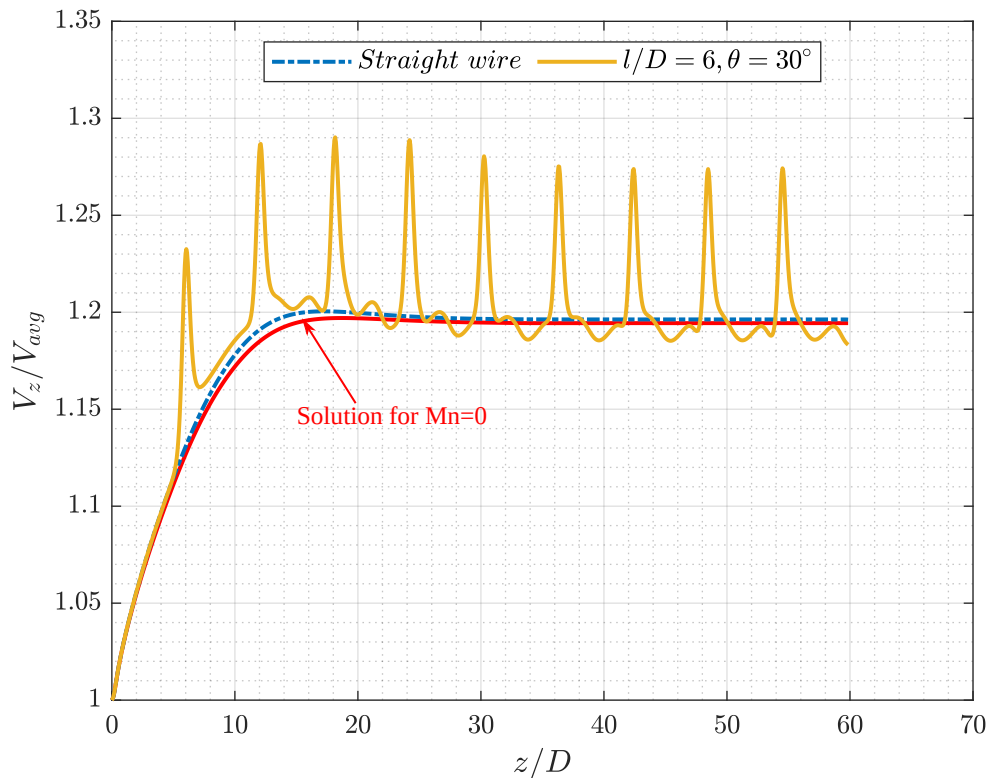
Figure 4.10: Dimensionless axial velocity at the tube center along the z direction for both wire configurations, Re=15000 and Mn=1.84·10^9.

The dimensionless axial velocity contours in Figure 4.11 reveal the distribution of the velocity at Re=15000 in three different cross sections located at z=16.7D, z=19.7·D and z=22.7·D for a Magnetic number Mn=0 (Figure 4.11a), Mn=1.84·10^9 generated by the straight current-carrying wire (Figure 4.11b) and the periodic wire (case of pitch length l=3·D, and position angle θ = 30°) (Figure 4.11c). For the straight wire case (Figure 4.11b), it can be noticed that the magnetic field increases the high velocity towards the wire position at the lower part of the absorber tube. On the contrary, the axial velocity distribution in the case of the periodic wire shows that the high velocity region changes its position along the tube (a pitch at the right and the next pitch at the left). This also explains the oscillating behavior of the axial velocity curves along the axial direction in Figure 4.10 for the periodic current-currying wires cases.

There is an apparent mismatch between the wire position and the high velocity region, that can be explained by the flow inertia. The initial wire accelerates the fluid close to this but, once it reaches a high velocity, the wire position is changed so the high velocity region, close to the initial wire position, is still observed in the following pitch. This process is repetitive along the tube generating a lag between the action of the magnetic force and the flow reaction (high velocity region).
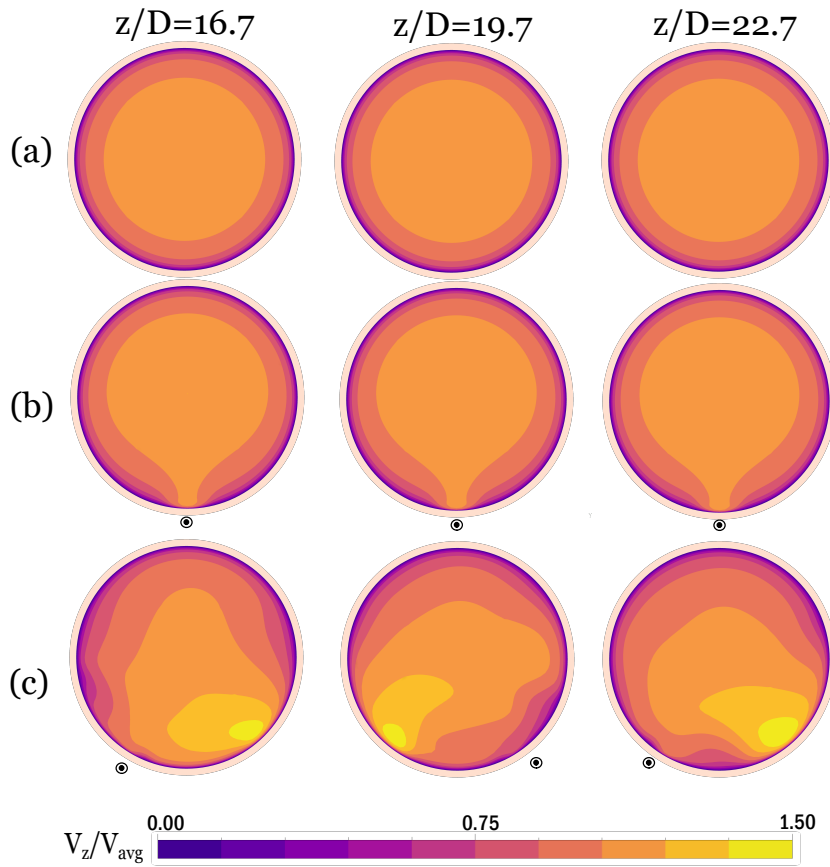
Figure 4.11: Dimensionless axial velocity (V_z/V_{avg}) contours for Re=15000. (a) Mn=0, (b) Straight wire case, Mn=1.84·10^9 (c) periodic wire case, Mn=1.84·10^9 , pitch length $l/D = 3$ and $\theta = 30°$.

For a deep understanding of the non-uniform magnetic field effect on the ferrofluid flow pattern, three dimensional streamlines and streamlines on the cross section of the absorber tube (of the average velocity field) are plotted in Figure 4.12 and Figure 4.13, successively. They have been colored according to the local dimensionless axial velocity of the flow, V_z/V_{avg}.

Figure 4.12a shows the three-dimensional streamlines along the parabolic trough solar collector absorber tube for lowest Reynolds number, Re=15000 in the absence of magnetic field (Mn=0), the streamlines are totally straight, as expected. On the other hand, the case in presences magnetic field generates swirled flows for the straight wire (Figure 4.12b) and periodic wire configuration (Figure 4.12c), forming strand shape streamlines distributed side by side periodically.

The cross-section streamlines (Figure 4.13) shows the generation of a pair of counter-rotating vortices for both cases, straight (a) and periodic wires (b). The vortices size in the fully developed region is uniform along the axial direction for the straight wire case (a). In contrast, for the periodic wire case (b), the vortex size depends on the axial position, eventually the wire pitch position. The increase and decrease in the size of vortices varies periodic way, similar to the high axial velocity zone, along the axial direction of the absorber tube.
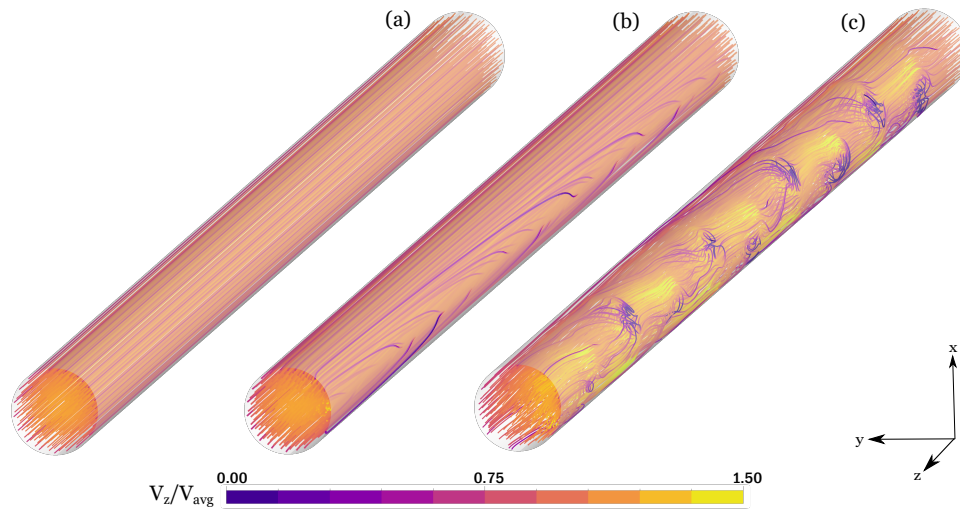
Figure 4.12: Streamlines of ferrofluid flow in PTSC absorber tube for Re=15000 (a) Mn=0, (b) Straight wire case, Mn=$1.84 \cdot 10^9$ (c) periodic wire case, Mn=$1.84 \cdot 10^9$, pitch length $l/D = 3$ and $\theta = 30°$.
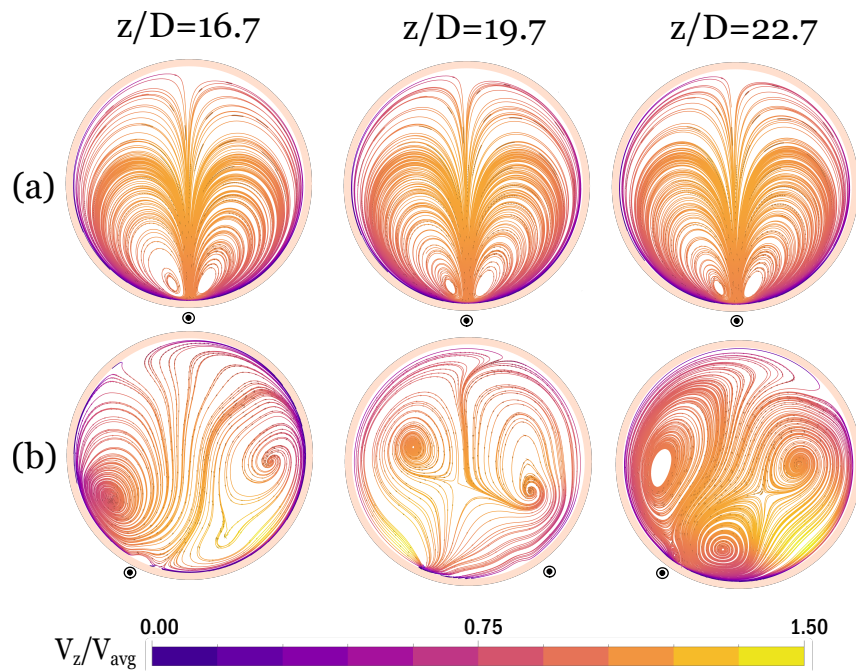
Figure 4.13: Effect of magnetic field on surface streamlines of ferrofluid flow in PTSC absorber tube at different cross-sections, for Re=15000 (a) Mn=0, (b) Straight current-carrying wire case, Mn=$1.84 \cdot 10^9$ (c) periodic wire case, Mn=$1.84 \cdot 10^9$, pitch length $l/D = 3$ and $\theta = 30°$.

In order to analyze the effect of the magnetic field on the convective heat transfer, the average Nusselt number, Nu, is plotted as a function of the Reynolds number, Re and shown in Figure 4.14. The data for Therminol 66 and Fe_3O_4/Therminol 66 as working fluids under non uniform heat flux are included, with and without applied magnetic field, and for different current-carrying wire configurations.

Applying an external magnetic field with Magnetic number equals to Mn=$1.84 \cdot 10^9$, increases the average Nusselt number in the range of Reynolds numbers from Re=15000 to Re=120000. In addition, The periodic configuration increases the Nusselt number comparing to the straight wire case for the same Magnetic number.
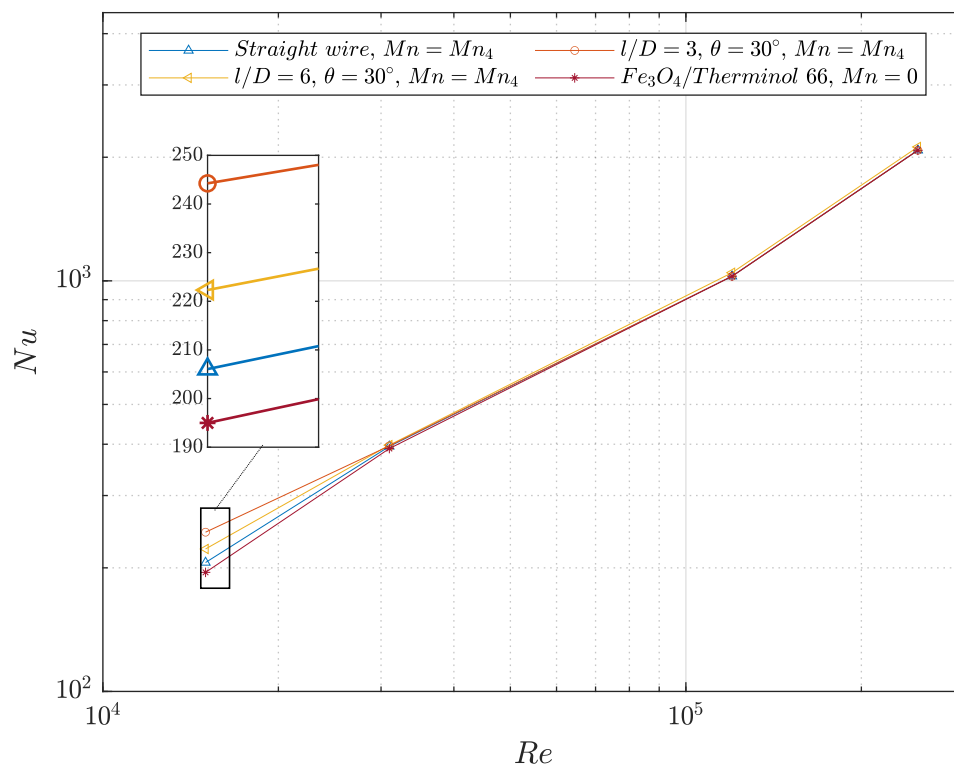
Figure 4.14: Effect of the magnetic field (Mn=$1.84 \cdot 10^9$) generated by straight and periodic wires on the Nusselt number as a function of the Reynolds number.

Darcy's friction factor as a function of the Reynolds number is shown in Figure 4.15. The application of an external magnetic field on the ferrofluid folow, increases the friction factor for both wire configurations (the straight and the periodic), and significant friction factor values are observed for the periodic wire configuration in comparison to the straight wire configuration. Furthermore, the relative pitch length of the wire (l/D) has a noticeable effect on the friction factor value for the studied Magnetic number, Mn=$1.84 \cdot 10^9$, with higher values for the lower pitch, $l = 3 \cdot D$.
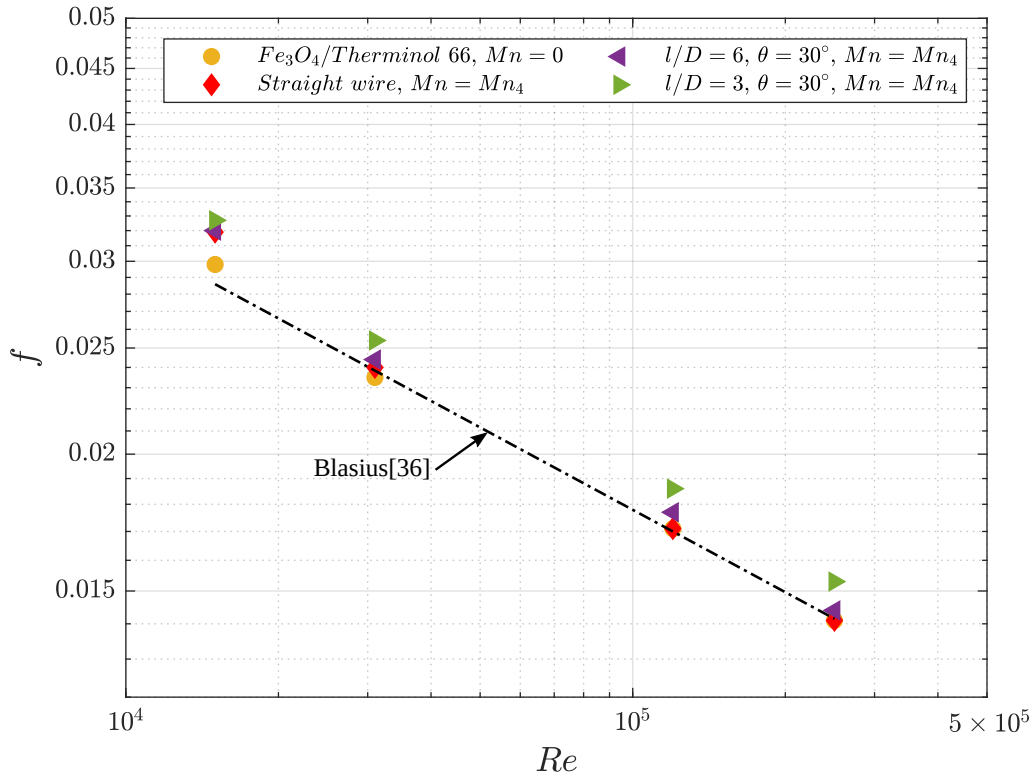
Figure 4.15: Darcy's friction factor as a function of the Reynolds number with and without applied magnetic field for different wire configurations (Mn=1.84·10^9).

4.8.3 Effect of periodic wire pitch position

to evaluate the effect of the current-carrying wire pitch position for the periodic configuration cases, the Nusselt number in function of the Reynolds number is plotted and depicted in Figure 4.16 for different angles: $\theta = 15°$, $\theta = 30°$ and $\theta = 90°$; while the other relevant parameters are kept constant i.e. the Magnetic number (Mn=1.84·10^9), the pitch length (l=3·D) and the distance between the wire and the tube center. As it can be noticed, putting the wire pitches at an intermediate angle, $\theta = 30°$, leads to an increase on the Nusselt number.

The effect of the angle between consecutive wire pitches on the friction factor is shown in Figure 4.17. The results for all the tested wire pitch positions are significantly higher than the straight wire configuration, as expected from the previous Nusselt number results. However, the variation of the friction factor for the different pitches is almost unnoticeable. Therefore, it simplifies the selection of the optimum wire pitch position, the case of $\theta = 30°$ increases the heat transfer but does not imply a very significant increase in the pressure drop .
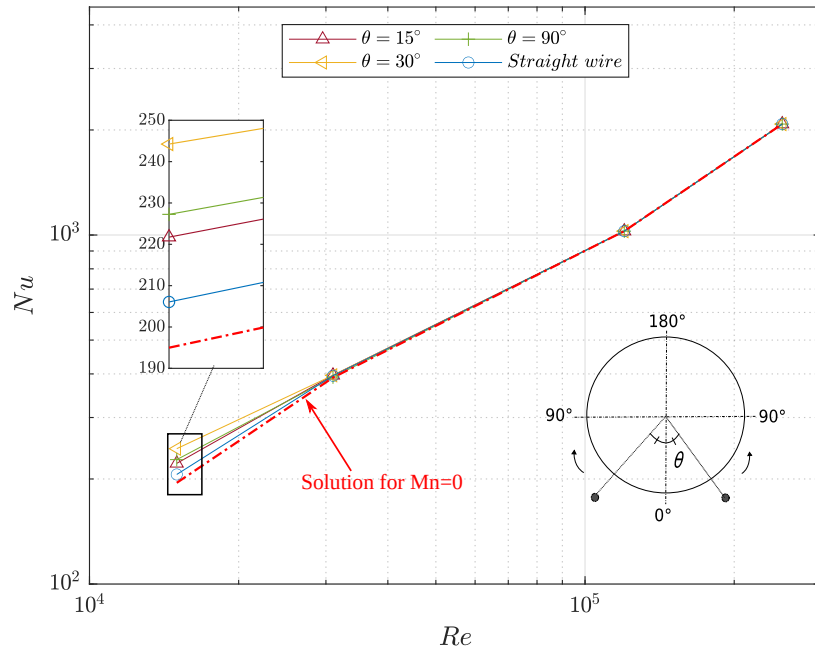
Figure 4.16: Effect of the wire pitch position on Nusselt number. $Mn=1.84 \cdot 10^9$, $l/D = 3$.
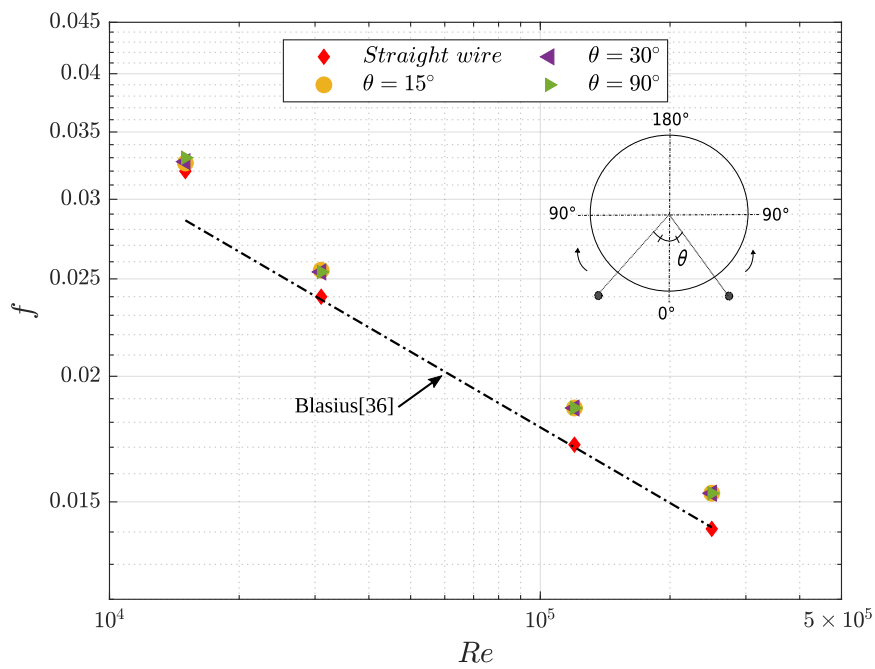
Figure 4.17: The effect of the wire pitch position on Nusselt number on friction factor. $Mn=1.84 \cdot 10^9$, $l/D = 3$.

4.8.4 The thermal efficiency

Since the thermal efficiency is a key parameter for the characterization of the parabolic trough solar collectors, Figure 4.18 shows the thermal efficiency (η_{th}) for three different working conditions as a function of Reynolds number.

The thermal efficiency for the present work is calculated using the following formula:

$$\eta_{th} = \frac{q''}{q'' + q_{loss}} \tag{4.6}$$

Here, the heat losses (q_{loss}) has been calculated according to the model proposed by Mohamad et al. [77].

The results show that the thermal efficiency is significantly higher at higher Reynolds numbers for all cases. However, the use of the ferrofluid improves the thermal efficiency for Reynolds number *Re*=15000 in the presence of the magnetic field in comparison to the base fluid case, with an enhancement of 0.53 % and 1.35 % successively (see right axis Figure 4.18). In contrast, the enhancement margin by the magnetic field tends to be negligible with the increase of the inertial forces of the ferrofluid flow.

On top of that, a comparison between the obtained results using this compound technique (nanoparticles and external magnetic field) with the results from the literature shows the possibility to achieve similar or better enhancement margin using other nanofluids without the necessity for supplementary external power (see Table 4.4).
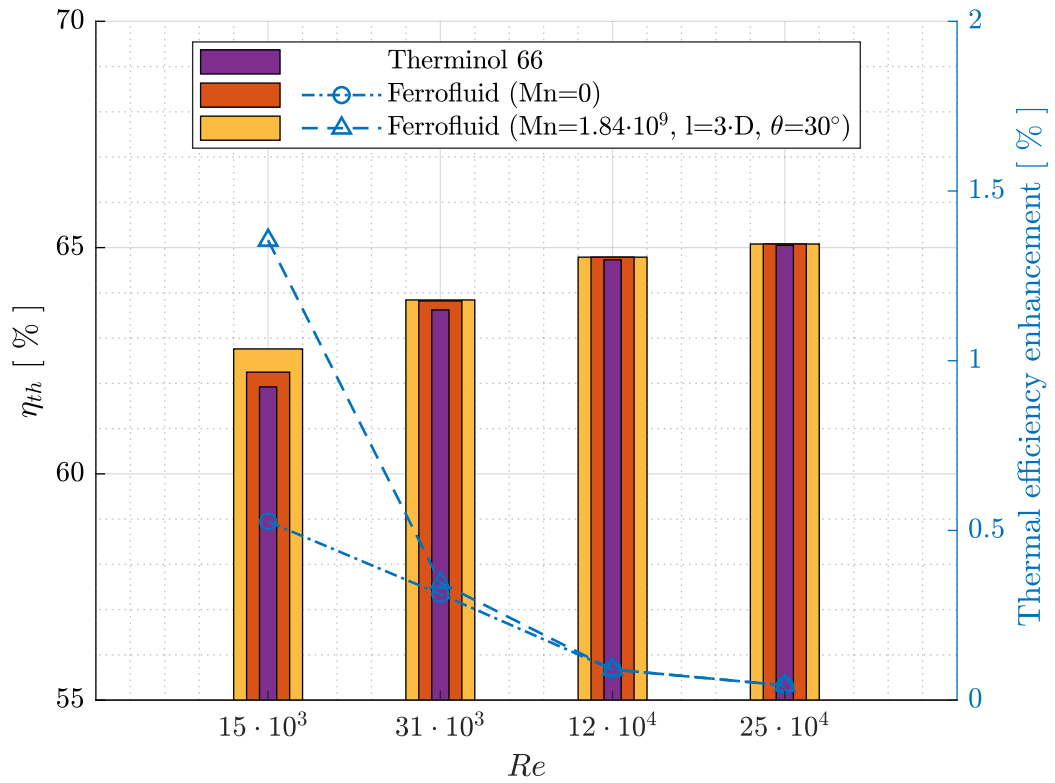
Figure 4.18: The thermal efficiency and thermal efficiency enhancement.

Table 4.4: The thermal efficiency enhancement compared to other studies.

Case	enhancement (%)
Present study (Ferrofluid (Mn=1.84·10^9, l/D=3))	1.35 %
Syltherm 800 with Al_2O_3 and TiO_2 [78]	1.31 %
Therminol VP1 with SWCNT nano particles [79]	4.4 %

4.9   Conclusions

This chapter studied numerically the effect of a non-uniform magnetic field, on the ferrofluid turbulent flow. The study was an application on the parabolic trough solar collector absorber tube. The principle outcomes of this study can be resumed as following

1. This study provides an insight on how the magnetic field influences on the thermal-hydraulic characteristics of the ferrofluid flow.

2. The effect of a magnetic field generated by straight and periodic current-carrying wire configurations on the axial velocity has been visualized in three-dimensional profiles. The Magnetic field created by the straight wire generates a high velocity region near the wire position, while the periodic wire generates an asymmetric velocity profile with a spatially-periodic deformation along the parabolic trough solar collector tube absorber.

3. The spatial periodicity of axial velocity profile for the periodic wire configuration cases is due to the periodic disturbance of the flow produced by the change of direction of the magnetic forces (Kelvin body forces).

4. The augmentation of the Magnetic number leads for an increase in the average Nusselt number as well as the friction factor. The difference on the Nusselt number and friction factor between the straight wire and the periodic wire configuration is also increased at higher Mn.

5. The effect of the Mn decreases at higher Reynolds numbers due to the increase in the inertial forces.

6. The present study showed that an increase in the Nusselt number, but also in the friction factor, could be achieved for the same Magnetic number by changing the wire configuration.

7. The optimum configuration (under the studied conditions) was found for a position angle of $\theta = 30°$ and a pitch length $l = 3 \cdot D$.

8. The use of the magnetic field enhanced the thermal efficiency of the PTSC by up to 1.35 %.

9. The use of ferrofluid and a non-uniform magnetic field generated by electrical current-carrying wire is expensive at the studied Reynolds numbers range comparing to other models using passive methods.

Conclusions and final comments

Conclusions

The present doctoral work has shed light on the heat transfer intensification using a compound method which combines the addition of magnetic nanoparticles to a heat transfer fluid (HTF) and a non-uniform magnetic field generated through the flow of an electrical current in a current-carrying wire.

This numerical analysis has characterized the thermal-hydraulic characteristics of the ferrofluids flow under the effect of a novel wire configuration which is based on the idea of the periodic change of the wire position. Furthermore this analysis has touched upon the laminar flow regime, as well as the turbulent. In addition, this numerical study has been performed using the commercial CFD code, ANSYS Fluent.

Due to the importance of the renewable energies, this study has focused with keen interest, on the reliability of using this novel technique on the parabolic trough solar collector absorber tube.

However, the main outcomes from this study are the flowing:

1. The consideration of the ferrofluids as dielectric fluid (the current density $J = 0$) helped reduce the mathematical interpretation of the physical phenomena that occurs during the interaction of a magnetic field with the ferrofluids flow, on the only term i.e. Kelvin body force, neglecting the magnetohydrodynamic term (Lorentz force) from the momentum equation.

2. The user defined functions (UDFs) allowed to implement the Kelvin body force into Fluent solver, representing a good solution as a tool for the numerical simulations of multiphysics problems.

3. The presence of a non-uniform magnetic field has shown noticeable effect on the velocity distribution.

4. The periodic distribution of the magnetic force has generated a spatial periodicity of the velocity profile for both flow regimes.

5. The magnetic field intensifies the convective heat transfer which is noticed from the increase of the average Nusselt number for both flow regimes. However, this enhancement is accompanied by the increase of the friction factor.

6. The augmentation in the magnetic field intensity yields an increase in the Nusselt number but also the friction factor until a saturation point.

7. It has been observed that the magnetic forces effect on the ferrofluid flow decreases with the increase of inertial forces, whether for the laminar regime or the turbulent.

8. The periodic configuration proved its efficiency against the straight configuration of the current-carrying wire.

9. The use of ferrofluids and a magnetic field generated by electricity in PTSC absorber as an enhancement technique is expensive in comparison with passive techniques.

10. The use of the magnetic field as a heat transfer enhancement technique is promising at lower Reynolds numbers (Laminar regime).

Future works

The current doctoral thesis represents a preliminary study for our research team in the ferro-hydrodynamics discipline. However, many works are needed to understand more deeply the effect of magnetic forces on the thermal-hydraulic characteristics of the ferrofluids toward a reliable use.

From that standpoint, the following points touch upon our future works:

1. The assessment of the feasibility of using the magnetic field as heat transfer enhancement technique using the R3 criterion.

2. Study of some fundamental aspects related to the alternating magnetic field applications.

3. Study of the possibility of using other magnetic field generation sources, like the permanent magnets.

4. Investigate the use of ferrofluids as heat transfer fluid in evacuated tube solar collectors under the effect of an external magnetic field.

[1] Y. Çengel **and** A. J. Ghajar, *Transferencia de calor y masa*. McGraw-Hill Interamericana de España S.L., 2011.

[2] M. Sheikholeslami, M. Gorji-Bandpy **and** D. D. Ganji, "Review of heat transfer enhancement methods: Focus on passive methods using swirl flow devices", *Renewable and Sustainable Energy Reviews*, **jourvol** 49, **pages** 444–469, 2015.

[3] R. L. Webb **and** N.-H. Kim, *Principles of Enhanced Heat Transfer*. Taylor & Francis, 2005.

[4] T. Bergman, A. Lavine, F. Incropera **and** D. DeWitt, *Fundamentals of Heat and Mass Transfer*. Wiley, 2017.

[5] J. P. Solano Fernández, "Análisis del flujo y de la transmisión de calor en intercambiadores de superficie rascada por movimiento lineal alternativo", Ph.D. dissertation, Universidad Politécnica de Cartagena., Campus Muralla del Mar, Calle Doctor Fleming, s/n, 30202 Cartagena, Murcia, España, 2009.

[6] A. Changdar **and** S. S. Chakraborty, "Laser processing of metal foam - a review", *Journal of Manufacturing Processes*, **jourvol** 61, **pages** 208–225, 2021.

[7] S. T. W. Kuruneru, K. Vafai, E. Sauret **and** Y. Gu, "Application of porous metal foam heat exchangers and the implications of particulate fouling for energy-intensive industries", *Chemical Engineering Science*, **jourvol** 228, **page** 115 968, 2020.

[8] Z. S. Kareem, M. Mohd Jaafar, T. M. Lazim, S. Abdullah **and** A. F. AbdulWahid, "Heat transfer enhancement in two-start spirally corrugated tube", *Alexandria Engineering Journal*, **jourvol** 54, **number** 3, **pages** 415–422, 2015.

[9] Y. Kim, J. S. Kim, D. H. Shin, S. M. You **and** J. Lee, "Enhanced thermal performance of a thermosyphon for waste heat recovery: Microporous coating at evaporator and hydrophobic coating at condenser", *Applied Thermal Engineering*, **jourvol** 175, **page** 115 332, 2020.

[10] J. Wang, Z. Zhai, D. Zheng, L. Yang **and** B. Sundén, "Investigation of heat transfer characteristics of al2o3-water nanofluids in an electric heater", *Heat Transfer Engineering*, **jourvol** 42, **number** 19-20, **pages** 1765–1774, 2021.

[11] N. Sreenivasalu Reddy, S. Gowreesh Subramanya, K. Vishwanath, M. Karthikeyan **and** S. Kanchiraya, "Enhancing the thermal efficiency of parabolic trough collector using rotary receiver tube", *Sustainable Energy Technologies and Assessments*, **jourvol** 51, **page** 101 941, 2022.

[12]   R. N. Sharma, "Fluid dynamics-based analytical model for synthetic jet actuation", *AIAA Journal*, **jourvol** 45, **number** 8, **pages** 1841–1847, 2007.

[13]   T. Alam **and** M.-H. Kim, "A comprehensive review on single phase heat transfer enhancement techniques in heat exchanger applications", *Renewable and Sustainable Energy Reviews*, **jourvol** 81, **pages** 813–839, 2018.

[14]   J. Muñoz Cámara, "Análisis experimental de los mecanismos de mejora termohidráulica en reactores de flujo oscilatorio", Ph.D. dissertation, Universidad Politécnica de Cartagena., Campus Muralla del Mar, Calle Doctor Fleming, s/n, 30202 Cartagena, Murcia, España, 2020.

[15]   S. Wangnipparnto, J. Tiansuwan, S. Jiracheewanun, T. Kiatsiriroat **and** C.-C. Wang, "Air side performance of thermosyphon heat exchanger in low reynolds number region: With and without electric field", *Energy Conversion and Management*, **jourvol** 43, **number** 14, **pages** 1791–1800, 2002.

[16]   M. Bahiraei, N. Mazaheri **and** S. Hosseini, "Neural network modeling of thermo-hydraulic attributes and entropy generation of an ecofriendly nanofluid flow inside tubes equipped with novel rotary coaxial double-twisted tape", *Powder Technology*, **jourvol** 369, **pages** 162–175, 2020.

[17]   R. Rosensweig, *Ferrohydrodynamics*, **jourser** Dover Books on Physics. Dover Publications, 2013.

[18]   S. Nasser El Dine, "Multi-physics modeling of cooling of power transformers immersed in a ferrofluid", Ph.D. dissertation, Université Paris-Saclay, CentraleSupelec, CNRS, Laboratoire de Génie Electrique et Electronique de Paris, 91192, Gif-sur-Yvette, France, 2021.

[19]   S. Odenbach, "Magnetic fluids - suspensions of magnetic dipoles and their magnetic control", *Journal of Physics: Condensed Matter*, **jourvol** 15, **number** 15, S1497–S1508, 2003.

[20]   Z. Sun, Q. Yue, Y. Liu *et al.*, "Rational synthesis of superparamagnetic core–shell structured mesoporous microspheres with large pore sizes", *J. Mater. Chem. A*, **jourvol** 2, **pages** 18 322–18 328, 43 2014.

[21]   J. L. Neuringer **and** R. E. Rosensweig, "Ferrohydrodynamics", *The Physics of Fluids*, **jourvol** 7, **number** 12, **pages** 1927–1937, 1964.

[22]   Z. Wu, A. Iqbal **and** F. B. Amara, *Modeling and control of magnetic fluid deformable mirrors for adaptive optics systems*. Springer Science & Business Media, 2012.

[23]   "Recent advances in synthesis and surface modification of superparamagnetic iron oxide nanoparticles with silica", *Journal of Magnetism and Magnetic Materials*, **jourvol** 416, **pages** 275–291, 2016.

[24]   U. Jeong, X. Teng, Y. Wang, H. Yang **and** Y. Xia, "Superparamagnetic colloids: Controlled synthesis and niche applications", *Advanced Materials*, **jourvol** 19, **number** 1, **pages** 33–60, 2007.

[25] D. Griffiths, *Introduction to Electrodynamics*. Pearson Education, 2014.

[26] T. K. Oanh Vuong, T. T. Le, H. D. Do *et al.*, "Pmao-assisted thermal decomposition synthesis of high-stability ferrofluid based on magnetite nanoparticles for hyperthermia and mri applications", *Materials Chemistry and Physics*, **jourvol** 245, **page** 122 762, 2020.

[27] N. Lee, D. Yoo, D. Ling, M. H. Cho, T. Hyeon **and** J. Cheon, "Iron oxide based nanoparticles for multimodal imaging and magnetoresponsive therapy", *Chemical reviews*, **jourvol** 115, **number** 19, **pages** 10 637–10 689, 2015.

[28] S. Odenbach **and** S. Thurm, "Magnetoviscous effects in ferrofluids", **in** *Ferrofluids: Magnetically Controllable Fluids and Their Applications* S. Odenbach, Ed. Berlin, Heidelberg: Springer Berlin Heidelberg, 2002, **pages** 185–201.

[29] *What are magnetic fluid speakers and how are they better than a traditional speaker?*, https://www.sony.com/en/SonyInfo/csr/SonyEnvironment/products/BDV-N9200WL.html, Accessed: 2022-03-10.

[30] J.-P. Déry, D. Brousseau, M. Rochette, E. F. Borra **and** A. M. Ritcey, "Aluminum-coated elastomer thin films for the fabrication of a ferrofluidic deformable mirror", *Journal of Applied Polymer Science*, **jourvol** 134, **number** 9, 2017.

[31] E. Borra, "Magnetic liquid deformable mirrors for astronomical applications: Active correction of optical aberrations from lower-grade optics and support system", *The Astrophysical Journal Supplement Series*, **jourvol** 201, **number** 2, **page** 8, 2012.

[32] H. Yamaguchi, *Engineering Fluid Mechanics*, **jourser** Fluid Mechanics and Its Applications. SPRINGER, 2008, **volume** 85.

[33] M. Alsaady, R. Fu, B. Li, R. Boukhanouf **and** Y. Yan, "Thermo-physical properties and thermo-magnetic convection of ferrofluid", *Applied Thermal Engineering*, **jourvol** 88, **pages** 14–21, 2015.

[34] W.-G. Fruh, "Heat transfer enhancement by thermomagnetic convection", **in** *Sustainable (Bio) Chemical Process Technology-Incorporating the 6th Intenational Conference on Process Intensification* 2005, **pages** 47–56.

[35] P. S. Szabo, M. Beković **and** W.-G. Früh, "Using infrared thermography to investigate thermomagnetic convection under spatial non-uniform magnetic field", *International Journal of Thermal Sciences*, **jourvol** 116, **pages** 118–128, 2017.

[36] M. Pattanaik, S. Cheekati, V. Varma **and** R. Ramanujan, "A novel magnetic cooling device for long distance heat transfer", *Applied Thermal Engineering*, **jourvol** 201, **page** 117 777, 2022.

[37] V. Kumar, M. Casel, V. Dau **and** P. Woodfield, "Effect of axisymmetric magnetic field strength on heat transfer from a current-carrying micro-wire in ferrofluid", *International Journal of Thermal Sciences*, **jourvol** 167, **page** 106 976, 2021.

[38] R. Zanella, C. Nore, X. Mininger, F. Bouillault **and** J.-L. Guermond, "Numerical study of cooling by ferrofluids in an electrical transformer using an axisymmetric model", *IEEE Transactions on Magnetics*, **jourvol** 57, **number** 7, **pages** 1–4, 2021.

[39] M. H. Buschmann, "Critical review of heat transfer experiments in ferrohydrodynamic pipe flow utilising ferronanofluids", *International Journal of Thermal Sciences*, **jourvol** 157, **page** 106 426, 2020.

[40] A. Shakiba **and** K. Vahedi, "Numerical analysis of magnetic field effects on hydrothermal behavior of a magnetic nanofluid in a double pipe heat exchanger", *Journal of Magnetism and Magnetic Materials*, **jourvol** 402, **pages** 131–142, 2016.

[41] M. M. Larimi, A. Ghanaat, A. Ramiar **and** A. A. Ranjbar, "Forced convection heat transfer in a channel under the influence of various non-uniform transverse magnetic field arrangements", *International Journal of Mechanical Sciences*, **jourvol** 118, **pages** 101–112, 2016.

[42] H. Soltanipour, A. Gharegöz **and** M. B. Oskooee, "Numerical study of magnetic field effect on the ferrofluid forced convection and entropy generation in a curved pipe", *Journal of the Brazilian Society of Mechanical Sciences and Engineering*, **jourvol** 42, **number** 3, **pages** 1–15, 2020.

[43] E. Yousefi, H. R. Nazif, H. Najafi Khaboshan **and** A. Azarinia, "Non-Uniform Magnetic Field Effect on Forced Convection Heat Transfer of Flattened Tubes Using Two-Phase Mixture Model", *Heat Transfer Engineering*, **jourvol** 42, **number** 12, **pages** 1041–1058, 2021.

[44] A. Khosravi, M. Malekan **and** M. E. H. Assad, "Numerical analysis of magnetic field effects on the heat transfer enhancement in ferrofluids for a parabolic trough solar collector", *Renewable Energy*, **jourvol** 134, **pages** 54–63, 2019, ISSN: 0960-1481.

[45] M. Malekan, A. Khosravi **and** S. Syri, "Heat transfer modeling of a parabolic trough solar collector with working fluid of fe3o4 and cuo/therminol 66 nanofluids under magnetic field", *Applied Thermal Engineering*, **jourvol** 163, 2019.

[46] M. Alsaady, R. Fu, Y. Yan, Z. Liu, S. Wu **and** R. Boukhanouf, "An experimental investigation on the effect of ferrofluids on the efficiency of novel parabolic trough solar collector under laminar flow conditions", *Heat Transfer Engineering*, **jourvol** 40, **number** 9-10, **pages** 753–761, 2019.

[47] H. Soltanipour, A. Gharegöz **and** M. B. Oskooee, "Numerical study of magnetic field effect on the ferrofluid forced convection and entropy generation in a curved pipe", *Journal of the Brazilian Society of Mechanical Sciences and Engineering*, **jourvol** 42, **number** 3, **pages** 1–15, 2020.

[48] E. E. Tzirtzilakis, "A mathematical model for blood flow in magnetic field", *Physics of Fluids*, **jourvol** 17, **number** 7, **page** 077 103, 2005.

[49] R. Zanella, "Thermomagnetic convection in ferrofluids : Finite element approximation and application to transformer cooling", Ph.D. dissertation, Université Paris-Saclay, CentraleSupelec, CNRS, Laboratoire de Génie Electrique et Electronique de Paris, 91192, Gif-sur-Yvette, France, 2018.

[50] S. A. Wahajuddin, "Superparamagnetic iron oxide nanoparticles: Magnetic nanoplat-forms as drug carriers", *International journal of nanomedicine*, **jourvol** 7, **page** 3445, 2012.

[51] M. Goharkhah **and** M. Ashjaee, "Effect of an alternating nonuniform magnetic field on ferrofluid flow and heat transfer in a channel", *Journal of Magnetism and Magnetic Materials*, **jourvol** 362, **pages** 80–89, 2014.

[52] B. C. Pak **and** Y. I. Cho, "Hydrodynamic and heat transfer study of dispersed fluids with submicron metallic oxide particles", *Experimental Heat Transfer an International Journal*, **jourvol** 11, **number** 2, **pages** 151–170, 1998.

[53] R. L. Hamilton **and** O. Crosser, "Thermal conductivity of heterogeneous two-component systems", *Industrial & Engineering chemistry fundamentals*, **jourvol** 1, **number** 3, **pages** 187–191, 1962.

[54] C. Liu, M. Pan, L. Zheng **and** P. Lin, "Effects of heterogeneous catalysis in porous media on nanofluid-based reactions", *International Communications in Heat and Mass Transfer*, **jourvol** 110, **page** 104 434, 2020.

[55] ANSYS® FLUENT, *Release 17.1, User's Guide, ANSYS, Inc*, **version** 17.1.

[56] H. Oh, *Applied Computational Fluid Dynamics*. IntechOpen, 2012, ISBN: 9789535102717. [Online]. Available: https://books.google.dz/books?id=oOuZDwAAQBAJ.

[57] A. Benabderrahmane, "Etude numérique de l'application des nanofluides dans l'amélioration du transfert thermique dans les capteurs solaires", Ph.D. dissertation, Université Djilali Lyabes, Sidi Bel abbes, 22000, Algeria, 2017.

[58] P. SCIENZA, "Numerical investigation of non-newtonian biomagnetic fluid flows in presence of localised magnetic field", M.S. thesis, School of Aerospace, Transport **and** Manufacturing, Cranfield University, 2015.

[59] R. A. Mahdi, H. Mohammed, K. Munisamy **and** N. Saeid, "Experimental and numerical investigation of combined convection heat transfer and fluid flow around circular cylinder through rectangular and trapezoidal open-cell aluminum foams", *Chemical Engineering Communications*, **jourvol** 202, **number** 5, **pages** 674–693, 2015.

[60] B. E. Rapp, *Microfluidics: modeling, mechanics and mathematics*. William Andrew, 2016.

[61] Y. Çengel **and** A. Ghajar, *Heat and Mass Transfer: Fundamentals & Applications*. McGraw Hill Education, 2015.

[62] H. Aghamiri, M. Niknejadi **and** D. Toghraie, "Analysis of the forced convection of two - phase Ferro - nanofluid flow in a completely porous microchannel containing rotating cylinders", *Scientific Reports*, **jourvol** 11, **pages** 1–18, 2021.

[63] M. Malekan **and** A. Khosravi, "Investigation of convective heat transfer of ferrofluid using CFD simulation and adaptive neuro-fuzzy inference system optimized with particle swarm optimization algorithm", *Powder Technology*, **jourvol** 333, **pages** 364–376, 2018.

[64] S. W. Churchill **and** H. Ozoe, "Correlations for Laminar Forced Convection with Uniform Heating in Flow over a Plate and in Developing and Fully Developed Flow in a Tube", *Journal of Heat Transfer*, **jourvol** 95, **number** 1, **pages** 78–84, 1973.

[65] J. Fredriksson, M. Eickhoff, L. Giese **and** M. Herzog, "A comparison and evaluation of innovative parabolic trough collector concepts for large-scale application", *Solar Energy*, **jourvol** 215, **pages** 266–310, 2021.

[66] P. Forman, S. Penkert, C. Kämper, T. Stallmann, P. Mark **and** J. Schnell, "A survey of solar concrete shell collectors for parabolic troughs", *Renewable and Sustainable Energy Reviews*, **jourvol** 134, **page** 110 331, 2020.

[67] A. Raheem, W. Siddique, Z. H. Farooqui *et al.*, "Performance evaluation of adding helical-screw tape inserts in parabolic solar trough collectors as a source of cleaner energy production", *Journal of Cleaner Production*, **jourvol** 297, **page** 126 628, 2021.

[68] G. Manikandan, S. Iniyan **and** R. Goic, "Enhancing the optical and thermal efficiency of a parabolic trough collector – a review", *Applied Energy*, **jourvol** 235, **pages** 1524–1540, 2019.

[69] M. C. Kulahli, S. Akbulut Özen **and** A. B. Etemoglu, "Numerical simulation of a parabolic trough collector containing a novel parabolic reflector with varying focal length", *Applied Thermal Engineering*, **jourvol** 161, **page** 114 210, 2019.

[70] *Skytrough parabolic solar collector*. [Online]. Available: https://www.energy.gov/eere/solar/articles/skytrough-parabolic-solar-collector.

[71] S. Ebrahim Ghasemi **and** A. Akbar Ranjbar, "Numerical thermal study on effect of porous rings on performance of solar parabolic trough collector", *Applied Thermal Engineering*, **jourvol** 118, **pages** 807–816, 2017.

[72] H. Blasius, "Das aehnlichkeitsgesetz bei reibungsvorgängen in flüssigkeiten", **in** *Mitteilungen über Forschungsarbeiten auf dem Gebiete des Ingenieurwesens: insbesondere aus den Laboratorien der technischen Hochschulen* Berlin, Heidelberg: Springer Berlin Heidelberg, 1913, **pages** 1–41.

[73] B. Petukhov, "Heat transfer and friction in turbulent pipe flow with variable physical properties", **injourser** Advances in Heat Transfer J. P. Hartnett **and** T. F. Irvine, Eds., **volume** 6, Elsevier, 1970, **pages** 503–564.

[74] V. Gnielinski, "New equations for heat and mass transfer in turbulent pipe and channel flow", *International Chemical Engineering*, **jourvol** 16, **number** 2, **pages** 359–368, 1976.

[75] H. Aminfar, M. Mohammadpourfard **and** S. Zonouzi, "Numerical study of the ferrofluid flow and heat transfer through a rectangular duct in the presence of a non-uniform transverse magnetic field", *Journal of Magnetism and Magnetic Materials*, **jourvol** 31, **number** 6, **pages** 31–42, 2013.

[76] A. Shakiba **and** V. Khodadad, "Numerical analysis of magnetic field effects on hydro-thermal behavior of a magnetic nanofluid in a double pipe heat exchanger", *Journal of Magnetism and Magnetic Materials*, **jourvol** 402, **pages** 131–142, 2016.

[77] A. Mohamad, J. Orfi **and** H. Alansary, "Heat losses from parabolic trough solar collectors", *International Journal of Energy Research*, **jourvol** 38, **pages** 20–28, 2013.

[78] E. Bellos **and** C. Tzivanidis, "Thermal analysis of parabolic trough collector operating with mono and hybrid nanofluids", *Sustainable Energy Technologies and Assessments*, **jourvol** 26, **pages** 105–115, 2018.

[79] A. Mwesigye, İ. H. Yılmaz **and** J. P. Meyer, "Numerical analysis of the thermal and thermo-dynamic performance of a parabolic trough solar collector using swcnts-therminol®vp-1 nanofluid", *Renewable Energy*, **jourvol** 119, **pages** 844–862, 2018.